NEOGENE TO QUATERNARY FAULT ACTIVITY AND SALT TECTONICS

WITHIN THE TERREBONNE SALT WITHDRAWAL BASIN: EFFECT OF

SEDIMENT LOADING ON SUBSIDENCE AND SALT-FAULT INTERACTION
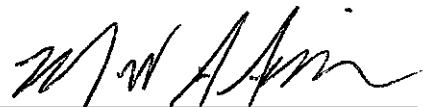

AN ABSTRACT SUBMITTED ON THE FIVTH DAY OF MAY 2021 TO THE

DEPARTMENT OF EARTH AND ENVIRONMENTAL SCIENCES IN PARTIAL

FULFILLMENT OF THE REQUIREMENTS OF THE SCHOOL OF SCIENCE AND

ENGINEERING OF TULANE UNIVERSITY FOR THE DEGREE OF
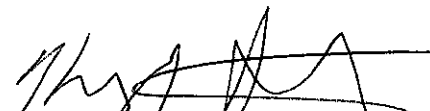
DOCTOR OF PHILOSOPHY

BY

_____
AKINBOBOLA O. AKINTOMIDE

APPROVED:

_____
Mead A. Allison, Ph.D.

_____
Kyle M. Straub, Ph.D.

_____
Elizabeth McDade, Ph.D.
External Member

ABSTRACT

Salt basins are complex structural systems, showing genetic relationships between salt structures, faults, and variable sediment depositional patterns. The dynamics of salt-fault interaction, the role of shale deformation, and the influence of salt evacuation on surface features have been poorly understood. A link between all these processes is the throw history of faults adjacent to and within a salt basin. In this dissertation, I interpret industry well logs and 3D seismic data from the Terrebonne Salt Withdrawal Basin (TSWB) of southeastern Louisiana, to understand these processes. The methodology includes the use of fault throw maps, throw variations along strike and with depth, and sediment expansion indices to understand fault kinematics adjacent to sediment loads and mobile material, i.e., salt or shale.

I address the histories of three faults along the northern margin of the TSWB: the Lake Boudreaux, Montegut, and Isle de Jean Charles faults. Each shows Miocene and Quaternary active phases correlated with sediment loading, separated by relative inactivity during the Pliocene. The pattern of Quaternary activity and the surface projections of these faults are consistent with a fault-controlled pattern of wetland loss, suggesting that faults in southeastern Louisiana are active.

Isle de Jean Charles fault and the Lake Boudreaux fault interact with the Bully Camp and Lake Barre Salt stocks, respectively. Each stock is interpreted to have grown by a different diapiric mechanism, consistent with different spatial patterns of throw variation on the two faults, despite similar temporal histories. Throw on the Isle de Jean Charles fault increases towards the Bully Camp stock, suggesting deformation inside and outside the stock. In contrast, a decrease in the throw on the Lake Boudreaux fault and an

increase in diameter of the Lake Barre stock indicate that deformation exists only within the stock. Additionally, this dissertation considers throw patterns along the southern margin of the TSWB, showing that faults linking the Dog Lake and Caillou Island salt stocks are affected by shale deformation adjacent to salt. These results show that studies of fault-related subsidence and wetland loss in coastal Louisiana need to include observations from nearby salt structures.

NEOGENE TO QUATERNARY FAULT ACTIVITY AND SALT TECTONICS

WITHIN THE TERREBONNE SALT WITHDRAWAL BASIN: EFFECT OF
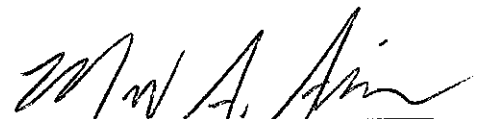
SEDIMENT LOADING ON SUBSIDENCE AND SALT-FAULT INTERACTION

A DISSERTATION SUBMITTED ON THE FIVTH DAY OF MAY 2021 TO THE

DEPARTMENT OF EARTH AND ENVIRONMENTAL SCIENCES IN PARTIAL

FULFILLMENT OF THE REQUIREMENTS OF THE SCHOOL OF SCIENCE AND

ENGINEERING OF TULANE UNIVERSITY FOR THE DEGREE OF
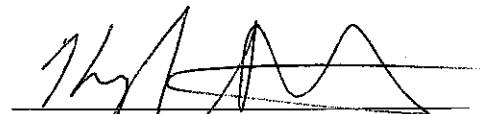
DOCTOR OF PHILOSOPHY

BY

_____

AKINBOBOLA O. AKINTOMIDE

APPROVED:

_____
Mead A. Allison, Ph.D.

_____
Kyle M. Straub, Ph.D.

_____
Elizabeth McDade, Ph.D.
External Member

ACKNOWLEDGEMENTS

Environmental Science at Tulane University. I appreciate my mentor, Edith Wilson, and my friends for cheering me on.

I dedicate this dissertation to my parents, Rufus and Dolapo Akintomide, my siblings Toyosi, Yemi and Lola, and my in-laws Bro. Leke, Oyinda, and Wale for their support and encouraging words. Also, Bishop Taiwo Adelakun, Captain Femi Olaiya, and Lola for their financial contribution towards my graduate program.

TABLE OF CONTENTS

LIST OF TABLES

LIST OF FIGURES

x

Chapter 1

Introduction

1.1 Motivation

Salt tectonics is intriguing because it introduces new dynamics and complexity into sedimentary basins. The complicated structure formed by salt deformation serves as a migration path and traps for hydrocarbon. The prolific hydrocarbon reserves found in salt basins drove exploration activities and research on salt tectonics. Over the last 90 years, we have seen an increase in research on salt expulsion, growth of salt structure, and mechanism involves in salt deformation. Some of the mechanisms proposed over the years are down-building (Barton, 1933), thermal convention (Talbot, 1978), differential loading (Bailey, 1931; Harrison, 1927; Rettger, 1935), regional extension (Vendeville and Jackson, 1990; Vendeville and Jackson, 1992b), etc. Among these mechanisms, the differential loading, extension, and weight of sediment loading explain a lot of salt-related features. One of such features is salt-related faults that interact with salt structures.

Fault formation and propagation are complex, and when a fault forms in a salt basin, its geometry and kinematic becomes complicated. The complication in fault growth led to research on salt-fault interaction as it relates to the way a fault interacts with a salt structure (Rowan et al., 1999; Tvedt et al., 2016; Tvedt et al., 2013), formation and displacement pattern of radial faults around a salt stock (Carruthers et al., 2013; Coleman et al., 2018; Mattos and Alves, 2018) and diapiric stages of a stock (Koyi, 1998;

1

Perez-Garcia et al., 2013; Vendeville and Jackson, 1992a, b). Understanding these salt-fault mechanisms is vital because it controls sediment loading (Alexander and Flemings, 1995; Seni, 1992), salt evacuation (Seni, 1992; Vendeville and Jackson, 1992b), hydrocarbon accumulation (Woodbury et al., 1974), and its impact on surface processes (Gagliano et al., 2003b). However, despite the extensive studies and research on fault activity in salt basins, there are gaps in the knowledge of salt tectonics, and this dissertation addresses some of these gaps.

The first knowledge gap is the role of subsurface salt deformation on surface processes. In the second chapter, I examine how subsurface salt evacuation on a long time scale influences coastal wetland loss and coastal subsidence. The second gap is the dynamic of spatial and temporal throw variation of faults in salt basins. Although previous studies have addressed throw variation due to the interaction of multiple faults (Childs et al., 1995, 1996; Walsh et al., 2003; Walsh and Watterson, 1991), it remains unclear how the mechanisms of fault formation and its interaction with adjacent salt stock can lead to throw variability. In Chapter 3, I addressed the effect of diapiric stress on fault propagation and displacement pattern. The third knowledge gap is about the mechanism of initiation and propagation of faults that connects adjacent salt stocks, a process that is not clear despite the presence and abundance of these faults in salt basins. In chapter 4 of this study, I proposed three conceptual models for the growth of fault that connect adjacent salt structures. I tested the validity of my models by studying the throw pattern of faults and how the lithology of strata can influence throw gradient at the salt-fault contact.

1.2 Approach

The study of fault growth can help to interpret the timing of salt evacuation and sediment loading in a salt basin. Fault growth is sub-divided into three stages; initiation, propagation, and cessation stage (Thorsen, 1963). A fault initiates due to brittle deformation, tensional stresses, and regional extension. In rocks, a fault occurs as a displacement of strata. Rarely does one find a single fault. More typically, a fault occurs as an array of isolated fault segments (Childs et al., 1995; Walsh et al., 2003; Walsh and Watterson, 1991). With continuous displacement, each segment propagates laterally and temporally (Fig. 1.1). Lateral propagation leads to overlapping segments resulting in segment interaction and an increase in the throw (Peacock and Sanderson, 1991; Willemse et al., 1996; Young et al., 2001). The pattern of interaction can vary from soft linkage, i.e., strictly kinematic interaction without being physically linked (Peacock and Sanderson, 1991; Walsh and Watterson, 1991) to hard linkage, i.e., physical intersection (Walsh and Watterson, 1991).

Temporally, fault tips can propagate upward and downward (Fig. 1.2). In the dip direction, two segments can grow towards each other, interact, and link to form a single fault (Mansfield and Cartwright, 1996). A throw minimum characterizes the point of linkage (Fig. 1.2d). The fault can also continue to propagate upward until it intercepts the surface of deposition leading to differential loading on the hanging wall relative to the footwall. In this situation, the fault is syn-depositional; i.e., it is actively slipping during sediment loading. Fault throw and gradient during the syn-depositional phase are relatively higher compare to when slip occur after the sediment has been deposited. The

fault gradient is used to differentiate the syn-depositional phase from the post-

depositional phase.
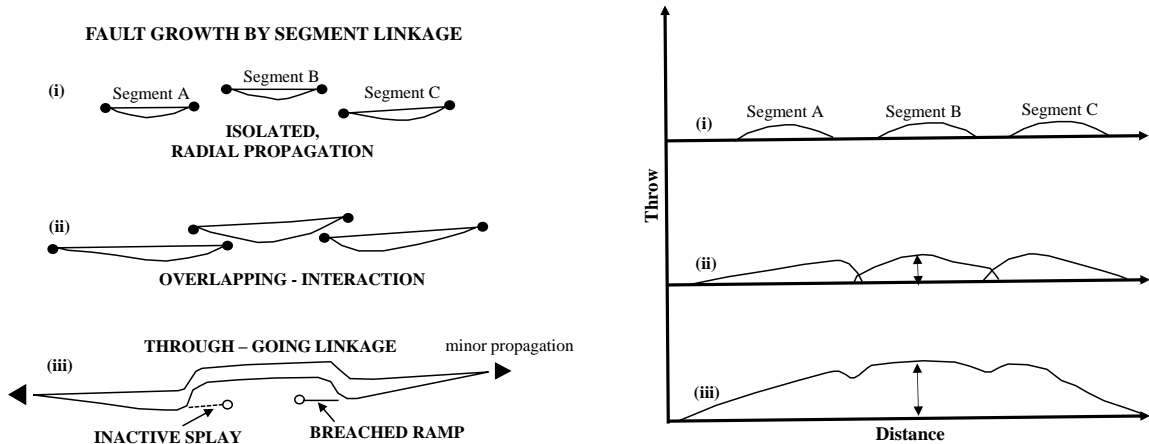
Figure 1.1. A schematic diagram showing the growth of segmented faults in an array in both map view (left) and cross-sectional view (right). At stage 1, i) the three segments are isolated and have a displacement pattern that resembles that of an isolated fault. By the second stage, (ii) they have propagated towards each other. At this stage, they are soft-linked, i.e., they interact with each other kinematically, increasing the displacement at the interacting tips. By stage 3, (iii) the segments are physically linked, forming a single fault. The displacement pattern of the fault is similar to that of a single isolated fault except for the displacement minimal at the linkage point. Modified after Cartwright et al. (1995).

Rock strata also record fault activity through thickening across a fault. The

amount of thickening can indicate the extent of movement (Thorsen, 1963). If the fault is

growing in a salt basin, the amount of differential loading can be very high due to

simultaneous salt expulsion (e.g., Alexander and Flemings, 1995; Dutton and Trudgill,

2009; Jackson, 2017).

The final stage is the cessation or inactive stage during which the fault either dies

out or growth ceases. In most cases, faults go through multiple stages of rapid growth that

are interrupted by a period of relative inactivity (Thorsen, 1963). The periodic change in

activity indicates that there is a coupling between fault activity, regional sediment

loading, and regional tectonics.
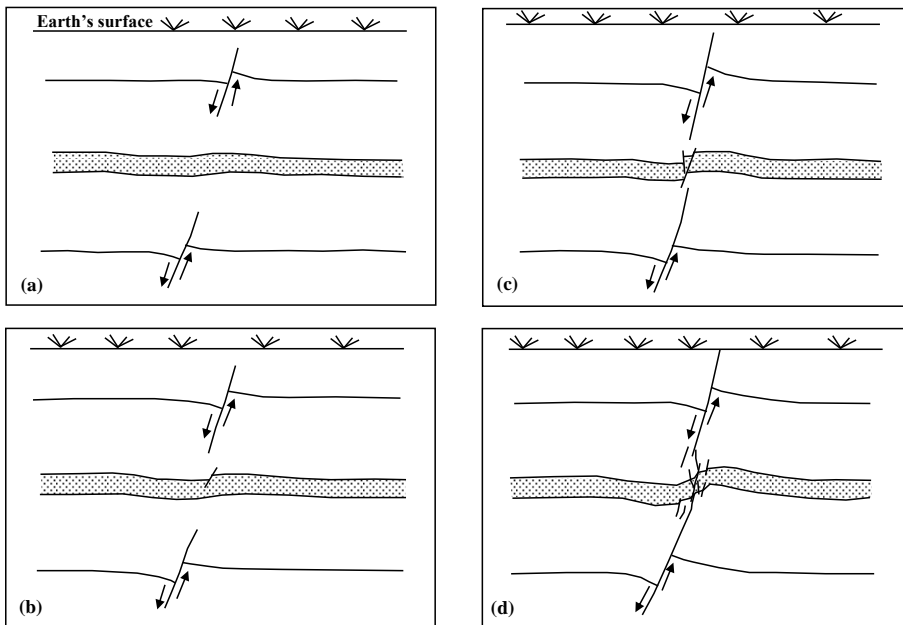
Figure 1.2. A schematic diagram showing the stages involved in the propagation and dip
linkage of a) two initially isolated faults. The upper and lower fault b) propagate towards
each other. A third fault forms in between them. As the upper and lower continue to grow
towards each other, c) the middle strata experience more faulting and folding. The two
faults eventually link at the middle d) to form a single fault. The middle strata is
characterized by severe faulting and folding. Modified after Mansfield and Cartwright
(1996).

The history of fault growth can give us an insight into the formation and evolution

of a basin. Identifying each growth stage of fault history in a salt basin can be used to

interpret the timing of salt deformation, the formation of salt structure, and the timing of

salt withdrawal basins (Alexander and Flemings, 1995; Dutton and Trudgill, 2009;

Jackson, 2017). The displacement pattern of faults can be used to reconstruct the history

of fault to fault interaction and salt-fault interacting in a salt basin. Interaction of faults

with salt usually lead to rapid propagation of a fault in comparison to faults in the

absence of salt. These faults in salt basins have distinct displacement pattern that can be

used in interpretating timing of sediment loading and offloading (e.g., Alexander and

Flemnings, 1995; Dutton and Trudgill, 2009; Jackson, 2017) and timing of interaction

with salt (Tvedt et al., 2016; Tvedt et al., 2013).

1.3 Contribution of this dissertation

This dissertation contributes to the knowledge of salt tectonics with an emphasis

on salt-fault interaction. I studied how coastal wetland loss in a salt basin occurs through

the slip of pre-existing faults that are controlled by salt expulsion. Then I investigated

how fault throw varies along these pre-existing faults and the mechanism that controls the

throw variability. I calculated the throw rates and compared them with other rates within

the Gulf of Mexico and other basins around the world. Lastly, I proposed conceptual

models that explain the growth of fault connecting salt structure. I used kinematic fault

techniques to investigate these models.

1.3.1 Quaternary fault activity in the northwestern margin of the Terrebonne Salt
Withdrawal Basin, southeastern Louisiana

This chapter seeks to address if faults within a salt withdrawal basin in the Gulf of

Mexico were active during the Quaternary. Previous studies have highlighted high fault

activity during the Miocene (McBride, 1998; Peel et al., 1995). Their result indirectly

implies that fault activity had ceased during the Pliocene due to a basinward shift in

depocenter and complete salt evacuation (McBride, 1998). However, the presence of sharp marsh break (Gagliano et al., 2003b), linear salinity anomaly (Kuecher et al., 2001), and coastal subsidence suggest active faulting. In this chapter, I study the throw history of faults within a study area using their throw profiles and sediment distribution pattern. Based on plot and maps, I found that a quiescent Pliocene phase separates periods of rapid fault activity during the Miocene and Quaternary. I also found a link between the subsurface fault and coastal wetland loss. I demonstrate this linkage with a map showing that the surface location of the faults coincides with areas that are experiencing rapid wetland loss.

1.3.2 Spatial and temporal throw variation in the Terrebonne Salt Withdrawal Basin: Effects of sediment loading and diapiric stress perturbation

     In this chapter, I studied the factors responsible for spatial and temporal throw variation on large faults in the Terrebonne Salt Withdrawal Basin. Previous studies focused on the effect of sediment loading on throw rate (Omale and Lorenzo, 2015; Shen et al., 2016). In my study area, the Lapeyrouse-Chauvin area in Terrebonne Parish, southeastern Louisiana, I focused on the throw pattern of two faults, the Isle de Jean Charles and the Lake Boudreaux faults. I looked at how each fault interacts with each other with respect to the overall throw distribution. I discovered that each fault has a unique throw pattern that is influenced by salt evacuation and interaction with adjacent salt stocks. I found that the throw on the Isle de Jean Charles fault is controlled by the kinematic and geometric coherence of the fault array whereas, the intersecting east-west striking faults influence the throw on the Lake Boudreaux fault. Furthermore, stress

perturbation by the Bully Camp salt stock led to an increase in the throw of the Isle de

Jean Charles fault, whereas the diapiric stress of the Lake Barre stock led to a rapid

decrease in the throw of the Lake Boudreaux fault.

1.3.3 Geometry and characteristics of faults connecting two salt stocks: insight from the

Gulf of Mexico

   In this chapter, I address the initiation and propagation of faults that connect two

salt structures. Previous studies have little discussion about the formation of these faults

but focus more on the nomenclature (Rowan et al., 1999) and how the faults suggest the

presence of a deep salt structure (Carruthers et al., 2013; Mattos and Alves, 2018; Tvedt

et al., 2016). I propose three conceptual models to explain the formation of these faults

based on how a fault propagates and interacts with other faults and adjacent stocks. I

tested my conceptual models using data from a salt withdrawal basin, the Terrebonne Salt

Withdrawal Basin, known for its complex fault-salt system. I found that fault that

connects salt stock can form, as proposed by my models, grow by the propagation of a

single fault or by propagation and eventual linkage of two faults. A distinct throw profile

characterizes fault formed by each model. Further, the fault shows a steep throw gradient

at its intersection with salt stock, which I relate to the varying lithology around the salt

stock.

Chapter 2

Quaternary fault activity in the Northwestern margin of the Terrebonne Salt Withdrawal Basin, southeastern Louisiana

Abstract

The kinematic analyses of faults in a salt withdrawal basin can indicate if salt evacuation is completed. In the Terrebonne Salt Withdrawal Basin in the northern Gulf of Mexico, fault activity is presumed to have ceased, and the allochthonous Loann Salt canopy almost evacuated by the end of the Tertiary period due to southward migration of the depocenter. However, geomorphic features along the northern margin of the basin, defined by the Golden Meadow fault zone, suggest that faults are still active in the basin. Using proprietary 3D seismic data from the Lapeyrouse and nearby fields in Terrebonne parish Louisiana, we mapped 10 stratal units based on biostratigraphic data, seismic reflector strength, and continuity. We interpret a discontinuous and complex fault geometry that includes a northwest striking Lake Boudreaux fault, and two east-west striking faults, the Montegut and Isle de Jean Charles. Fault kinematic techniques utilizing throw-distance, throw-depth, isopach maps, throw maps, and expansion indices show that there are two stages of fault activity, a Miocene and a Quaternary stage separated by a Pliocene phase of relative slow activity. Fault activity in both stages corresponds to the time of sediment loading and salt evacuation. The displacement along the Isle de Jean Charles and Lake Boudreaux fault vary laterally towards the Bully Camp

and Lake Barre salt stock, suggesting a coupling between fault movement and salt evacuation. The average Quaternary throw rate, Middle Pleistocene to present, on these faults is 0.53 - 0.65 mm/yr, one order of magnitude larger than those of the Baton Rouge fault zone from Late Pleistocene to present. Surface projection of the large faults shows that their location coincides with surface features including the edge of the cypress swamp near Montegut, historical patterns of wetland loss near Isle de Jean Charles, the Pointe Aux Chene Marina, and the Madison Bay subsidence hot-spot along the Lake Boudreaux fault. We interpret the long-lived patterns of fault activity to correspond primarily to sediment loading, salt evacuation and possible on-going salt deformation.

2.1 Introduction

Fault activity in a salt basin is driven by sediment loading and salt evacuation. Thinning of overburden strata initiates new faults (Vendeville and Jackson, 1992b). The new faults enable salt to rise (Perez-Garcia et al., 2013; Vendeville and Jackson, 1992b). Sediment loading of these faults results in synsedimentary activity, i.e., strata thicken across faults if there is enough sediment supply (Harding and Huuse, 2015; McBride, 1998; Peel et al., 1995; Thorsen, 1963). The differential loading of the basin leads to salt evacuation. The salt flow increases activity on pre-existing faults and influences the formation of new faults, resulting in positive feedback between these processes.

By studying the activity of one of these processes, we can infer or interpret activity on the other processes (e.g., Alexander and Flemings, 1995; Dutton and Trudgill, 2009; Jackson, 2017). Studying fault histories helps to interpret both the timing and the

10

magnitude of these processes. Furthermore, interpreting activity on synsedimentary faults is especially useful in salt basins because fault initiation, propagation, and growth are controlled only by sediment loading and salt evacuation. The effects of other drivers of faulting related to tectonic processes are minimized.
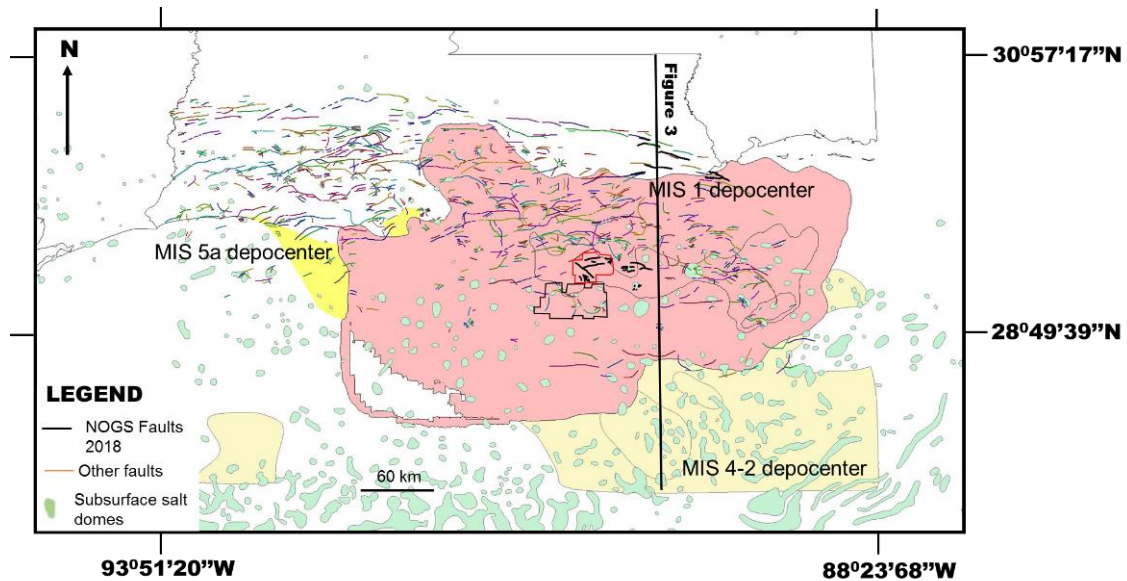
Figure 2.1. Schematic map showing the location of the Terrebonne salt withdrawal basin and the study area. En echelon basinward dipping growth faults mark the northern boundary of the basin whereas salt structures together with counter-regional growth faults mark the southern boundary of the basin. The red box is the location of the Lapeyrouse survey whereas the black box is the Terrebonne 3-D survey shown in Figure 2.2. The black line is a regional cross-section that shows the basin in Figure 2.3. Faults and related salt structures are from the New Orleans Geological Society. Late Pleistocene and Holocene depocenters from Shen et al. (2016) and references therein.

Late Cenozoic salt evacuation along the northern margin of the Gulf of Mexico led to the formation of salt withdrawal basins (Peel et al., 1995; Seni, 1992), including the Terrebonne Salt Withdrawal Basin (TSWB) located in coastal southeastern

Louisiana. This basin (Fig. 2.1), a Miocene and younger structure (Schuster, 1995), is defined at its northern margin by the Golden Meadow Fault zone (GMFZ). Surficial and shallow subsurface evidence suggests salt deformation may be ongoing and impacting ground subsidence and coastal ecosystem boundaries.

Previously Kuecher et al. (2001) constrained the surface trace of the GMFZ using limited well log data and 2d seismic profiles. The authors interpreted evidence of active faulting within the GMFZ through variation in electrical conductivity across several fault traces. These authors identified an east-west striking salinity anomaly south of Houma, Louisiana, along segments of the GMFZ. The observations of high conductivity and high salinity suggest subsurface brine migration to the surface through currently active faults in the northern Terrebonne Bay region.

Gagliano et al. (2003a) used aerial photographs to infer the location of faults in the Laperouse-Chauvin areas. The Montegut fault, south of Montegut, is interpreted based on an east-west sharp-marsh break and the presence of dead cypress trees on the fault's upthrown block. Analysis of shallow cores across the fault indicates an offset of at least 1.4 m (Gagliano et al., 2003a). Similarly, around 1971, a new water body, Lake Boudreaux, appeared in the Bay Madison area. The lake's sharp boundary with the marsh suggests the presence of a fault, the Lake Boudreaux fault. Within the Isle de Jean Charles town's vicinity, there are relict of natural levees that suggest ongoing subsidence. For example, the partially submerged Bayou St. Jean Charles ridge is down-dropped by a fault that corresponds to the inferred surface location of a segment of the GMFZ, the Isle de Jean Charles fault. Despite all these features, the exact location of the faults is unknown.

An explanation for the cause of wetland loss and subsidence in the Lapeyrouse area has been linked to hydrocarbon withdrawal (Morton and Bernier, 2010; Morton et al., 2006; Morton et al., 2005; Morton et al., 2003). According to these studies, oil and gas production leads to a decrease in pore pressure, which increases vertical stress and cause compaction-induced subsidence. The high subsidence rates in the 1970s were correlated to the peak in hydrocarbon production (Morton and Bernier, 2010; Morton et al., 2006) and low subsidence rates in the 1990s and 2000s correspond to a decrease in hydrocarbon production (Morton and Bernier, 2010; Morton et al., 2006). Further, subsidence rates are thought to be low between hydrocarbon fields (Morton and Bernier, 2010). High subsidence is also observed across the inferred surface expression of fault, such as the Isle de Jean Charles fault (Morton and Bernier, 2010).

Morton et al. (2005) analyzed core data from the upthrown block of the IdJC fault in Pointe au Chien. An east-west cross-section of the cores shows the marsh, silt, and mud thickening at the middle portion (Morton et al., 2005). The authors couldn't use a fluid withdrawal mechanism to explain the observed thickening in this area because it does not coincide with any oil and gas field. The calculated subsidence rate in the Lapeyrouse town area based on data obtained between 1966 and 1993 along Highway LA 56, from Houma to Cocodrie is 11 mm/yr (Morton and Bernier, 2010). The minimum subsidence in Madison Bay estimated using core data is 0.65 m (Morton et al., 2006; Morton et al., 2003).

The pattern of subsidence in Grand Isle, Louisiana, due to hydrocarbon withdrawal is compared to the pattern of the subsidence in Galveston, which is attributed to the pumping of groundwater (Kolker et al., 2011). The subsidence rate in Grand Isle

rises steadily at 3.16 ± 1 mm/yr in 1958 to a peak of 9.82 ± 0.33 mm/yr by 1991 and decline by 2006 to 1.04 ± 0.97 mm/yr (Kolker et al., 2011). According to this work, the subsidence trend correlates with hydrocarbon production data in Louisiana, as reported Meckel (2008), which stood at 1.14 x 10^8 barrels in 1945, reach a peak of 4.37 x 10^8 barrels by 1968, and eventually decrease to 5.55 x 10^7 barrels in 2005. This work suggests that the subsidence in Galveston due to groundwater pumping is similar to the pattern of subsidence observed in Grand Isle, which correlates to hydrocarbon extraction and wetland loss (Kolker et al., 2011).

Numerical modeling of compaction-induced subsidence in Madison Bay caused by fluid withdrawal shows that compaction can account for one-third of the observed subsidence (Chan and Zoback, 2007). The value may not represent the subsidence in the area because fault traces used for the modeling are from Kuecher et al. (2001) and may not reflect the structural framework of the Madison Bay area.

Elsewhere in coastal Louisiana, Holocene fault activity is more directly documented. Shen et al. (2016) studied the Pleistocene-Holocene activity of segments of the Baton Rouge fault zone (BRFZ), which is located north of the TSWB. Based on their study, the BRFZ vertical slip rate (throw rate) was 0.03 - 0.04 mm/yr and 0.22 mm/yr during the Late Pleistocene and Late Holocene, respectively. The faster Holocene throw rate was attributed to the shifting pattern of the Mississippi delta lobes towards the BRFZ (Shen et al., 2016). A similar process is expected to affect faults along the GMFZ in the TSWB, i.e., the deposition of Teche and LaFourche delta lobes (Coleman et al., 1998; Roberts, 1997). Earlier Neogene deposition clearly triggered salt flow and accelerated fault activity here (McBride, 1998; Peel et al., 1995); however, it is has not

yet been determined whether the Quaternary sedimentary load led to an increase in fault activity or if it affected the salt structures in the region.

Frederick et al. (2019) argue that the contribution of faults to Quaternary subsidence in coastal Louisiana is relatively small. Using well log data, they mapped eight chronostratigraphic surfaces that range in age from Pliocene to Middle Pleistocene. Their result shows that Quaternary fault activity contributes 4.5% to the total subsidence north of the TSWB. Because their data near Terrebonne Bay is mainly far north of the TSWB, an area with relatively minimal Pleistocene sediment loading, their result can be considered a minimum estimate and does not reflect the true contribution of faulting to the overall subsidence.

Another main process for subsidence in southeastern Louisiana is the compaction of Holocene sediment. This deposit varies spatially in thickness from New Orleans in the north to the basin. The strata thicken basinward from 15 m near New Orleans to an average of 61 m near the shoreline (Heinrich et al., 2015). Further, thickness exceeds 107 m at the Birdfoot Delta, i.e., the modern mouth of the Mississippi River. Some areas have relatively thinner strata that correspond to the subsurface location of salt domes and stocks. Stocks such as Bully Camp, Dog Lake, Four Isle, Lake Barre, and Lake Pelto probably interact with the Holocene-Pleistocene boundary (Heinrich et al., 2015). Others, such as Belle Isle and Cote Blanche Island domes, both in St. Mary Parish, emerge at the surface as outcrops (Heinrich et al., 2015).

Present-day subsidence patterns due to compaction of the Holocene sediment using elevation data acquired between 6-10 years indicate spatial variation in subsidence from New Orleans southward and from Chenier Plain on the west to Birdfoot Delta

(Nienhuis et al., 2017). The average subsidence is about 9 mm/yr but can vary based on the thickness of the Holocene strata. Area with high Holocene thickness, such as the Birdfoot, subsides at ~ 11 mm/yr, whereas regions with thinner Holocene strata i.e., west of the Chenier Plain are subsiding at ~ 7 mm/yr (Nienhuis et al., 2017).

Through dating of peat data from Lafourche, Louisiana Törnqvist et al. (2008) calculated the modern-day compaction rate as 5 mm/yr and a short-term (100 years) rate of 10 mm/yr. In comparison to the elevation record from a compaction-free area located 30 km east of Lafourche, Lafourche Parish experience at least 2-3 m of subsidence due to compaction of Holocene sediment (Törnqvist et al., 2008).

East of the Lafourche is the Barataria Basin. In this basin, the subsidence rate between 2003 and 2019 shows a range between 2-7 mm/yr (Byrnes et al., 2019). The rate increases southeastern, and it is maximum at 7. 1 mm/yr at Grand Isle (Byrnes et al., 2019). The increase in rate towards the southeast corresponds to increasing Holocene thickness and younger deposit (Byrnes et al., 2019).

Usually, when an area subsides, or sea-level rises, vertical accretion of marsh can restore the elevation. However, if vertical accretion is not keeping up with relative sea level, the extent of wetland would diminish (Jankowski et al., 2017). By analyzing 274-rod surface elevation data from Louisiana's Coastwide Reference Monitoring System (CRMS), Jankowski et al. (2017) found that 60% of the total subsidence in the Mississippi Delta is due to shallow subsidence, i.e., from the earth or marsh surface to 20 m below the surface. The result also suggests when vertical accretion is not keeping pace with relative sea-level rise, 35% of wetland within the Mississippi Delta would still strive (Jankowski et al., 2017).
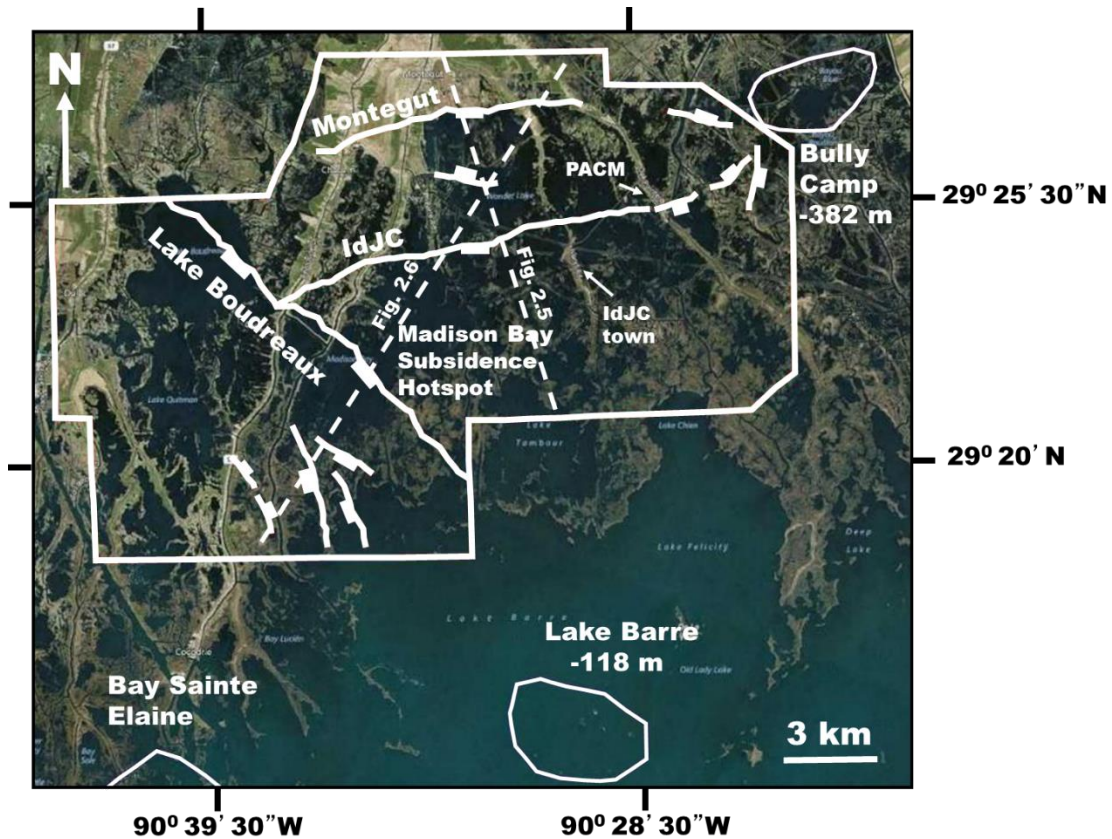
Figure 2.2 Google Earth image with surface traces of major faults (white lines) including Isle de Jean Charles fault, a segment of the Golden Meadow Fault Zone (GMFZ). Faults that intersect the surface are Montegut (M), Isle de Jean Charles (IdJC), Lake Boudreaux (LB), and other faults such as radial faults. The IdJC and LB faults strike towards the Bully Camp (BC) and Lake Barre salt stocks, respectively. These salt stocks, among others, are tabulated by Heinrich et al. (2015) as likely affecting the Holocene – Pleistocene boundary; with depths to the top of caprock of 118 m for Lake Barre and 382 m for Bully Camp (BC). Salt stocks data is from Seismic Exchange Incorporated. The town of IdJC and Pointe Aux Chene Marina lies along the active portion of the IdJC fault. The broken white lines represent the location of the seismic profile in figures 2.5 and 2.6.

To better understand the fault contribution to subsidence and fault-related wetland loss, it is essential to know the fault slip rates during the Quaternary. In this study, I constrain the fault architecture and slip rates for the portion of the TSWB that underlies the northern Terrebonne Bay area. The study area is defined by the extent of the

Lapeyrouse-Chauvin 3D seismic volume (Fig. 2.2), and was chosen because of the availability of 3-D seismic data, the 3D survey's relatively large extent, and an abundance of well data within the survey's area. Additionally, several of the previous studies noted above provide a knowledge-base that is largely lacking in other parts of the TSWB due to difficulties obtaining access to proprietary data and relatively few studies of active faulting.

2.2 Geological Setting

The Gulf of Mexico formed due to the continental rifting of Pangea from the Late Triassic to the Middle Jurassic (Buffler and Sawyer, 1985; Hudec et al., 2013). As Pangea rifted, the South American-African plate migrated away from the North American plate (Hudec et al., 2013). During the Jurassic, the Louann salt precipitated within the restricted marginal marine basin (Buffler and Sawyer, 1985). After the precipitation of the Louann salt, extension continued during the Late Jurassic, causing enough lithospheric subsidence to form a new oceanic crust (Buffler and Sawyer, 1985; Hudec et al., 2013).

During the Eocene, the northern Gulf of Mexico contained an allochthonous canopy of Jurassic Louann salt (McBride, 1998; Peel et al., 1995). Sediment influx from the north began in the Late Eocene and peaked during the Miocene (McBride, 1998; Peel et al., 1995). Because of denser sediment being deposited on less dense salt, coupled with differential loading (Frey and Grimes, 1970; McBride, 1998; Seni, 1992), the salt began to flow basinward and upward (Frey and Grimes, 1970; Ingram, 1991; McBride, 1998; Seni, 1992). The withdrawn salt forms a variety of salt diapiric structures such as stocks,

walls, and domes (Frey and Grimes, 1970; Ingram, 1991; McBride, 1998; Peel et al., 1995; Schuster, 1995; Seni, 1992). These include a salt ridge at the southern margin of the TSWB (Schuster, 1996; McBride 1998; Fig. 2.3). This ridge is topped by several stocks and domes (Abriel and Haworth, 2011; Frey and Grimes, 1970; Ingram, 1991; Rowan et al., 1999) including the Bay Marchand, Timbalier and Calliou Island salt domes (Ingram, 1991; Schuster, 1995; Steiner, 1976).

The loading of this basin with Miocene sediment may have formed new faults and accelerated faults (McBride, 1998). These are basinward dipping growth faults (McBride, 1998; Peel et al., 1995) and landward dipping growth faults that connect adjacent salt domes forming a counter-regional system (McBride, 1998; Schuster, 1995). These faults are detached into Tertiary strata (McBride, 1998; Schuster, 1995). The thickness of the strata increases towards the counter-regional system (McBride, 1998; Schuster, 1995).

The Pliocene was marked by relatively little sediment storage, with the main depocenter lying south of the TSWB (Galloway, 2001); this resulted in a slowing of fault activity. Later, the northeast portion of the Pleistocene Sangamonian Marine Isotope Stage (MIS) 5e depocenter fell within the TSWB (Galloway, 2001). The remaining Pleistocene and Holocene sediments coincide with the TSWB's northern margin (Fig. 2.1) and mark the approximate northern extent of MIS 4, 3 and 2 depocenters (Coleman and Roberts, 1988b), i.e., sediment deposited during glacial, interglacial and glacial periods, respectively. Because of this differential loading, faults and salt structures that formed during the Miocene may have been rejuvenated in the Quaternary.
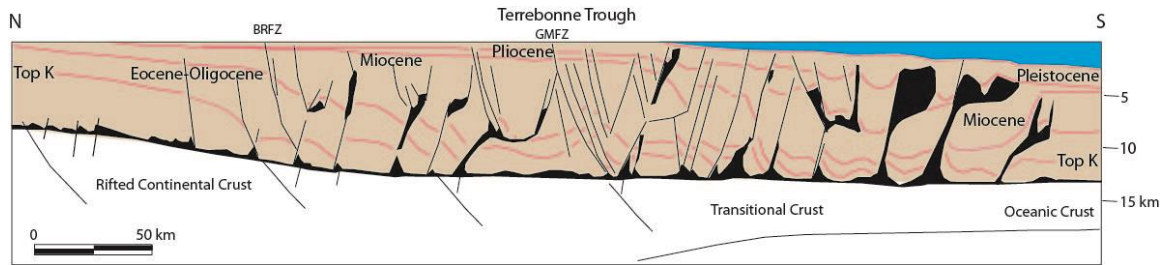
Figure 2.3. Highly generalized geological cross-section of southeast Louisiana showing strata thickening towards the basin. Basinward dipping listric faults mark the basin's northern boundary, whereas landward dipping fault and salt stock mark the southern boundary of the TSWB. Modified from McBride (1998). This cross-section extends from latitude 31^0N to 25^013'N. See Figure 2.1 for the location of the cross-section.

2.3 Data and Methodology

2.3.1 Data

Well logs are 1-D representations of changes in physical properties of rock and fluids they may contain. The logs used in this study were obtained from the online database of Louisiana Department of Natural Resources, which is known as the Strategic Online Natural Resources Information System, or SONRIS. These logs are primarily gamma ray (GR), spontaneous potential (SP) and resistivity logs. On each log, the top of the 850 m (2700 ft) sand was obtained from Kolvoord et al. (2008). The shale unit above it which we refer to in this study as the 760 m (2500 ft) shale, and other tops were also picked and mapped (Fig. 2.4). The depth of the well tops were imported into Kingdom Suite software loaded with 3-D seismic data, and the equivalent seismic reflectors were mapped.

Three dimensional (3D) seismic data provide detailed information on relationships between subsurface stratigraphy and structure. A large 3D surveys form the basis of this study. The Lapeyrouse 3D survey (Fig. 2.2) is a merged data volume owned

by Seitel and encompasses an area of 531 km^2. The dataset have a normal polarity, i.e., a peak represents an increase in acoustic impedance as the seismic wave travels from a less dense stratum to a denser one. The seismic volumes contain a grid of north-south inlines and west-east crosslines. The inlines are perpendicular to the regional structure (i.e., fault strike); the crosslines are parallel to the regional structure (west-east). Inline and crossline spacing for the Seitel is 110 ft.

Geologic Age	Stratal Unit	Index Fossil	Reflector mapped	Age (Ma)
Quaternary	SU 10		Z1	?
	SU 9		760 m Shale	?
		Angulogerina B	850 m Sand	1.54
Pliocene ?-	SU 8		M1	?
	SU 7		M2	?
?-	SU 6		M3	?
	SU 5			
Miocene	SU 4	Bigenerina A	Big. A	7.39
	SU 3	Amphistegina E	Amph. E	7.84
	SU 2	Discorbis 12	Dis. 12	9.18
		Textularia L	Tex. L	9.71
	SU 1	Cibicides Cartensi	Cib. C	10.63

Figure 2.4. The chart shows the seismic reflectors mapped and their corresponding biostratigraphy ages. A seismic reflector corresponds to the top and base of each stratal unit (SU). The reflectors were group into 10 stratal units from the oldest, SU 1 to the youngest, SU 10. Biostratigraphic ages are from PaleoData biostratigraphic chart- Gulf Basin, USA version January 16, 2017

The 3D seismic data interpretation, using IHS Kingdom Suite, started with fault

interpretation. Faults were interpreted on a seismic section where there is displacement of

seismic reflectors. The faults were digitized from the shallow reflectors to the deep

reflectors on every 10 inlines, in addition to arbitrary lines, and were subsequently tied to

the crosslines. Horizons were digitized on reflections having geological significance

every 20 inlines and every 20 crosslines across the 3D seismic volume. Horizons

mapped include those based on the 'formation tops' from Kolvoord et al. (2008),

biostratigraphic picks obtained from PaleoData (Fig. 2.4), and horizons chosen because

of seismic reflectivity and continuity. The horizons and faults were used to generate time

structure maps, i.e., maps produced in two-way travel time. These maps were converted

into depth structure maps by multiplying them by a time-depth chart or velocity survey

using data donated by Velocity Databank Inc. The difference between two successive

depth structure maps was used to compute the thickness of a stratal unit (SU) and

generate isopach maps.

2.3.2 Fault Kinematic Techniques

Data from depth structure maps are used for fault kinematic analyses. These

maps contain information on depths to horizons, fault throw (vertical component of total

displacement), and thickness. The fault data are displayed as throw (T) versus depth (z)

plots, throw (T) versus lateral distance (x) plots, expansion indices (E.I.), and throw

maps. T-z plots identify the timing of activity on syn-depositional faults (e.g., Cartwright

et al., 1998). An active time interval for a syn-depositional fault is expressed as a positive

gradient, i.e., the displacement decreases upward until a free surface is intersected

(Baudon and Cartwright, 2008a). A period of fault inactivity is indicated by a zero gradient (Cartwright et al., 1998).

T-x plots, i.e., throw along the fault trace from one tip to the other or into adjacent salt, are generated using Badley Geoscience's Traptester 7 (T7) software. Throw gradients and segment geometry are used to determine if a large fault formed by fault linkage (e.g., Willemse et al., 1996; Cowie and Roberts, 2001). T-x patterns of linked faults are characterized by anomalous gradients and local displacement minima. The change in displacement will be better resolved with a data spacing of 61 m (200 ft) because the smaller the sampling density, the better the quality of maps and resolution of data (Mansfield and Cartwright, 1996).

Mapping of fault throw on the fault plane is also useful for establishing the timing of activity (e.g., Childs et al., 2003). Badley's T7 software is used to generate throw maps. These maps identify syn-sedimentary intervals, which are characterized by horizontal to sub-horizontal throw contours in contrast with non-growth intervals characterized by vertical to concentric contours (Childs et al., 2003). The T-z data and throw maps are also used to interpret interaction between faults and adjacent salt structures (e.g., Baudon and Cartwright, 2008; Tvedt et al., 2013 and Tvedt et al., 2016).

Thickness variation of sedimentary strata also record growth intervals. First used by Thorsen (1963), the expansion index (E.I.) is the ratio of hanging wall stratal thickness to the footwall thickness. Thus intervals that have an expansion index of 1 did not experience fault activity whereas intervals with EI> 1 indicate that the fault was active while the sediment was being deposited. It is useful here in that there is a high sediment supply relative to slip rate (Childs et al., 2003; Jackson et al., 2017; Thorsen, 1963).

23

2.4. Results

2.4.1 Fault Architecture

The mapping of eleven reflectors show that three large faults define the structural framework of the Lapeyrouse area. These faults are a northwest-striking fault referred herein as the Lake Boudreaux fault, and two east-west striking faults, the Montegut and Isle de Jean Charles faults (Figs. 2.3, 2.5, 2.6 and 2.7). The Lake Boudreaux fault dips southwest whereas the Montegut and Isle de Jean Charles faults dip southward. There is also an east-west striking fault on the hanging wall of the Lake Boudreaux fault (Fig. 2.7a). This fault, which I refer to as the Dulac fault, is only partially contained in the Lapeyrouse survey and bisects the Lake Boudreaux fault into northern and southern segments. It is unclear if this fault is a segment of the Isle de Jean Charles fault, which lies along-strike to the east. The Isle de Jean Charles fault extends westward to the Lake Boudreaux fault, but neither clearly offsets the other suggesting they have both been active over similar times. Unlike the Lake Boudreaux fault, the Isle de Jean Charles fault is a right-stepping en echelon fault. It is made up of three segments; IdJC1, IdJC2, and IdJC3 (Fig. 2.7b). The western segment, IdJC1, interacts with the Lake Boudreaux fault, the eastern IdJC3 interacts with a radial fault from the Bully Camp salt stock, whereas the middle segment, IdJC2, interacts with the two other segments.

The Montegut fault intersects but does not offset the Lake Boudreaux fault. Along with the large faults, radial faults associated with the Bully Camp salt stock and other minor faults are also interpreted. One of the radial faults interacts with the eastern segment of the Isle de Jean Charles fault (Fig. 2.7) and suggests that the Isle de Jean Charles fault probably propagated from the Bully Camp salt stock.
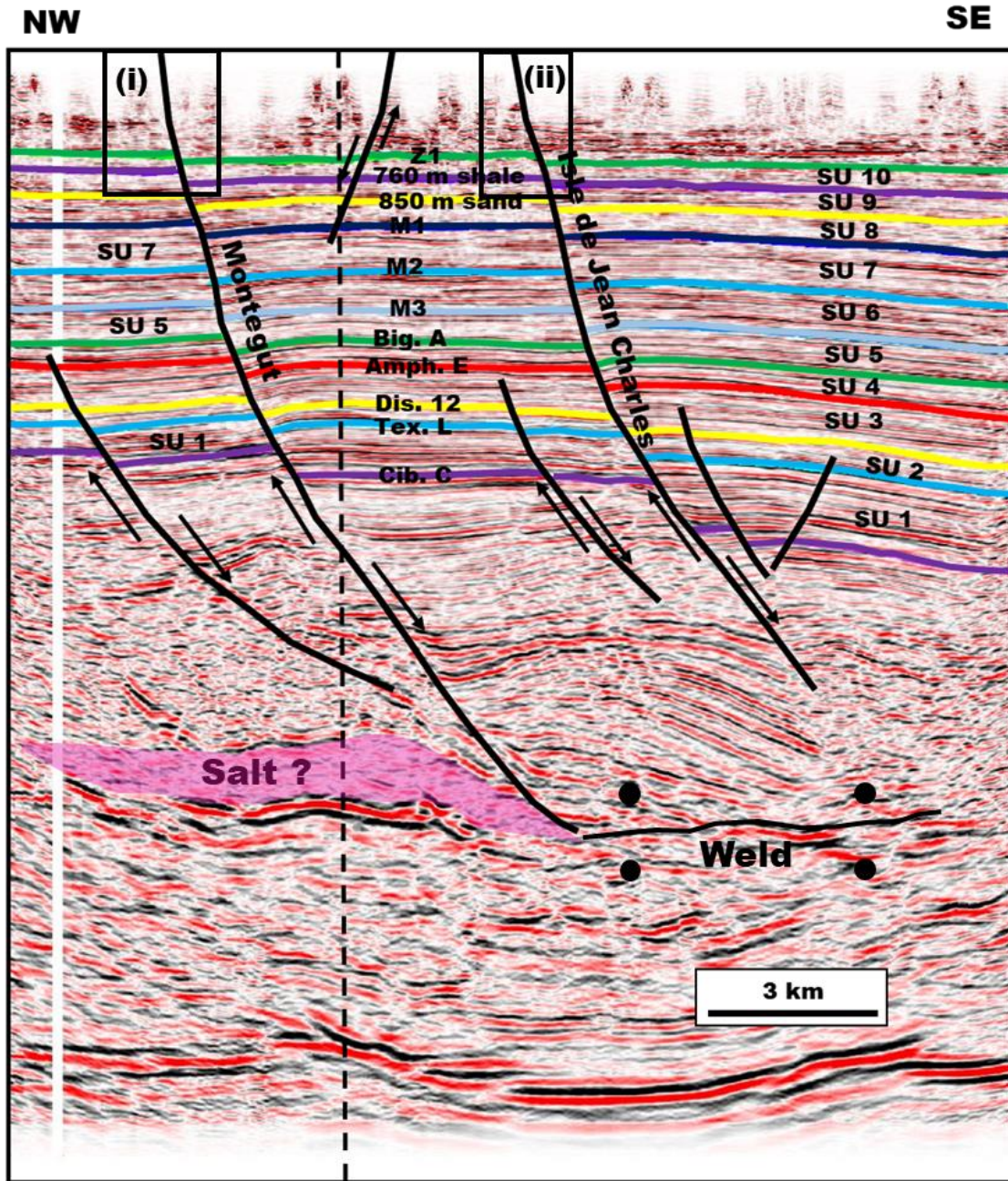
Figure 2.5a. A northwest to southeast seismic profile through the 3D seismic volume. The Montegut and Isle de Jean Charles faults offset the youngest Quaternary stratal unit, SU 10. Stratal thickening is interpreted on the hangingwall of Montegut fault for SU 10. Both faults extend to the top of the seismic profile. Insert (i) and (ii) are shown in Figure 2.5b. See Fig. 2.2 for the location of the section. The broken black line represents the point of intersection of figure 2.6.

25
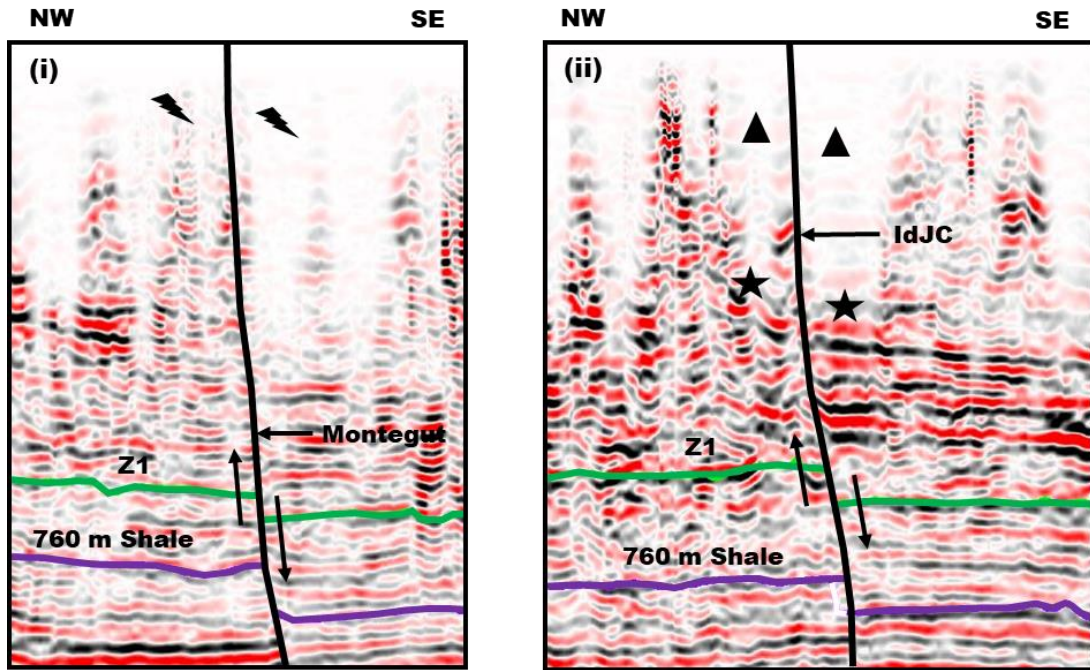
Figure 2.5b. Displacement of shallow reflector by the (i) Montegut and (ii) the Isle de Jean Charles faults. Shapes show similar reflectors on both side of the fault.
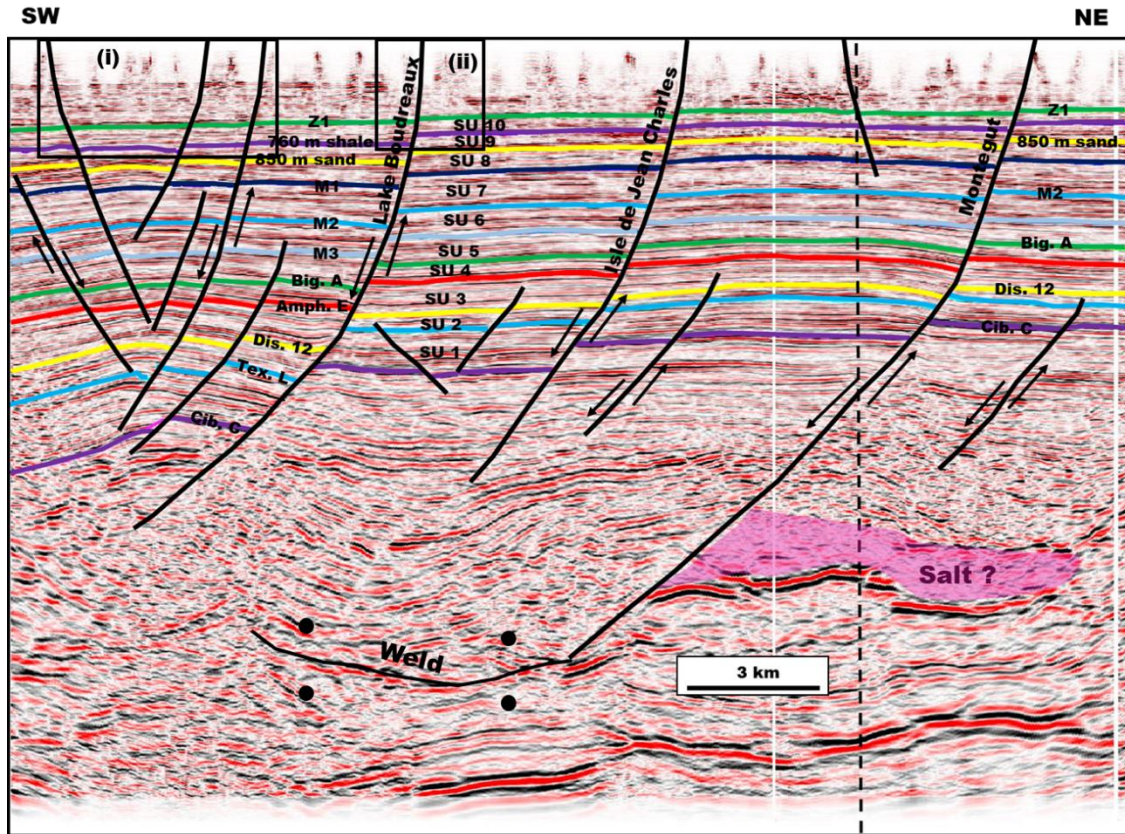
Figure 2.6a. A southwest to northeast seismic profile through the 3d seismic volume showing the Montegut, Lake Boudreaux, and Isle de Jean Charles faults. Fault displacement extends to the top of the seismic volume. Strata thicken from the northeast towards the graben on the hanging wall of Lake Boudreaux fault. For example, SU 10 thickens across the Montegut in the northeast, to the Lake Boudreaux in the southwest. Insert (i) and (ii) are shown in Figure 2.6b See Figure 2.2 for the location of seismic profile. The broken black line represents the point of intersection of figure 2.5.
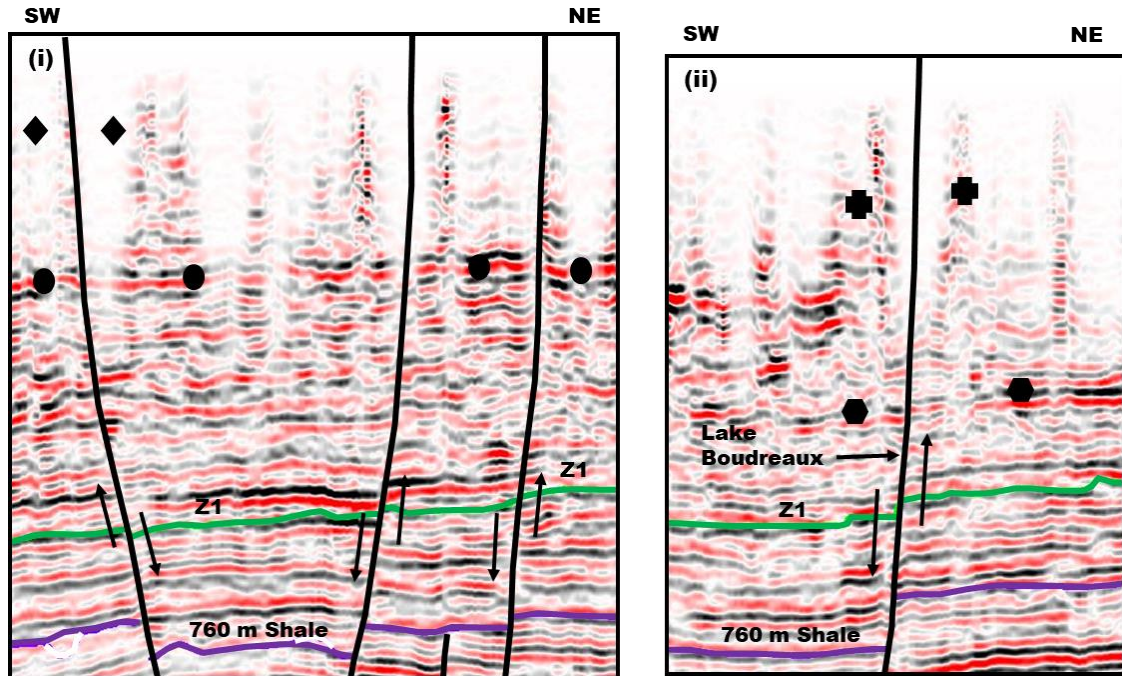
Figure 2.6b. Displacement of the shallow reflectors by the (i) the graben faults southwest of Lake Boudreau fault and (ii) the Lake Boudreaux fault. Shapes show similar reflectors on both sides of the fault.

2.4.2 Relative Timing Of Growth

A visual inspection of the seismic profiles indicates that faults extend to the top of the 3D seismic volume (Figs. 2.5 & 2.6). Stratal thickness increases across faults from the Montegut fault at the northeast towards the graben system on the hanging wall of Lake Boudreaux fault. For example, the Late Quaternary SU 10 show an increase in thickness across the three large faults into the graben system.

2.4.2.1 Isopach maps

The isopach maps (Fig. 2.7) show that the large faults were active from the Miocene to the Quaternary. At the beginning of the Late Miocene, SU 1, the southeast

28

segment of the Lake Boudreaux fault was more active than its northwest counterpart and the east-west striking faults. The relative thickness across southeast LB is approximately 600 m. The strata further thicken towards the southwest. Strata thickness varies from west to east along IdJC, whereas they are uniform on the Montegut fault. By SU 2 (Fig. 2.7b), the entire length of Lake Boudreaux remains active, especially the southeast portion of the fault. About 520 m of strata accumulated on the southeast hangingwall compared to 200 m on the footwall, whereas the relative difference in thickness on both sides of the Montegut fault is approximately 20 m. Furthermore, the three segments of IdJC fault become visible.

A local depocenter forms, by SU 3, around the two eastern segments, IdJC2 and IdJC3 (Fig. 2.7c). At the same time, the western portion of Montegut show a record of high sediment accumulation (thicker stratigraphy) and southeast Lake Boudreaux fault still record a relatively high sediment accumulation rate compared to its northern segment. By SU4, little variation in strata thickness is recorded across the Lake Boudreaux fault (Fig. 2.7d). The two segments of the Dulac fault, Dulac-North and Dulac South, cease to interact with the main Dulac fault (Dulac-center). As for the E-W faults, little across fault thickness is interpreted across IdJC2, IdJC3, the western and eastern portion of Montegut. By the end of the Miocene (SU5), the main Dulac fault was no longer interacting with the Lake Boudreaux fault; hanging wall strata thickness began to even out (Fig. 2.7e). At the same time, deposition was concentrated along the eastern portion of the Montegut fault, western portions of IdJC1, and the entire length of IdJC2, and IdJC3.
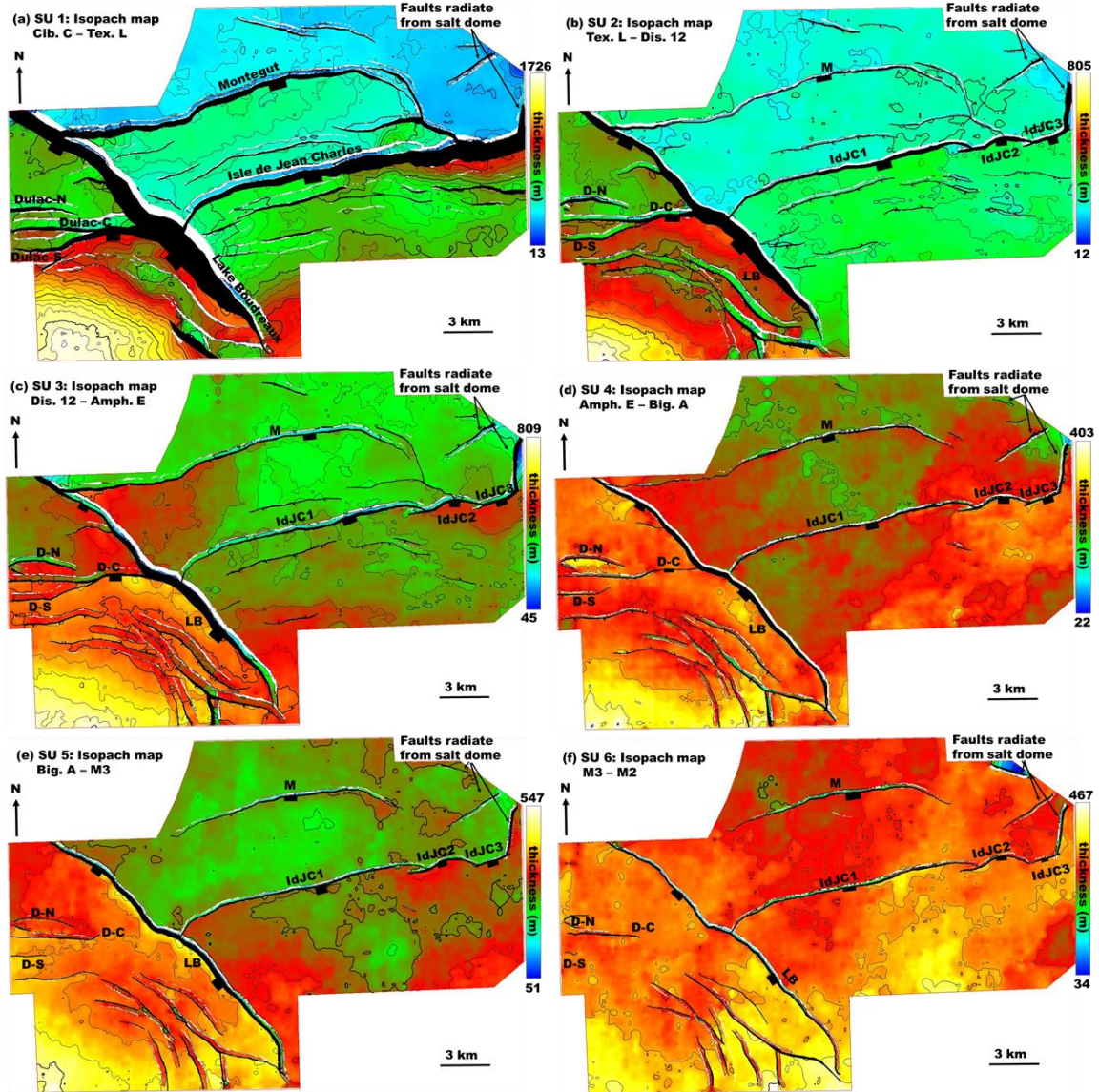
Figure 2.7. Isopach maps for SU 1 to SU10. Strata thicken across the northwest striking Lake Boudreaux fault and the east-west striking faults, Montegut and Isle de Jean Charles. The east-west striking faults interact with the Lake Boudreaux fault. The IdJC fault becomes a right steeping en echelon fault (b) by the beginning of SU 2. The Lake Boudreaux fault is divided into two segments (a-d) by the east-west striking Dulac fault. Strata thickness varies spatially along strike of the large faults, especially for Isle de Jean Charles and Lake Boudreaux fault because of interaction with the Bully Camp and the Lake Barre salt stock, respectively. Continuous white lines on (j) represent location of seismic profiles in Figures 2.5 and 2.6. Short black lines across the faults indicate the location of data for the T-z plot and expansion indices.
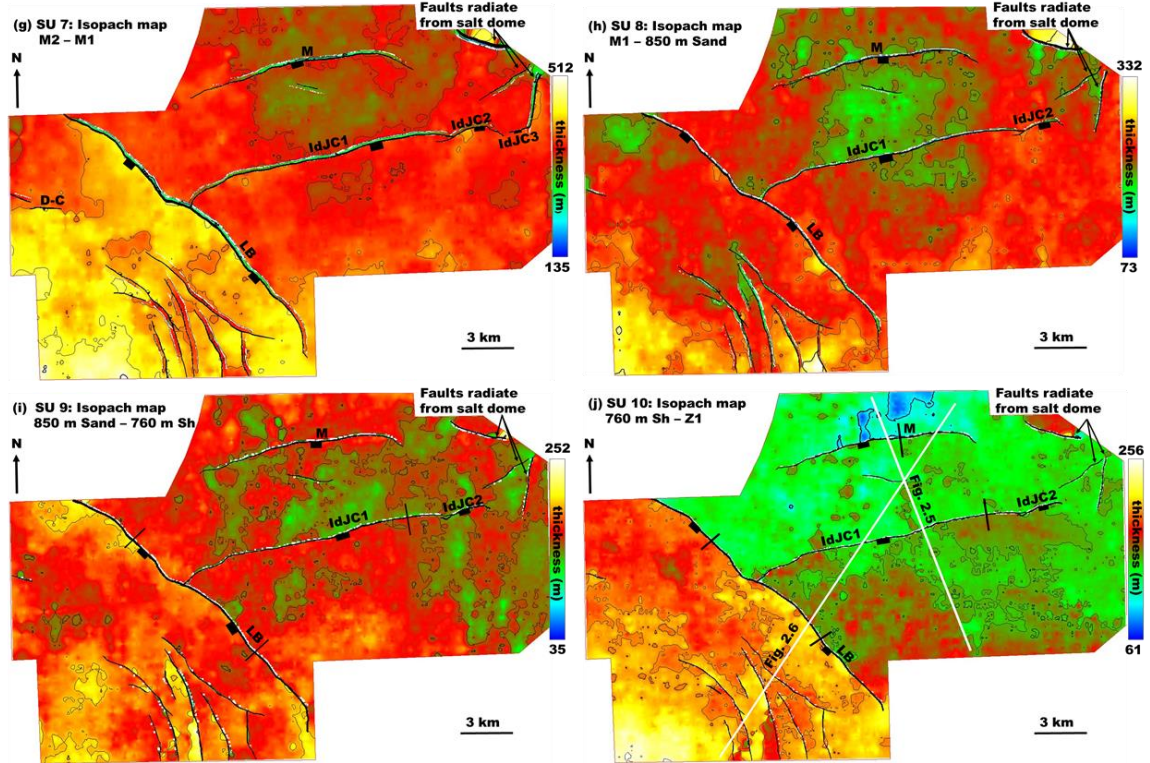
Figure 2.7 continued

The beginning of SU6 is marked by little across fault strata thickening (Fig. 2.7f).

Few locations along the large faults indicate active faulting such as southeastern Lake

Boudreaux, eastern IdJC1 and the western portion of IdJC2. By SU 7, the entire length of

Lake Boudreaux was active with its hanging wall accumulating a differential thickness of

50 m whereas the center portion of IdJC1 and IdJC2 records a differential thickness of 10

m and 40 m, respectively (Fig. 2.7g). By SU 8, across fault thickening was restricted to

the centers of southeast LB, IdJC1, and the interacting area of IdJC and Lake Boudreaux

faults (Fig. 2.7h). Furthermore, IdJC3 did not cut through this strata unit, and thus the

link between IdJC and the radial fault was broken.

31

The middle Pleistocene, SU 9, is by marked active fault growth. Strata thicken

across 70% of IdJC1 with the locus of deposition at the fault center (Fig. 2.7i). Evidence

of thickening is also interpreted at the northernmost and southernmost portions of the

Lake Boudreaux fault. By the late Quaternary SU 10, the Lake Boudreaux fault once

again becomes the most active of the three large faults with strata thickening across its

entire length (Fig. 2.7j). An increase in strata thickness across the center of Montegut

fault, the western and eastern portion of IdJC1, and the western portion of IdJC2 suggest

an increase in fault activity.

2.4.2.2 Throw vs. Depth plot

The T-z plot (Fig. 2.8) shows a general decrease in throw from the Miocene to the

Quaternary. During the late Miocene *Cib. C*, the throws of the large faults were very high

with the Montegut having a throw of 187 m, 461 m for IdJC, 681 m for northwest LB and

963 m for southeast LB. The fault throw decreases rapidly upsection from *Cib. C* to *Dis.

12* especially for IdJC and Lake Boudreaux faults. However, during the deposition of

Amph. E, IdJC and northwest Lake Boudreaux show an abrupt increase in throw. The

throw of the IdJC increased by 20 m, whereas that of the northwest Lake Boudreaux

increased by 55 m. On the other hand, the throw of Montegut and southeast Lake

Boudreaux decreased by 41 m and 47 m respectively. From *Amph. E.* up to the end of the

Miocene (*Big. A*), faults throw continue to decrease up section with a calculated gradient

of 0.03 for Montegut, 0.16 for IdJC, 0.1 for northwest Lake Boudreaux and 0.33 for

southeast Lake Boudreaux faults. In comparison to the latest Miocene gradient, the fault

gradient from *Cib. C* to *Dis. 12* is 0.06 for Montegut, 0.33 for IdJC, 0.48 for NW Lake

Boudreaux and 0.53 for SE Lake Boudreaux faults. Fault throw continued to decrease up section from M3 to M1 at a much slower pace, i.e. low gradient with computed gradient as low as 0.03 for Montegut, 0.03 for IdJC, 0.01 for northwest Lake Boudreaux and 0.08 for southeast Lake Boudreaux faults. However, from the deposition of the middle Pleistocene 760 m Shale to the deposition of the late Quaternary Z1, there was an abrupt increase in throw gradient. The calculated gradients are 0.19 for Montegut, 0.09 for IdJC, 0.37 for northwest Lake Boudreaux and 0.33 for southeast Lake Boudreaux faults.
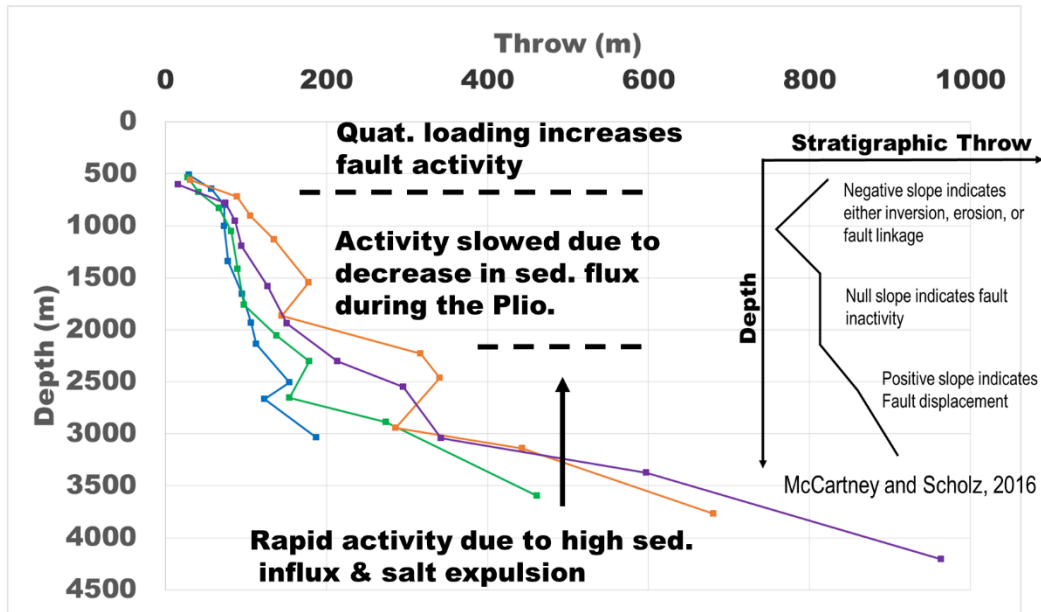
Figure 2.8. A plot of Throw against Depth (T-z) for Montegut (Blue), IdJC (Green), NW LB (Orange) and SE LB (Purple). Displacement generally increases with depth. Fault activity varies from the Miocene to the Quaternary due to varying rates of salt evacuation influenced by varying rates of sediment influx and loading. The Miocene and Quaternary stages of fast activity are characterized by high gradient whereas the Pliocene phase of low activity is characterized by low gradient. The location of data points for T-z plot is shown in figure 2.7j. The insert is a conceptual image of T-z plot is from McCartney and Scholz (2016).

2.4.2.4 Expansion Index plot

At the beginning of the Late Miocene (SU 1), the three large faults showed evidence of rapid movement as suggested by high E.I with a value range from 1.3 for IdJC to 1.5 for southeast Lake Boudreaux fault (Fig. 2.9). Activity further increases during SU 2 for the IdJC and the Lake Boudreaux faults with both recording E.I. values of 1.7 and 2.3 respectively whereas E.I. decreases for the Montegut fault. The deposition of SU 3 records a decrease in E.I. value to approximately 1.1 except for northwest Lake Boudreaux with a value of 0.9. The E.I. remained at approximately 1.1 during SU 4 except for southeast Lake Boudreaux fault which showed a relative increase in activity with an E.I value of 1.4. By the end of the Miocene (SU 5), only the northern segment of Lake showed an increase in activity whereas activity on the east-west striking faults remains the same.

The expansion indices for Strata Unit 6 to Strata Unit 8 are very low. The index varies from 0.9 to 1.1 and suggests slow rates of faulting. However, at the beginning of the Quaternary period (SU 9), the Montegut and IdJC whose E.I. values had fluctuated around 1.05 from SU 6 to SU 8, started showing evidence of resume fault activity with E.I values of 1.1 and 1.2 respectively. At the same time, E.I. value of both segments of the Lake Boudreaux fault was similar to their Pliocene values. However, by the Late Quaternary period (SU 10), both segments of Lake Boudreaux fault shows evidence of rejuvenation of activity based on an increase in E.I. value from 1.1 during SU 9 to at least 1.4. The expansion index of the Montegut fault also increases to over 1.2 during SU 10.
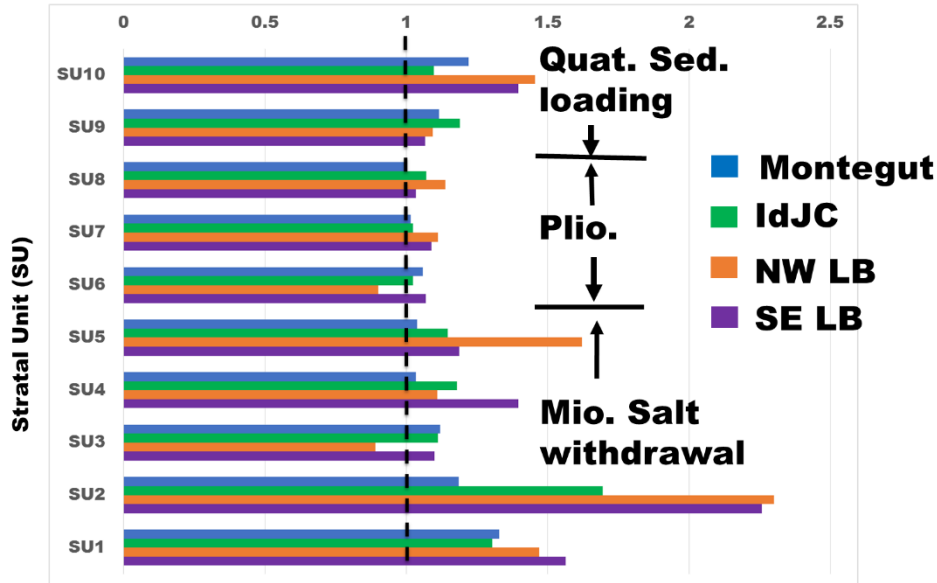
Figure 2.9. Expansion indices for the large faults. The plot shows fast fault activity, and high E.I., at the beginning of the Late Miocene from SU1 to SU 2. The decrease in E.I. from SU 3 to SU 5 indicates a decrease in fault activity towards the end of the Miocene. During the Pliocene, SU 6 to SU 8, low E.I. values suggest that activity remains minimal. However, there is a rejuvenation of fault activity during the Quaternary. This is recorded by the high E.I. value, especially for the Lake Boudreaux fault, for SU 10. The location of data points for the E.I. plot is shown in figure 2.7d.

2.4.3 Displacement profiles and throw maps

2.4.3.1 Montegut Fault

2.4.3.1.1 Throw vs. Distance plot

The throw vs. distance plot for the Montegut fault (Fig. 2.10) is asymmetrical from *Cib.C* to *Amp. E* whereas it is generally symmetrical from *Dis. 12* to Z1. The throw of the Late Miocene *Cib. C*, *Tex. L*, *Dis. 12* and *Amph. E* decreases from the point of intersection with the Lake Boudreaux fault on the west towards the east. However, throw increases at 6 km along strike. The throw continues to fluctuate until approximately 17 km where it began to decrease towards the east. A maximum drop in throw of 230 m is

recorded between *Cib. C* and *Tex. L.* From *Tex. L* to Z1, the throw gradually decrease

from the older reflector to the younger reflector. No throw values were computed for

Big. A to Z1 for the first 7 km of the first because by *Big. A*, the Montegut fault had

stopped interacting with the Lake Boudreaux fault and had laterally retreated eastward.

The maximum throw for *Big. A* to Z1 is located between 15 km to 18 km.
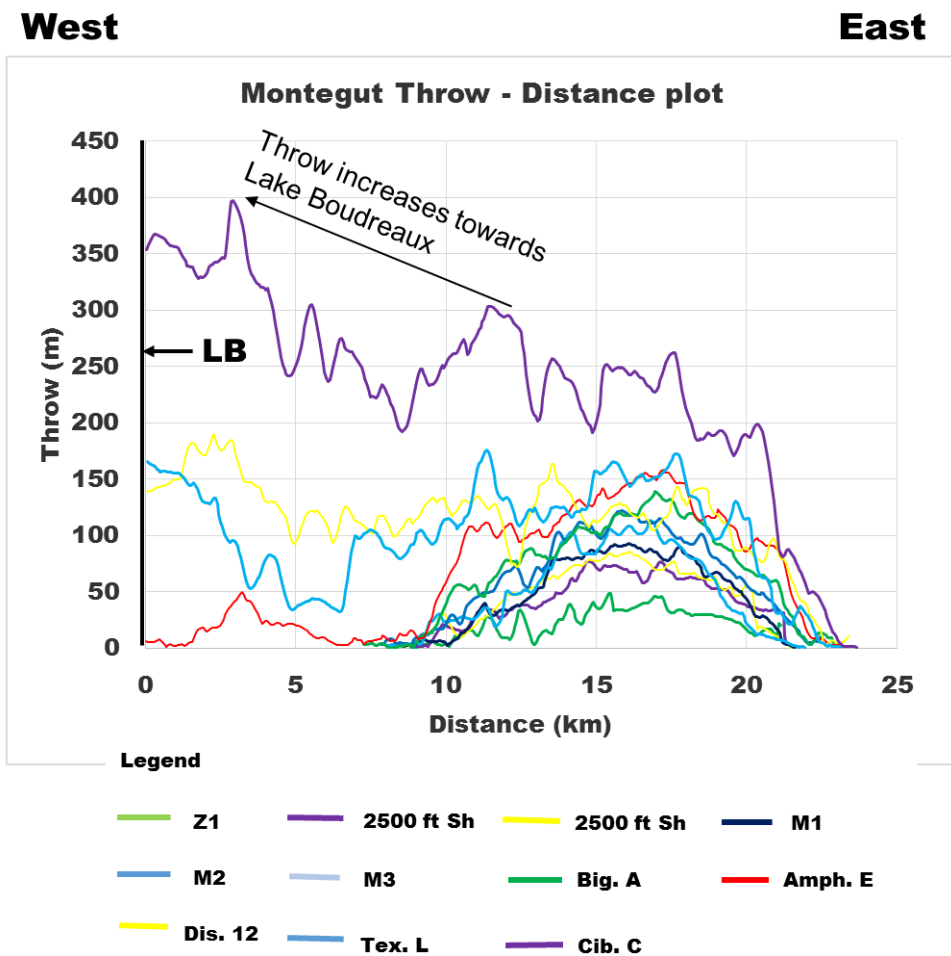
Figure 2.10. Throw vs. Distance plot (T-x) for the Montegut fault. Throw increase westward towards the Lake Boudreaux fault until the end of *Amph. E*, at which time the fault had stopped interacting with the LB. The displacement profile becomes symmetrical from *Big. A* to Z1.

2.4.3.1.2 Throw map
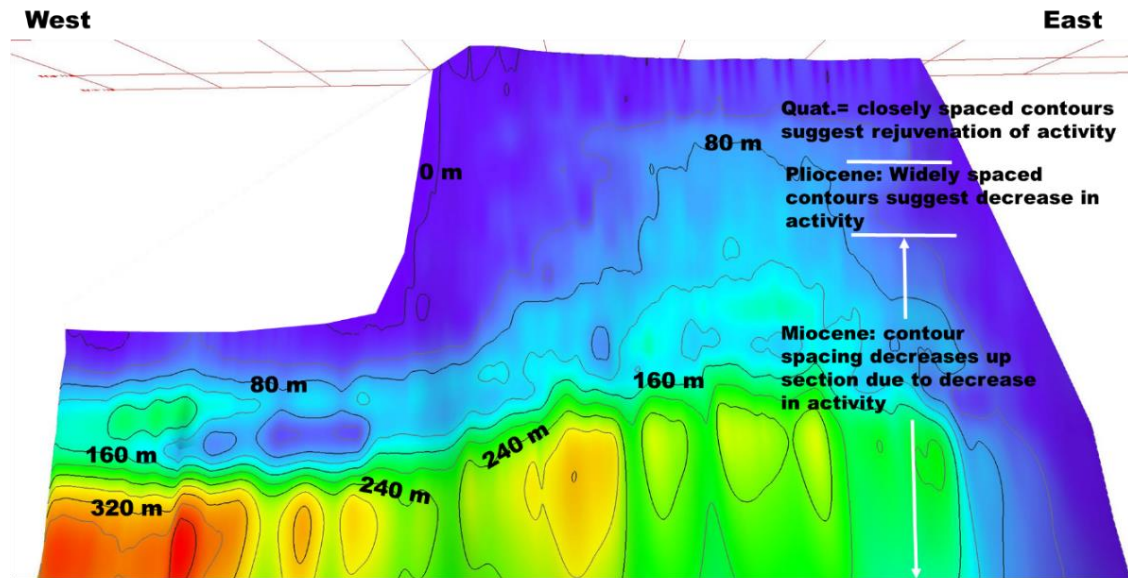
Figure 2.11. Throw map for Montegut fault. At the bottom of the map, throw increase westward toward the Lake Boudreaux fault. Contour spacing increases to the top of the map suggesting a decrease in fault activity.

The contours patterns and distribution of this fault suggest spatial and temporal throw variation (Fig. 2.11). The bottom of the map shows at least six distinct areas of high contour values that are elliptical. The structural high at the western portion of the map has the highest contour value of 400 m. Furthermore, contour lines in this area are more closely spaced compared to those at the fault center. Temporally, contour spacing increases upsection towards the middle portion of the map. By the latest Miocene (map middle portion), closely spaced contours at the map's western portion suggest rapid fault movement whereas the eastern portion show widely spaced contours indicating relatively slow fault activity. During the Pliocene, the contour spacing further increases, at the east portion, towards the top of the map. At the same time, at the western portion of the fault,

contour approaches zero. However at the uppermost portion, Quaternary section, a decrease in contour spacing with contour have a horizontal to sub-horizontal pattern suggesting syn-depositional across the fault.

2.4.3.2 Isle De Jean Charles Fault

2.4.3.2.1 Throw vs. Distance plot

The throw vs. distance plot for IdJC fault (Fig. 2.12) is asymmetrical and skewed towards the east. The throw generally increases eastward, i.e., from Lake Boudreaux fault to the Bully camp salt stock. This plot shows three areas of throw maximal which are separated by throw minimal at 15 km and 20 km. Displacement on the third throw maximal increases towards the Bully Camp salt stock. At 20 km, i.e., 5 km from the salt stock, the Late Miocene *Cib. C* record a maximum throw of approximately 1000 m. There is a rapid decrease in throw between the older *Cib. C* and younger *Tex.L*. Unlike the *Cib. C*, the maximum throw of *Tex. L* is 316 m, and it is located close to the east tip of IdJC1. There are two other throw maximum at 17.7 km and 22.5 km. From *Tex. L* to *Big. A,* the first throw maximal which is usually located at about 14 km along the fault, began to migrate westward. The second maximal on the other hand alternated between the west tip and center of IdJC2. At the same time, IdJC3 throw continues to increase eastward. By the beginning of M3, the location of maximum throw for both IdJC1 and IdJC2 continue to move towards the center of both fault segments. The maximum throw is located at the center of both IdJC1 and IdJC2 during the Quaternary.
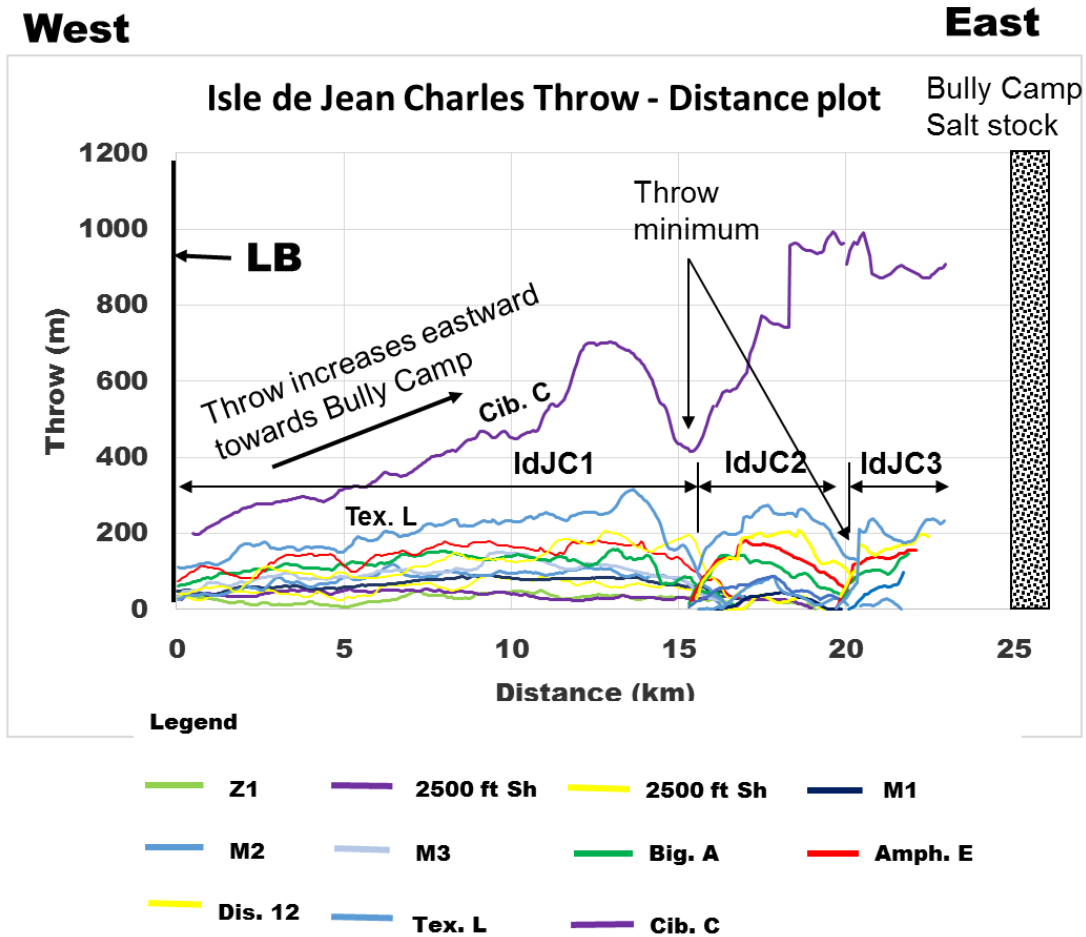
Figure 2.12. T-x plot for Isle de Jean Charles fault (IdJC). Throw increase eastwards towards the Bully Camp salt stock. Throw minimal occur at the tip of each segment of IdJC. The maximum throw for each segment is located at the eastern tip for IdJC1, shift between the western tip and the center fro IdJC2, and located at the west tip for IdJC3

2.4.3.2.2 Throw map

The throw map of this fault suggests spatial and temporal throw variation (Fig. 2.13). This is based on contour patterns and spacing. At the bottom of the map, there are three distinct areas of structural highs with sub-horizontal to horizontal contour lines with contour value increasing downward towards a closed elliptical contour. These structural highs are separated by areas of vertical contour lines with low contour value.

39
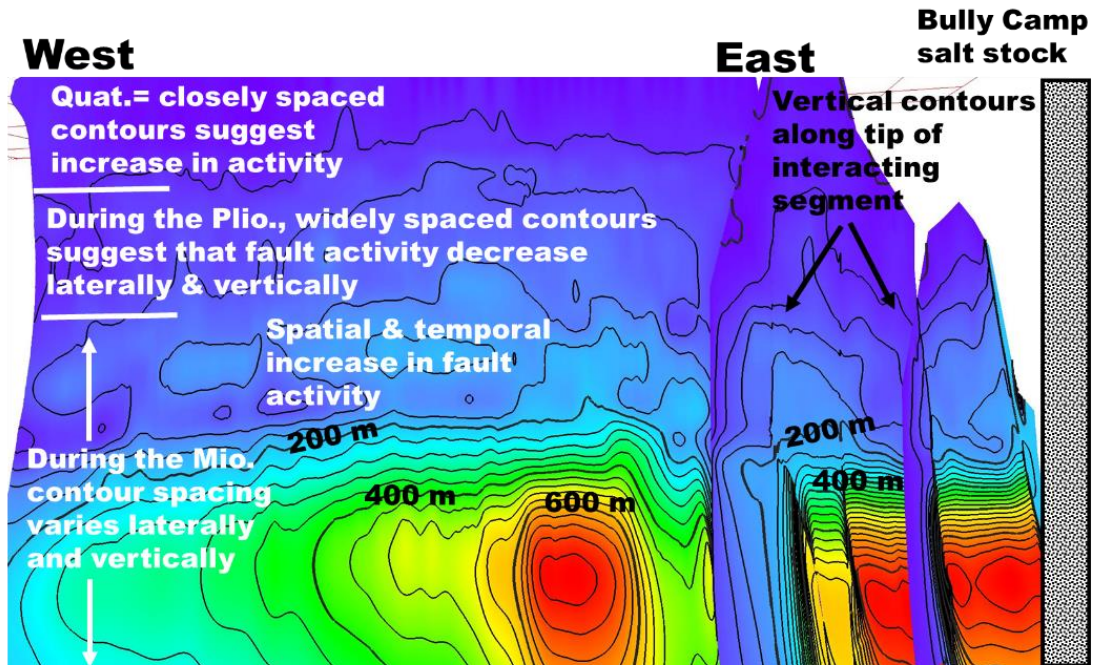
Figure 2.13. Throw map for Isle de Jean Charles fault. Activity varies temporally and spatially as seen in variation in contour spacing from west to east and from top to bottom of the map. Contours spacing decrease eastward towards Bully Camp stock suggests rapid fault activity influenced by salt evacuation. Three structural highs marked the point of maximum throw on the three fault segments. The fault segments represented by structural highs are separated by an interval of vertical contour lines. The decrease in contour spacing, from the Miocene to the Pliocene, indicates a decrease in fault activity. However, relatively closely spaced contour is interpreted in the Quaternary suggests rejuvenation of fault activity. C.I. is 40 m & V. E. is 10

The first area of structural high extends from the west, where the fault interacts with the Lake Boudreaux fault, to the end of the IdJC1 segment. Contour spacing decreases eastward towards the area of maximum contour. This is supported by a corresponding increase in contour values from 200 m to 760 m at the center of closed elliptical-shaped contour. From this structural high to the east tip of the IdJC1, the contour values decreased by approximately 160 m. The second structural high area is characterized by much more closely spaced contours compared to the first structural high.

40

The contour value increase from west to east and from top to approximately 1000 m at the center of the semi-closed contour. The third structural high area, located close to Bully camp stock, show similarity in contour spacing and value to the second structural high.

Temporally, the contour spacing increases up-dip, whereas contour values decrease up-dip towards the Miocene-Pliocene boundary. The middle portion of the map shows a further increase in contour spacing compared to contour spacing towards the end of the Miocene. However, at the top of the map, there is a relative decrease in contour spacing and the shape of the contours is sub-horizontal.

2.4.3.3 Lake Boudreaux Fault

2.4.3.3.1 Throw vs. Distance plot

The throw vs. distance plot for the Lake Boudreaux fault (Fig. 2.14) is asymmetrical and throw decreases rapidly at the southeast portion of the fault compared to gradual decrease at the northeast portion. Unlike the IdJC fault, the throw maximum is close to the fault center, i.e., at approximately 13 km. In comparison to the IdJC fault, there are points of abrupt increase and decrease in fault throw. These points correlate with where east-west striking faults intersect the Lake Boudreaux fault, and the magnitude of increase or decrease depends on the throw of the interacting fault. If the interacting fault is on the footwall of the LB, the throw decreases. For example, where IdJC interacts with Lake Boudreaux fault. Whereas if the interacting fault is on the hanging wall of the LB, the throw increases. For example, throw increases where Dulac fault interacts with Lake Boudreaux.

41
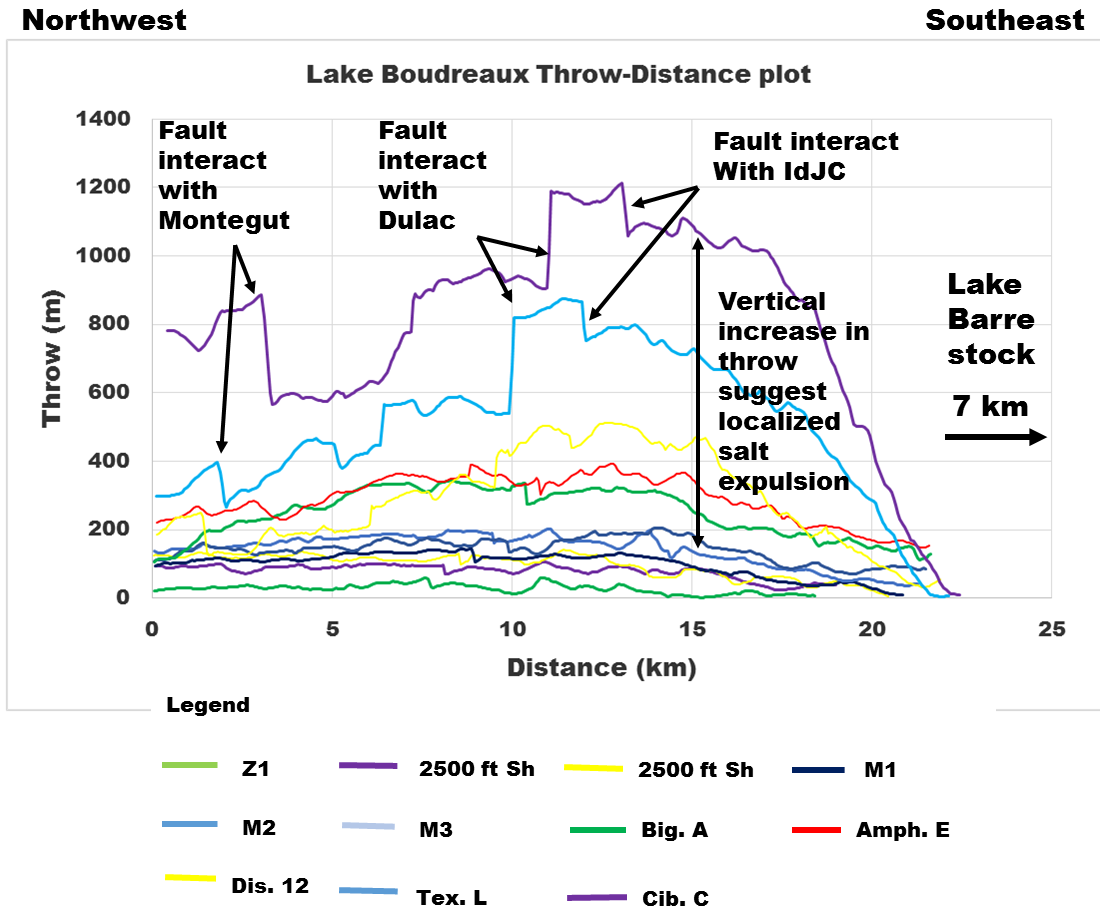
Figure 2.14. A plot of throw aginst Distance (T-x) for Lake Boudreaux fault. An abrupt increase/decrease in throw occurs where the fault interacts with Isle de Jean Charles, Montegut, and other east-west striking faults. The throw decrease if the interacting fault is on LB hanging wall whereas throw increase if the interacting fault is on the footwall of LB. The gradient of the displacement profile is steeper between 10 and 23 km compare to between 0 and 10 km.

In addition to the abrupt lateral change in throw, there is also a rapid decrease in throw from the oldest to the youngest reflector. The rapid throw change is faster for the three oldest reflectors. The maximum throw for the *Cib. C*, *Tex. L*, *Dis. 12* and *Amph. E* is 1200 m, 862 m, 513 m, and 392 m respectively, and the calculated throw decrease

between *Cib. C* and *Tex. L* is 338 m, *Tex. L* and *Dis. 12* is 349 m, and *Dis. 12* and *Amph. E.* is 121 m.

The throw profile began to flatten by the deposition of *Amp. E,* between 5 km and 16 km. In comparison to the older strata, the decrease in throw is smaller; throw decrease by 48 m between *Amph. E* and *Big A*. However, the decrease in throw between *Big. A* and M3 was much higher with a calculated decrease of 138 m. By the beginning of M3, the decrease in throw had dropped drastically and ranged from 3 m to 57 m. However, between Quaternary 2500 ft shale and Z1, the decrease in throw had increased to 47 m.

2.4.3.3.2 Throw map

The throw map of the Lake Boudreaux fault suggests variation in fault activity along strike and depth (Fig. 2.15). This variation is interpreted based on varying contours patterns and distribution. The lower portion of the map shows two areas of high elliptical contour values separated by a region of relatively low contours value with sub-horizontal to horizontal contour pattern. The first structural high area is at the northwest portion of the fault. The contour pattern of the first structural high changes from sub-horizontal to elliptical at its center with the center having a contour value above 880 m. Southeast of this structural high, the contours abruptly changes to sub-vertical. The second structural high is located southeast of the first and extends over a much wider area. Its contour value increase from the northwest towards the center with a maximum contour value of 1200 m. At two different points, the contour pattern abruptly changes from sub-horizontal to sub-vertical. Beyond these points, the contour pattern gradually changes from sub-

horizontal to sub-vertical, and contour value also decreases to the southeast from 1200 m

to less than 200 m.
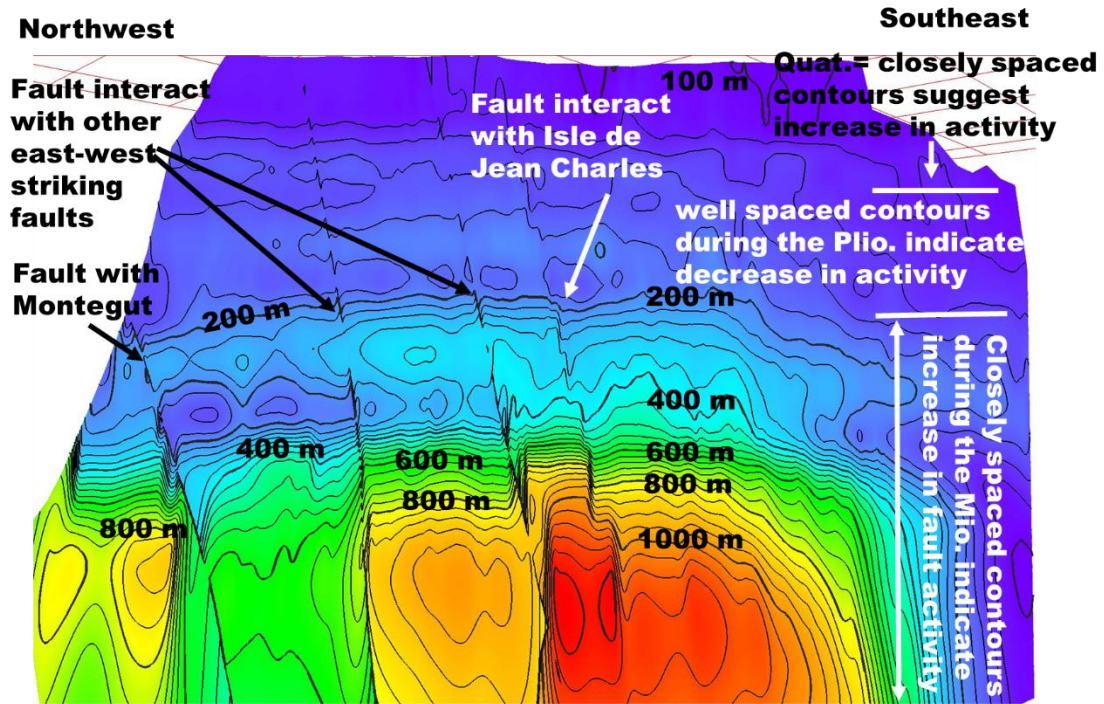
Figure 2.15. Throw map for Lake Boudreaux fault. Horizontal to sub-horizontal contours indicate an interval of active fault growth. Closely spaced contours between 200 m and 1000 m suggest high fault activity whereas well-spaced contours between 180 m and 200 m indicate a decrease in fault activity. The rapid change in contour value and pattern at the base of the base is due to an increase/decrease in throw due to interacting of east-west striking faults. C.I. = 40 m and V.E. is 10

Temporally, the contour spacing increases up-dip from the bottom of the map

towards its center, whereas its values decrease from over 1000 m to 200 m at the

Miocene-Pliocene boundary.Contours between the 400 m and 200 m contours are widely

spaced compared to contours at the bottom of the map. The three contours that are closer

to 200 m contour are more closely spaced and more sub-horizontal compared to contours that are closer to the 400 m. Up dip of the 200 m contour, there is an increase in contour spacing with a corresponding decrease in contour value. However, by the beginning of the Quaternary, the uppermost portion of the map, there is a decrease in contour spacing.

2.5. Discussion

2.5.1 Late Miocene to Pleistocene fault activity

Kinematic analyses of faults in the Lapeyrouse-Chauvin vicinity suggest two stages of fault growth; a Late Miocene stage and a Quaternary stage (Fig. 2.8 and 2.9). The Late Miocene stage started before the deposition of SU 1 as suggested by high E.I., high throw, large difference in strata thickness across the large faults, and closely spaced contours at the bottom of throw maps (Figs. 2.11, 2.13 and 2.15). However, the high fault activity began to decline by SU 3 (Fig. 2.9), as indicated by a decrease in E.I., throw, and an increase in contour spacing towards the end of Late Miocene. Fault activity was rapid during the deposition of the Miocene strata because sediment delivery to the basin was high as the study area lies within the Miocene depocenter (Galloway, 2001; Galloway et al., 2011) of the ancestral Mississippi River and Tennessee River (Galloway et al., 2011). The high sediment flux and depositional loading led to rapid salt evacuation and accelerated fault activity.

Evidence of a positive correlation between fault activity and salt evacuation is interpreted from the increase in fault throw (Fig. 2.12 and 2.14) and strata thickness (Fig. 2.7) along the Isle de Jean Charles and Lake Boudreaux fault towards the Bully Camp and Lake Barre salt stock, respectively. The decrease in fault activity at the end of the

45

Miocene is interpreted as a decrease in sediment loading to the northern Gulf of Mexico caused by uplift and decrease in precipitation in the hinterland (Galloway et al., 2011).

The Miocene stage is separated from the Quaternary stage by SU 6 to SU 8: a period of a relative decrease in fault activity (Fig. 2.8 and 2.9) indicated by (1) widely spaced contours at the middle portion of the throw maps (Fig. 2.11, 2.13 and 2.15), (2) low E.I., and (3) low gradient on the T-z plot between subsea depth of 2000 m to approximately 800 m. This depth interval corresponds to M3 to M1 (Fig. 2.5 and 2.6). Based on the slow fault activity, I interpret that SU 6 to SU 8 are Pliocene strata because the Pliocene depocenter is located south of the TSWB and Louisiana's coastline (Galloway, 2001). Therefore, the period of reduced Pliocene sediment deposition and storage in the study area led to decreased fault activity.

The Quaternary stage, SU 9 to SU 10 shows evidence of rejuvenation of activity based on the decrease in contour spacing at the top of the throw maps, increase gradient on T-z plot between subsea depth of 800 m and 500 m, high E.I., and increase in strata thickness across the large faults. An abrupt increase in fault activity in this stratal section in the study area is interpreted to be because it falls within the Pleistocene *Trimosina A, Sangamonian* (Galloway, 2001), MIS 4, MIS 3 and MIS 2 depocenters (Coleman and Roberts, 1988b) and the late Holocene age Mississippi River LaFourche and Teche delta lobes (Coleman et al., 1998; Roberts, 1997).

The throw rates for the large faults are calculated by plotting each horizon's biostratigraphic ages against its corresponding throw (Fig. 2.16 and Table 2.1). The long-term (Mio. – Mid. Pleistocene) average rates for the three large faults are 0.0896 mm/yr for the southeast segment of the Lake Boudreaux fault, 0.0651 mm/yr for the northwest

segment of the Lake Boudreaux fault, 0.0296 mm/yr for the Isle de Jean Charles fault, and 0.0131 mm/yr for the Montegut fault. The rates of the faster Lake Boudreaux and Isle de Jean Charles faults fall within the calculated rate by Nicol et al. (1997) of 0.03 – 0.4 mm/yr for faults in the Gulf Coast.

This present study faults rate also lie within the range of other gravity-driven faults such as 0.09 – 0.12 mm/yr for the Niger Delta (Pochat et al., 2009), 0.02 – 0.18 mm/yr for Angola (Dutton and Trudgill, 2009), and 0.03 – 0.18 mm/yr for Norway (Jackson, 2017). In comparison to tectonic faults, the Lapeyrouse area faults are moving at similar rates as the North Sea; 0.005 – 0.15 mm/yr (Nicol et al., 1997), Timor Sea; 0.005 – 0.067 mm/yr (Nicol et al., 1997), and Basin and Range; 0.02 – 0.7 mm/yr (Mouslopoulou et al., 2009; Nicol et al., 1997) whereas they are slower than faults in the Corinth Rift and Apennines, both with a minimum rate of 0.22 mm/yr and 0.17 mm/yr, respectively (Mouslopoulou et al., 2009).

The short-term throw rate was calculated using the age for the base of SU 9, i.e., the Middle Pleistocene shale with an index fossil *Angulogerina B* with a calculated age of 1.54 Ma to present data surface. These rates are 0.65 mm/yr and 0.62 mm/yr for the southern and northern segments of the Lake Boudreaux fault, respectively; the Isle de Jean Charles and Montegut faults are slipping at 0.54 mm/yr and 0.53 mm/yr, respectively, averaged over this short and more recent timescale. These rates are almost an order of magnitude higher than the Baton Rouge fault, with a latest Pleistocene rate of 0.07 mm/yr (Shen et al., 2016).
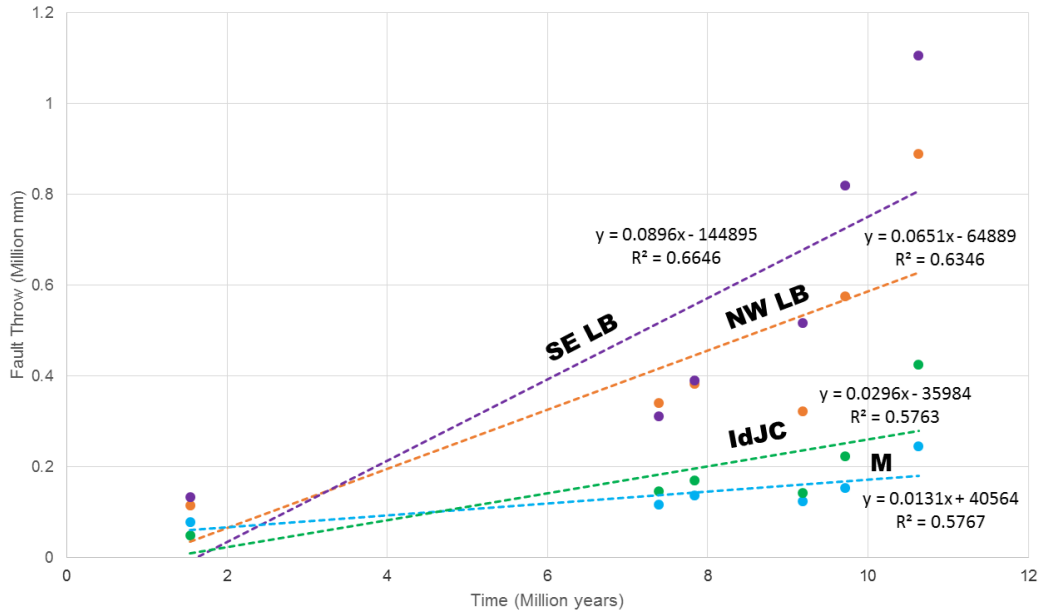
Figure 2.16. A plot of Throw against biostratigraphic age.

Table 2.1. Long term and short term throw rate for the Montegut, Isle de Jean Charles and Lake Boudreaux fault

	Long term rate, Mid. Miocene-present (mm/yr)	Approx. Pleistocene rate (mm/yr)
SE Lake Boudreaux f.	0.0896	0.648
NW Lake Boudreaux f.	0.0651	0.621
Isle de Jean Charles f.	0.0296	0.542
Montegut f.	0.0131	0.531

2.5.2 Holocene and Modern fault activity

Though this present study could not interpret faults at the top of the seismic

volume due to poor resolution (Fig. 2.5 and 2.6) and did not compute the throw beyond

the middle Pleistocene, 0 to 500 m subsea (Fig. 2.8), some studies show faults in

southeastern Louisiana were active during the late Holocene and in the modern time.

These studies suggest that the displacement of the Montegut, Lake Boudreaux, and Isle

de Jean Charles faults does not decrease to zero.

In the Lapeyrouse study area, analyses of sediment cores on both sides of the

southeast portion of the Lake Boudreaux fault show that, within the last 850 years, there

is evidence of thickening across the fault and with a measured throw of 0.57 m (Yeager

and Whitehead, 2020). The Late Holocene throw rate of 0.67 mm/yr (Yeager and

Whitehead, 2020) is similar to the present study's short-term throw rate of 0.65 mm/yr.

Along the Baton Rouge fault zone, activity is interpreted during the late Holocene

(Shen et al., 2016). According to Shen et al. (2016), the Baton Rouge fault's Late

Holocene throw rate is 0.22 mm/yr.

Faulting of Holocene strata is observed in southeastern Louisiana due to rising

salt structures (Heinrich et al., 2015). Some of the salt structures in this region affect the

Holocene-Pleistocene boundary through continuous salt deformation during Holocene

sediment deposition, outcrop on the surface or subsurface deformation that influence the

structure of younger strata (Heinrich et al., 2015).

Geology and geomorphic evidence in the Montegut fault area also suggest

modern activity. Cross-section across the Montegut fault using sediment cores indicate

thickening of the upper grassy peat layer increases from 0.75 m on the footwall to over

49

1.25 m on the hanging wall (Gagliano et al., 2003a). Further, the difference in elevation between the marsh floor on the upthrown block and the lake's bottom on the downthrow block is 0.8 m (Gagliano et al., 2003a).

A recent elevation study along bridges over Lake Pontchartrain by Hopkins et al. (2018) shows that the Baton Rouge Fault zone is still active. On one of the bridges built approximately 90 years ago, the difference in elevation between the hanging wall and footwall cutoffs is 0.26 m. The throw rate for the fault is between 1.5 – 2.8 mm/yr (Hopkins et al., 2018).

2.5.3 The role of faults in coastal wetlands loss and subsidence

While the fault traces in the study area cannot be observed directly at the top of the seismic volume, extrapolation of the fault planes to the surface shows a close correlation between surface projections of these faults with boundaries between marsh or swamp and open water (Fig. 2.2). The Montegut fault forms a boundary between a cypress swamp on the footwall and a lake on the hanging wall. For the Isle de Jean Charles fault, there is no apparent correlation between fault and open water bodies because both sides of the fault have lost a significant amount of marsh and surface fault traces are underwater.For the Lake Boudreaux fault, there is a correlation between the marsh-water break at the location where the Isle de Jean Charles fault merges into it. Northwest of this interaction, the marsh edge roughly parallels the fault trace but lies northeast of it, suggesting that the marsh edge may have retreated. The difference between the location of marsh edge and Lake Boudreaux fault trace may be due to marsh erosion.

Marsh edge retreat is controlled by both subsidence and erosion by wave action. In the Barataria Bay and Breton Sound, the amount of wetland loss due to wave erosion is 63% and 72%, respectively (Wilson and Allison, 2008). In the Madison Bay area, subsidence is the primary cause of wetland loss (Wilson and Allison, 2008).

Gagliano et al. (2003b) establish a relationship between fault activity and hydrology in the Terrebonne area. By comparing aerial photographs of different years and superimposing fault trace on them, the authors show that the opening of Lake Boudreaux and the wetland loss in Montegut are related to fault movement. According to Gagliano et al. (2003a), the Lake Boudreaux fault is at the lake's west shoreline. However, the result of this present study indicate that the fault is very close to the east shoreline. In contrast, the inferred location of the Montegut fault, based on the sharp boundary between dead cypress trees and broken marsh or water (Gagliano et al., 2003a) is coincident with the surface extrapolation of the fault trace from this study's interpretation of 3D seismic.

Yeager et al. (2012) examine fault activity along the Pearl River, Louisiana, located 140 km northeast of the Lapeyrouse study area and east of Lake Pontchartrain, and found evidence of active faults based on sediment thickening across faults, as well as surficial evidence in the form of variable marsh species, and change in fluvial drainage patterns across the trace. Ponded rivers and straight river channels along the Pearl River suggest active faults. Interpretation of shallow seismic profiles acquire along rivers shows discordant reflectors, which confirms shallow faults. Furthermore, marsh species change across the fault trace with *Panicum virgatum,* a freshwater species, and *Phragmites australis,* a saltwater species, dominating the footwall and hanging wall, respectively.

51

Compared to the Lapeyrouse area, the cypress forest dominates the Montegut fault footwall, whereas open water predominates along the hanging wall side. Furthermore, Bayou Pointe Aue Chene and Bayou Isle de Jean Charles are both discontinuous i.e., they do not extend to the Gulf Coast shoreline, suggesting the influence of fault-induced subsidence.

The present study's results on recent fault activity are similar to O' Leary and Gottardi's (2020) results in the Chenier Plain in Cameron Parish, southwest Louisiana, despite the difference in late Holocene stratigraphy. Wave action reshaping sediment transported westward of the active Mississippi-Atchafalaya outlet forms the Chenier Plain (O'Leary and Gottardi, 2020). Here, the Holocene is much shallower (~10 m below the surface; O'Leary and Gottardi, 2020). In contrast, the Holocene sediment is at least 76 m thick (Heinrich et al., 2015) within the Terrebonne Salt Withdrawal basin. The greater Holocene thickness in the basin is due to the Mississippi River deposition of the late Holocene Teche (~5500 – 3800 yrs BP) and the LaFourche (~2500 – 800 yrs BP) delta complexes (Coleman et al., 1998; Roberts, 1997).

By projecting faults to the surface and comparing historic aerial photographs for 1953 and 2017, O'Leary and Gottardi (2020) show the appearance of open water bodies on the downthrown side of fault traces, whereas coastal marsh remains on the upthrown blocks. The elevation difference across the faults in the Chenier Plan area is about 0.46 m. Similarly, surface extrapolation of faults in the Layperouse study i.e., the Montegut, Lake Boudreaux, Isle de Jean Charles, and radial faults from the Bully Camp stock show these faults' footwall define the boundary of lakes on the hanging wall.

The present study's results differ from those of Kuecher et al. (2001) carried out around the Terrebonne and Lafourche Parishes, Louisiana in that the structural framework of the Lapeyrouse-Chauvin area is more complex, comprising large faults, a graben, and radial faults from the Bully Camp salt stock (Fig. 2.17). Using widely spaced 2D seismic profiles and well logs, Kuecher et al. (2001) define three east-west striking faults, the Lake Hatch, the Spur, and the Golden Meadow. The fault trace of the latter extends westward beyond the eastern shoreline of Lake Boudreaux. However, the present results show that the Isle de Jean Charles segment of the Golden Meadow fault intersects the northwest striking Lake Boudreaux fault at Lake Boudreaux's eastern shoreline (Fig. 2.17). The intersection of the surface projection of both faults is located west of both Highway 56 and the junction of Bayou Petit Caillou and the Bush Canal (Fig. 2.2).

Secondly, Kuecher et al.'s (2001)suggest that low conductivity across the Golden Meadow fault trace based on electromagnetic surveys along Bayou du Large and Bayou Grand Caillou indicates that the fault is not active. However, based on 3D mapping, this study would suggest that there is no difference in conductivity because the surface projection of the Golden Meadow fault lies about 8 km east of Bayou Grand Caillou rather than where it was studied by Kuecher et al. (2001).

Leveling data along Highway 56 within the Madison Bay area shows an abrupt increase in subsidence across the Isle de Jean Charles fault (Morton and Bernier, 2010; Morton et al., 2006; Morton et al., 2005; Morton et al., 2002). Surface elevation measured between 1966 to 1993 increased across the fault, from 105 mm on the footwall to 250 mm on the hanging wall (Morton et al., 2002). The impact of fluid withdrawal, i.e., hydrocarbon withdrawal on subsidence, has been examined in the Bay Madison area

(Morton and Bernier, 2010; Morton et al., 2006; Morton et al., 2005; Morton et al., 2002). By comparing hydrocarbon production data with subsidence data, these authors argue that fluid withdrawal drives subsidence in the area. In contrast, this study's results suggest that fault-induced subsidence drive subsidence in the area. For example, the Isle de Jean Charles town and Pointe Aux Chene Marina are on the more active portion of the Isle de Jean Charles, i.e., the east tip of IdJC1 and IdJC2, respectively that are strongly influenced by salt expulsion into the Bully camp salt stock. The surface projection of IdJC2 shows marsh on the footwall and water on the hanging wall suggest that the Isle de Jean Charles fault is still active.
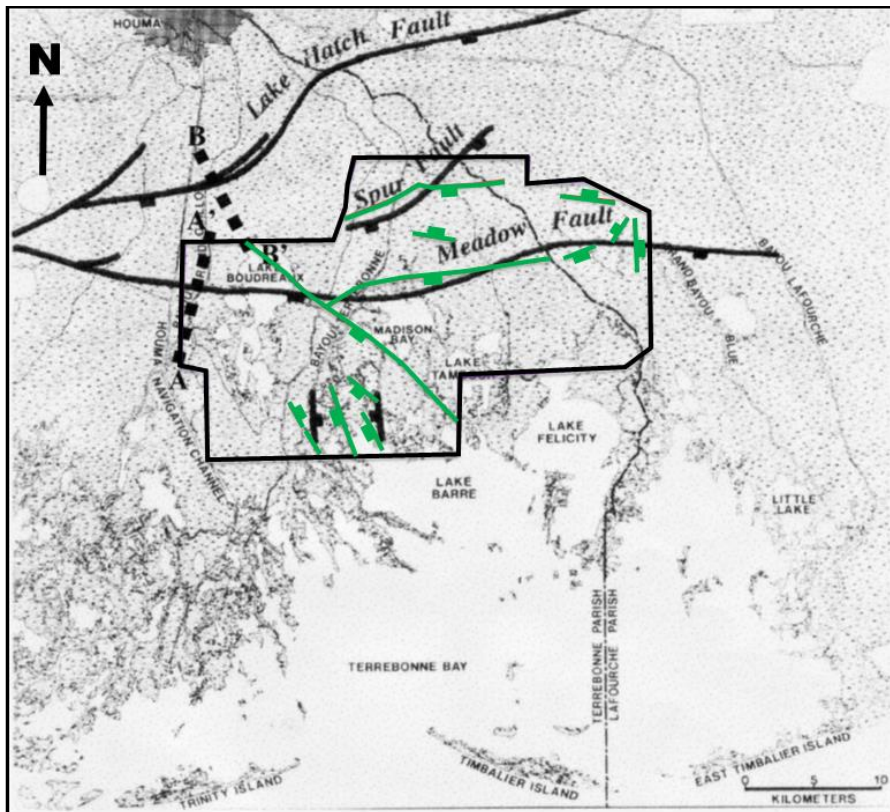
Figure 2.17. Fault trace based on 3D interpretation of the Lapeyrouse-Chauvin data (Green) superimposed on the fault trace of Kuecher et al. (2001) (Black). Modified after Kuecher et al. (2001)

Modeling of compaction-induced subsidence by Chan and Zoback (2007) shows that this compaction accounts for 1/3 of the observed subsidence along the Isle de Jean Charles fault. However, the authors used Kuecher et al. (2001) fault trace of the Golden Meadow fault that was generated using sparsely space well data and 2d seismic profiles. My result shows that the interaction of the Isle de Jean Charles, Lake Boudreaux, and Dulac faults produced a double drop-down geometry (Fig. 2.7 and 2.18) that accounts for high fault-induced subsidence during the Neogene.
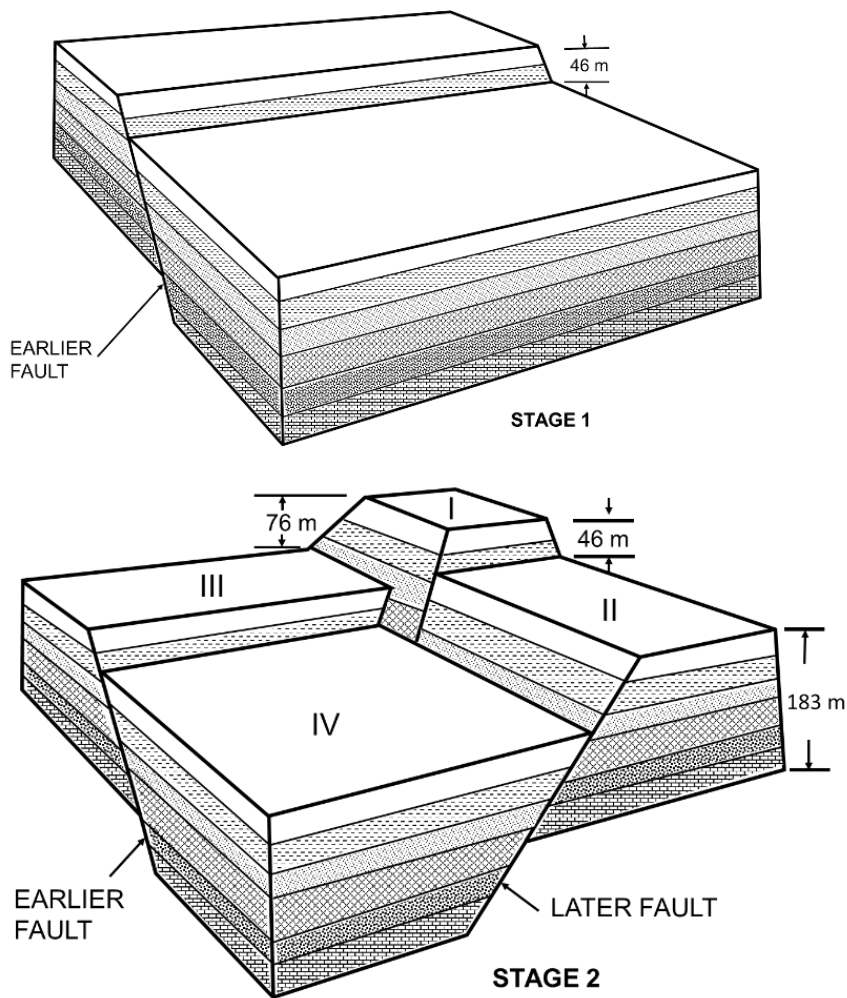
Figure 2.18. Double drop-down geometry formed by intersecting faults. Modified after Dickinson (1954)

Far-field events such as earthquakes also influence fault activity in southeastern Louisiana. Gagliano et al. (2003b) correlate the 1964 rapid change in tides reading from gauges on the Frenier Fault zone, Lake Hatch Fault zone, Golden Meadow Fault zone, and Leeville fault zone to movement induced by the magnitude 8.3 Prince William Sound earthquake in Alaska. According to this study, there was oscillation in closed water in New Orleans, Venice, and Balize Delta, with boats slamming against the landing stage. The water movement suggests that the earthquake was felt in Louisiana and might have led to movement along these pre-existing faults. Activity on these faults within the Terrebonne Salt Withdrawal basin indicates that these remain active faults in the present day.

Frederick et al. (2019) examine the contribution of deep geology processes on the subsidence rate in southeastern Lousiana. Using a fault throw of 6.71 m for a 0.58 Ma sequence, the authors argued that fault-induced subsidence accounts for approximately 4.5 % of the observed subsidence. However, the data used for this calculation are from 1^0 north of the Golden Meadow area, a region with relatively thin sediment deposition and slower fault activity. My result shows an increase in fault activity during the deposition of SU9 and SU10. The maximum fault throw on the youngest Z1 horizon's surface is between 49 m – 59 m. On a short-term scale, the throw rate of the three faults in the Lapeyrouse area is one order of magnitude higher than the Baton Rouge Fault zone. This rate shows that faults within the TSWB are faster and contribute more to subsidence compare to faults in the Baton Rouge Fault zone.

2.6. Conclusions

The kinematic analyses of faults in the Lapeyrouse-Chauvin area, southeastern Louisiana using 3-D seismic data and well logs shows that;

a) Three large faults, Montegut, Isle de Jean Charles, and Lake Boudreaux faults, minor faults, and radial faults define the subsurface structure of the area.

b) Isle de Jean Charles and Lake Boudreaux are more active than the Montegut fault. Displacement on both faults increases along strike towards adjacent salt stocks.

c) Activity on these faults is divided into two stages; the Miocene and the Quaternary stage. The Miocene stage is characterized by high fault activity and rapid salt evacuation due to high sediment influx. The stage is followed by a period of low fault activity during the Pliocene. This is because the Pliocene depocenter is located south of the study area. The location of the Quaternary depocenter within the TSWB led to the rejuvenation of fault activity and salt expulsion.

d) The surface location of faults coincides with areas of on-going wetland loss and subsidence, suggesting fault activity into the modern. The region with the highest subsidence, Bay Madison, and the area around the town of Isle de Jean Charles experienced high subsidence and rapid fault activity from the Miocene to the Quaternary due to their proximity to these salt structures.

Chapter 3

Spatial and Temporal Throw Variation in the Terrebonne Salt Withdrawal Basin: Effects of sediment loading and diapiric stress perturbation

Abstract

Fault throw distribution is influenced by a variety of mechanisms that range from the interaction of faults with one another to salt-fault interaction. Throw patterns after interaction and linkage are strongly controlled by the genetic relationship of the fault segments. However, the presence of salt influences the throw distribution, and it remains unclear the extent of salt influence on the spatial and temporal throw pattern of faults. In the Terrebonne Salt Withdrawal Basin in the Gulf of Mexico, I used throw profiles, throw maps of fault planes, sedimentary growth indices and throw-distance plots to examine each of the two faults, the Lake Boudreaux fault and the Isle de Jean Charles fault. Both faults have a tip located very near a salt stock, Lake Barre and Bully Camp salt pillars, respectively. Both faults show similar temporal throw history that is expected because both lie within the Golden Meadow fault zone. However, their spatial throw distribution is different. Throw on the Lake Boudreaux fault is strongly influenced by intersecting east-west striking faults, whereas throw pattern of the segmented Isle de Jean Charles fault shows that Isle de Jean Charles initiated as a kinematically coherent fault segments. Both faults differ in the way they interact with adjacent salt stocks. The interaction of the Isle de Jean Charles fault with the Bully Camp salt stock increased fault throw towards

the stock, whereas the Lake Barre stock absorbed strain, inhibiting the propagation of the Lake Boudreaux fault towards it.

3.1 Introduction

Fault throw distribution and rate are useful in interpreting the timing of salt evacuation, sediment loading, and fault activity (e.g., Alexander and Flemings, 1995; Dutton and Trudgill, 2009; Jackson, 2017). Many studies have shown how fault throw pattern are influenced by fault interaction (Cowie and Roberts, 2001; Gupta and Scholz, 2000; Maerten et al., 1999; Peacock and Sanderson, 1991; Willemse et al., 1996), fault linkage (Childs et al., 1995; Dawers and Anders, 1995; Mansfield and Cartwright, 1996; Walsh et al., 1999; Young et al., 2001) and interaction with salt structure (Rowan et al., 1999; Tvedt et al., 2016; Tvedt et al., 2013; Vendeville and Jackson, 1992b). Studies have also examined the different growth stages of a salt stock in terms of relationship with radial faults (Vendeville and Jackson, 1992a, b), however, it remains unclear how the diapiric stress of a rising diapir influences the displacement pattern of large faults that interacts with stocks.

The presence of salt structures in a basin affects the displacement distribution on a fault array (e.g., Child et al., 1995). In the absence of salt, the maximum displacement is located in the middle of a fault or a fault array (Peacock and Sanderson, 1991; Willemse et al., 1996). When salt is present and the fault interacts with a salt structure, the maximum displacement is located close to the salt-fault interface (e.g., Child et al., 1995; Tvedt et al., 2016).

Near the salt-fault contact, salt can either increase the throw on a fault or "absorb" the shear strain that would be roughly equivalent to the fault displacement. If the "strain absorption" is being accommodated by ongoing flow of salt into a diapir, then changes in the diameter of the salt structure may show a relationship to the temporal and spatial pattern of faulting around the diapir (Vendeville and Jackson, 1992b).

The strain around the salt stock is caused by circumferential stress or hoop stress. Numerical modeling of stresses around salt stock shows that the hoop stress is the minimum principal stress (Heidari et al., 2017; Nikolinakou et al., 2014). This stress is generated by diapiric force on the surrounding sediment (Heidari et al., 2017). The rock strata release the pressure through the formation of radial faults (Heidari et al., 2017; Nikolinakou et al., 2014) or accommodate it through ductile stretching (Stewart, 2006). Active deposition around a passive diapir, i.e., a diapir at the surface, can subdue the stress in newly deposited sediment (Maltman, 1994; Stewart, 2006).

Hoop stress around the North and South Pierce salt stocks in the North Sea influences the displacement pattern of polygonal faults (Carruthers et al., 2013). The faults within the lateral extent of the stress were rotated and aligned radially to the stocks. Although realigned, these faults maintain their dumb-bell displacement profile compared to an asymmetrical profile of radial faults that propagate from both stocks. Outside the limit of the hoop stress, the polygonal faults appear undisturbed by the stress field. The polygonal faults are relatively small in size, between 0.15 – 1 km in length (Carruthers et al., 2013), as compared to large faults with lengths in 10s and 100s km (Mouslopoulou et al., 2009). Due to the scale of large faults, the salt-induced stress may or may not have a similar effect on large faults. Therefore, this chapter examines the extent and effect of

stress perturbation on the displacement pattern of large faults as it interacts with a salt stock.

This study investigates the influence of salt tectonics and mechanisms of fault formation on spatial and temporal throw distributions of the Isle de Jean Charles and Lake Boudreaux faults, located in the Terrebonne Salt Withdrawal Basin, Gulf of Mexico (Fig. 3.1). The area provides an excellent opportunity for studies of fault-salt interaction because of abundant well logs, 3D seismic data, and previous mapping of salt structures (Abriel and Haworth, 2011; Frey and Grimes, 1970). Furthermore, the study area lies within the region of several key early studies of salt evacuation along the northern Gulf of Mexico (GOM) margin (McBride, 1998; Peel et al., 1995; Schuster, 1995). My results show that the growth pattern of a salt structure and the diapiric stress affects the location of throw maximum, dictates whether a fault eventually intersects the structure, and connects multiple salt structures.

3.2 Geological Setting

The rifting of the supercontinent Pangea, during the middle Mesozoic led to the formation of the Gulf of Mexico basin (Buffler and Sawyer, 1985; Hudec et al., 2013). Initially, the basin was a small, restricted and very saline basin, resulting in the precipitation of the Jurassic Louann salt (Buffler and Sawyer, 1985). With continuing development of the GOM and Atlantic ocean basins, salt precipitation ceased (Hudec et al., 2013). During the Late Jurassic, rifting slowed and the formation of oceanic crust and thermal subsidence became the dominant processes (Buffler and Sawyer, 1985; Hudec et al., 2013).

61
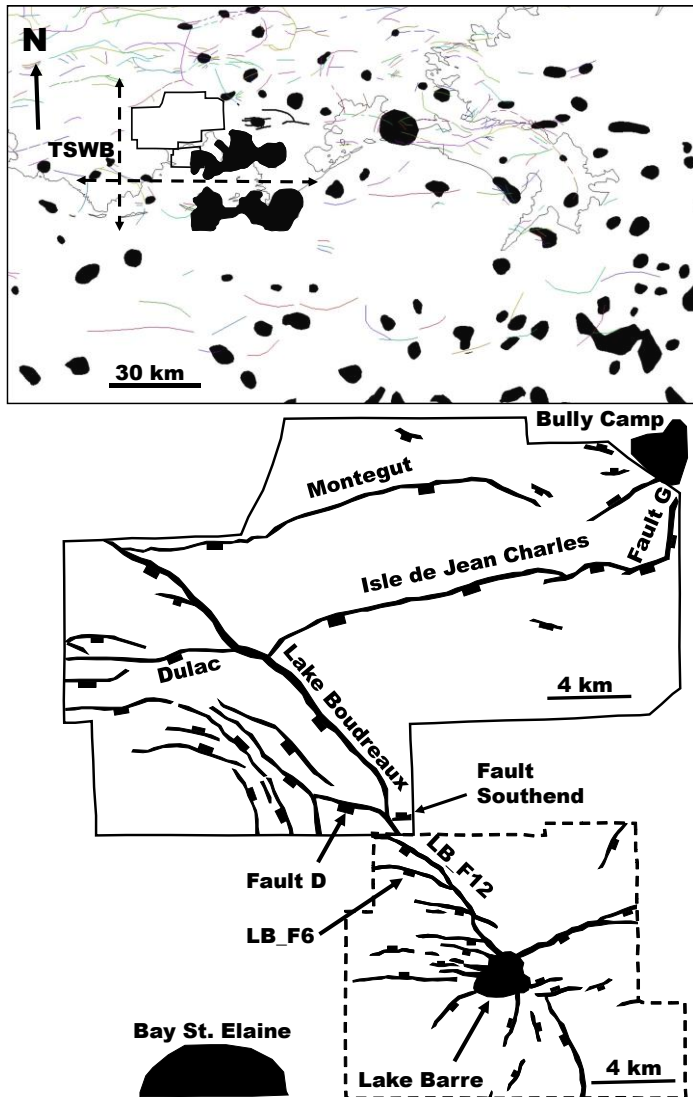
Figure 3.1. (Upper) Map of the northern Gulf of Mexico (GoM) showing the Terrebonne Salt Withdrawal Basin (TSWB). The lateral extent of the basin extends across southern Louisiana (broken arrows). The Caillou Island-Bay Marchand salt ridge (Black elongated polygon) defines the southern margin of the TSWB. Data for the salt ridge is from Abriel and Haworth (2011). Data for the other salt structures (black polygon) is obtained from Seismic Exchange Inc (SEI). Linear to curvilinear lines are regional faults compiled by Elizabeth McDade for Louisiana Coastal Atlas. (Lower) Fault map of the Lapeyrouse-Chavin and Lake Barre area. The fault trace is based on the structure map of the *Amphistegina E*. The map shows Isle de Jean Charles (IdJC), Dulac, Lake Boudreaux, Fault D, Fault G, LB_F12, and LB_F6. Both IdJC and Lake Boudreaux interact with radial faults from the Bully Camp and Lake Barre salt stock, respectively. The graben on Lake Boudreaux hanging wall and the east-west striking faults around Lake Barre interact with Bay saint Elaine salt stock. The top survey (closed polygon) is the Lapeyrouse-Chauvin 3D survey donated by Seitel, whereas the bottom survey (broken polygon) is the Terrebonne Bay 3D data donated by Chevron.

The large load of later prograding sediment from the North American continent expelled the salt (Fig. 3.1a). The expelled salt moved basinward and formed an Eocene allochthonous salt canopy covering underlying sediment (McBride, 1998; Peel et al., 1995) and the older rift basins. By the Late Eocene, sediment supplied by the ancestral Mississippi River began to prograde basinward (McBride, 1998; Peel et al., 1995). By the Miocene, there was an increase in activity of existing faults and formation of new faults (McBride, 1998). At the same time, the salt canopy deformed, and salt flow induced by the spatially varying in sedimentary load deposition (Frey and Grimes, 1970; McBride, 1998; Seni, 1992), led to a basinward salt evacuation (Frey and Grimes, 1970; Ingram, 1991; McBride, 1998; Seni, 1992) and the formation of the Miocene-age Terrebonne Salt Withdrawal basin.

The total volume of Louann Salt is greatly reduced in areas underlying present-day southeastern Louisiana, with remaining salt isolated to salt domes. Beneath the current coastline along the Timbalier-Terrebonne-Barataria Bay region, a salt ridge with several stocks developed along the top of it forms the largest salt structure within southeast Louisiana (Abriel and Haworth, 2011; Frey and Grimes, 1970; Ingram, 1991; Rowan et al., 1999). This structure, known as the Bay Marchand-Timbalier Bay-Caillou Island Salt Complex (Frey and Grimes, 1970), along with north-dipping (counter-regional) faults forms the southern margin of the TSWB.The northern margin of the TSWB is defined by the Golden Meadow Fault Zone (GMFZ). Within the basin are salt stocks such as the Bully Camp (Fig. 1a), Clovelly, Golden Meadow, Lake Hermitage, Potash and Cox Bay.

The locus of deposition continued to shift southward during the Neogene, with the Pliocene depocenter lying in the present-day continental shelf (Galloway, 2001). However, during the Quaternary, sediment deposition is concentrated again in the TSWB, especially during Marine Isotope Stage (MIS) 5e (Galloway, 2001), MIS 4, 3, 2 (Coleman and Roberts, 1988b), and also during the Holocene (Coleman and Roberts, 1988b).

3.3 Dataset and Methods

3.3.1 3D seismic and well data

The main dataset for this study are well logs and 3D seismic volume. A well log is a record of change in rock physical attributes such as porosity, permeability, radioactivity, and density, along the wellbore. Logs used primarily for lithology identification such as gamma-ray (GR), resistivity and spontaneous potential (SP) were downloaded from an online public repository, the Strategic Online Natural Resources Information System, or SONRIS which is managed by the Louisiana Department of Natural Resources. The logs, 491 logs in raster format, were loaded into IHS Petra software and well tops with geologic relevance were mapped such as a Mid-Pleistocene 850 m (2700 ft) sand that was mapped by Kolvoord et al. (2008) in the Golden Meadow field (Fig. 3.2), the overlying 760 m (2500 ft) shale and other tops that are laterally continuous. In order to map the equivalent seismic reflectors of the well tops, their depth was loaded into a Kingdom Suite project.

Regional mapping of the study area was done using IHS Kingdom Suite software loaded with a merged 531 sq.km 3-D Lapeyrouse-Chauvin seismic data from Seitel and a

219 sq.km portion of a much larger Terrebonne Bay 3D data from Chevron. Unlike well logs, 3-D seismic data is acquired as a cube. Therefore, it is used to constrain the lateral and temporal variation of rock deformation and depositional patterns. The seismic data have SEG normal polarity with a bin size of approximately 34 m (110 ft) for the Seitel, and 25 m (82.5 ft) for the Chevron survey enables better spatial resolution. The survey inlines depict the geologic structures such as faults and folds better than the crosslines because the inline transverse the geologic structures.

Geologic Age	Stratal Unit	Index Fossil	Reflector mapped	Age (Ma)
Quaternary			Z1	?
	SU 10			
			760 m Shale	?
	SU 9			
		Angulogerina B	850 m Sand	1.54
?—	SU 8			
			M1	?
	SU 7			
Pliocene			M2	?
	SU 6			
?—			M3	?
	SU 5			
		Bigenerina A	Big. A	7.39
	SU 4			
Miocene		Amphistegina E	Amph. E	7.84
	SU 3			
		Discorbis 12	Dis. 12	9.18
	SU 2			
		Textularia L	Tex. L	9.71
	SU 1			
		Cibicides Cartensi	Cib. C	10.63
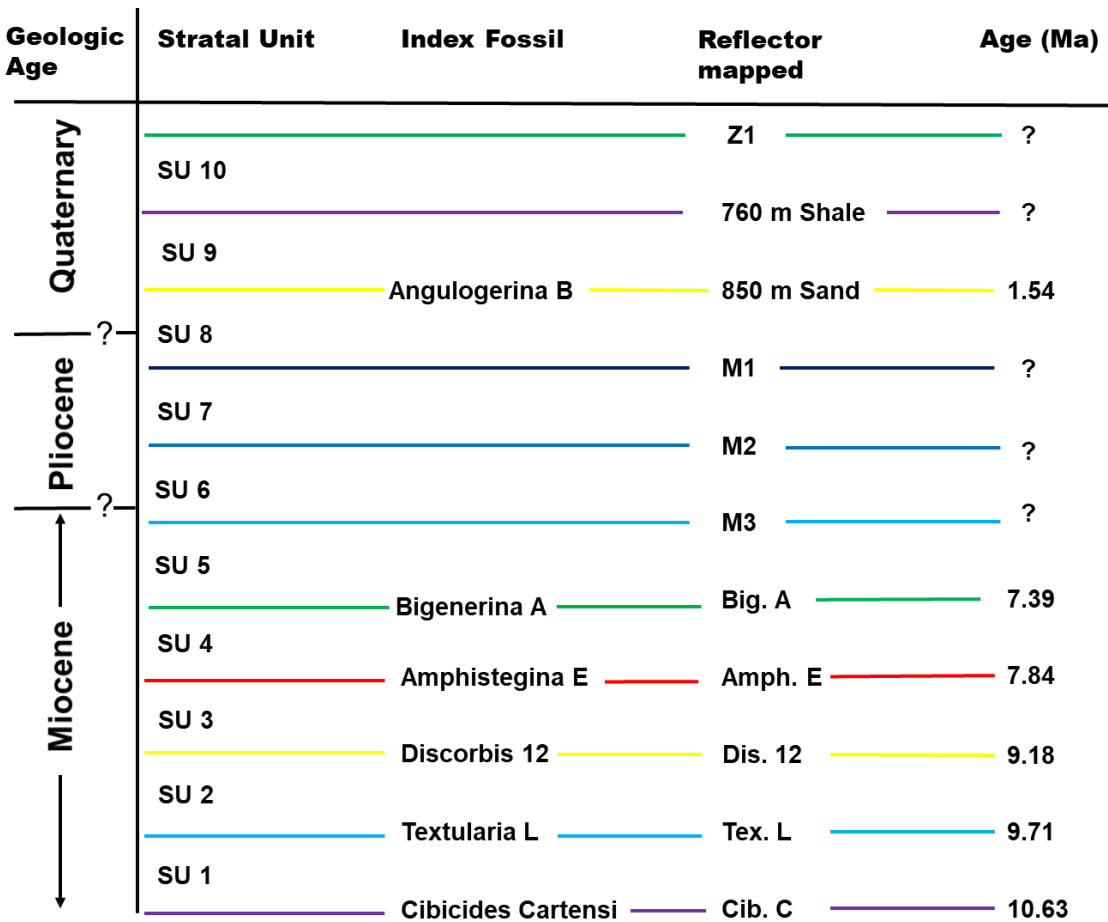
Figure 3.2. Stratigraphic chart showing the ten stratal units (SU) and their respective ages based on biostratigraphic data from PaleoData. *Bigenerina A*, *Ampistegina E*, *Discorbis 12*, *Textularia L* and *Cibicides Cartensi* are constrained by PaleoData, whereas *Angulogerina B* is from Kolvoord et al. (2008)

Data interpretation started with the mapping of faults on every 10 seismic lines using lines that are perpendicular to the fault's strike. Usually, these lines are the inlines; however, some faults were mapped on crossline and arbitrary lines. After faults mapping was completed, 10 stratal unit (SU) defined by the seismic horizon at their top and base were mapped on inlines and crosslines at an interval of 20 lines. These horizon are grouped into three categories (Fig. 3.2); those mapped based on well log correlation such as the Mid-Pleistocene 850 m sand from Kolvoord et al. (2008) and 760 m shale, horizon constrained by biostratigraphy data donated by PaleoData and those mapped based on strong amplitude such as Z1, M1, M2, and M3. The time value of each horizon and the fault traces were used to generate structure maps in two-way travel time (TWTT). Depth conversion of the maps were done by multiplying the time value by time-depth charts from Velocity Databank Inc. The thickness between two successive depth maps was used to generate isopach maps.

3.3.2 Displacement profiles, maps and growth index

Throw measurements obtained from the subsea depth structure maps were used to generate displacement profiles. Fault throw obtained perpendicular to the fault trace was plotted against the mid-point depth of the displaced horizon to generate a throw (T) against depth (z) plot. A T-z plot is use to interpret the phase of fault activity such as the syn-depositional phase expressed as a positive slope (e.g., Cartwright et al., 1998) which is formed as a result of a fault intersecting the free surface (Baudon and Cartwright, 2008a) and a post-depositional phase indicated by a null slope (e.g., Cartwright et al., (1998).

Throw (T) versus distance (x) plot, using Traptester 7 (T7) by Badleys

Geoscience, were generated for each fault. T-x plot is use to interpret fault interaction

(e.g., Peacock and Sanderson 1991; Gupta and Scholz 2000; Walsh et al., 2003), linkage

(e.g., Willemse et al., 1996; Cowie and Roberts, 2001) and interaction with salt structures

(e.g., Tvedt et al., 2016; Coleman et al., 2018) based on shape and gradient of the

displacement profile. To capture the change in gradient and to improve lateral resolution,

we used a sampling interval of 61 m (200 ft). Once the T-x patterns are established, the

displacement of the fault is backstripped using the maximum throw subtraction method

(Dutton and Trudgill, 2009; Jackson et al., 2017; Rowan et al., 1998). This method

sequentially subtracts the maximum displacement of shallow horizons from deeper ones

and is used to interpret the direction of fault propagation and the timing of interaction

(Dutton and Trudgill, 2009).

Fault throws were plotted on the fault plane, using Badley's T7, to generate a

throw map. This map is used to interpret interval of fault activity or growth which is

expressed as horizontal to sub-horizontal contours (Baudon and Cartwright, 2008a;

Childs et al., 2003), post-depositional interval expressed as concentric contours (Baudon

and Cartwright, 2008b) and fault interaction which is expressed as vertical contours (e.g.,

Childs et al., 2003; Baudon and Cartwright, 2008a; Dutton and Trudgill, 2009). Throw

map also helps to interpret salt-fault interaction (e.g., Baudon and Cartwright, 2008;

Tvedt et al., 2013 and Tvedt et al., 2016).

Fault activity can be quantified using strata thickness. The footwall thickness

divided by the hanging wall gives an index; this is referred to as an Expansion Index

(E.I.). Thorsen (1963) was the first person to demonstrate how to use this technique to

interpret the inception, growth phase, and cessation of syn-depositional fault activity. When faulting is post-depositional, the hanging wall and footwall thickness are equal; thus, the E.I. is 1. However, when faulting is contemporaneous with sediment deposition, i.e., syn-depositional, E.I > 1. During this syn-depositional fault, E.I. increase from 1 at the inception of activity to a maximum and then decreases to 1 at the end of the depositional phase (e.g., Thorsen 1963). For the E.I. index to work, the sedimentation rate is assumed to be higher than the fault slip rate (Childs et al., 2003; Jackson et al., 2017; Thorsen, 1963).

3.4. Results

3.4.1 Structural framework

The structure of the Lapeyrouse study area (Figs 3.3a and b) is defined by a complex array of faults. The faults are mostly east-west striking faults of which the Montegut, the Isle de Jean Charles (IdJC), and the Dulac faults are the largest of this fault set. The northwest striking Lake Boudreaux faults are considered together with its graben system. Other faults include a fault at the south edge of the Lapeyrouse survey called the Southend fault and radial faults around Bully Camp and Lake Barre stocks. The Isle de Jean Charles and Lake Boudreaux faults strike towards the Bully Camp stock and Lake Barre stock, respectively. This study focus on these two faults.

The IdJC fault is a basinward dipping fault, and it is 22.6 km long, whereas the Lake Boudreaux fault is 21.6 km in length within the Seitel survey and dips southwest. At shallow depth, both the IdJC (Figs 3.4a, b, and c) and the Lake Boudreaux faults (Fig. 3.4e) appear to intersect the earth's surface as evident by a small offset of seismic

68

reflectors between 0.1 and 0.6 secs. Along its strike, the IdJC fault intersects the Lake

Boudreaux fault at an acute angle of 70^0 forming a T or Y geometry fault (e.g., Maerten

et al., 1999; Fig. 3.3b). Around the intersection point of both faults, the Lake Boudreaux

fault bends towards the northwest. At deeper depth, the structural style of the study area

becomes complicated (Figs. 3.1 and 3.3a). A basinward dipping east-west striking fault,

the Dulac fault (Figs. 3.3a and 3.4d), intersects the Lake Boudreaux fault. This fault,

together with the IdJC and Lake Boudreaux fault, forms a double dropped-down fault

geometry (Figs. 3.1 and 3.3a), which was first defined by Dickinson (1954).

The southwest block of the double dropped-down system is further complicated

by segmentation of the Dulac fault and a northwest striking graben (Figs. 3.1, 3.3a, and

3.3b). The Dulac fault is at least 8.5 km long, and it comprises of three fault segments;

Dulac-north (D-N), Dulac-center (D-C) and Dulac-south (D-S) which offset strata on the

hanging wall of the Lake Boudreaux fault. Dulac-center is the master fault because it

intersects the Lake Boudreaux fault, whereas the Dulac–south physically interacts with

Dulac-center, and Dulac-north is not hard-linked to the master fault. The graben, on the

other hand, is located 3 km west of Lake Boudreaux, and it comprises of at least seven

normal faults. These graben faults strike southwards towards the Bay St. Elaine salt stock

(Fig. 3.1).
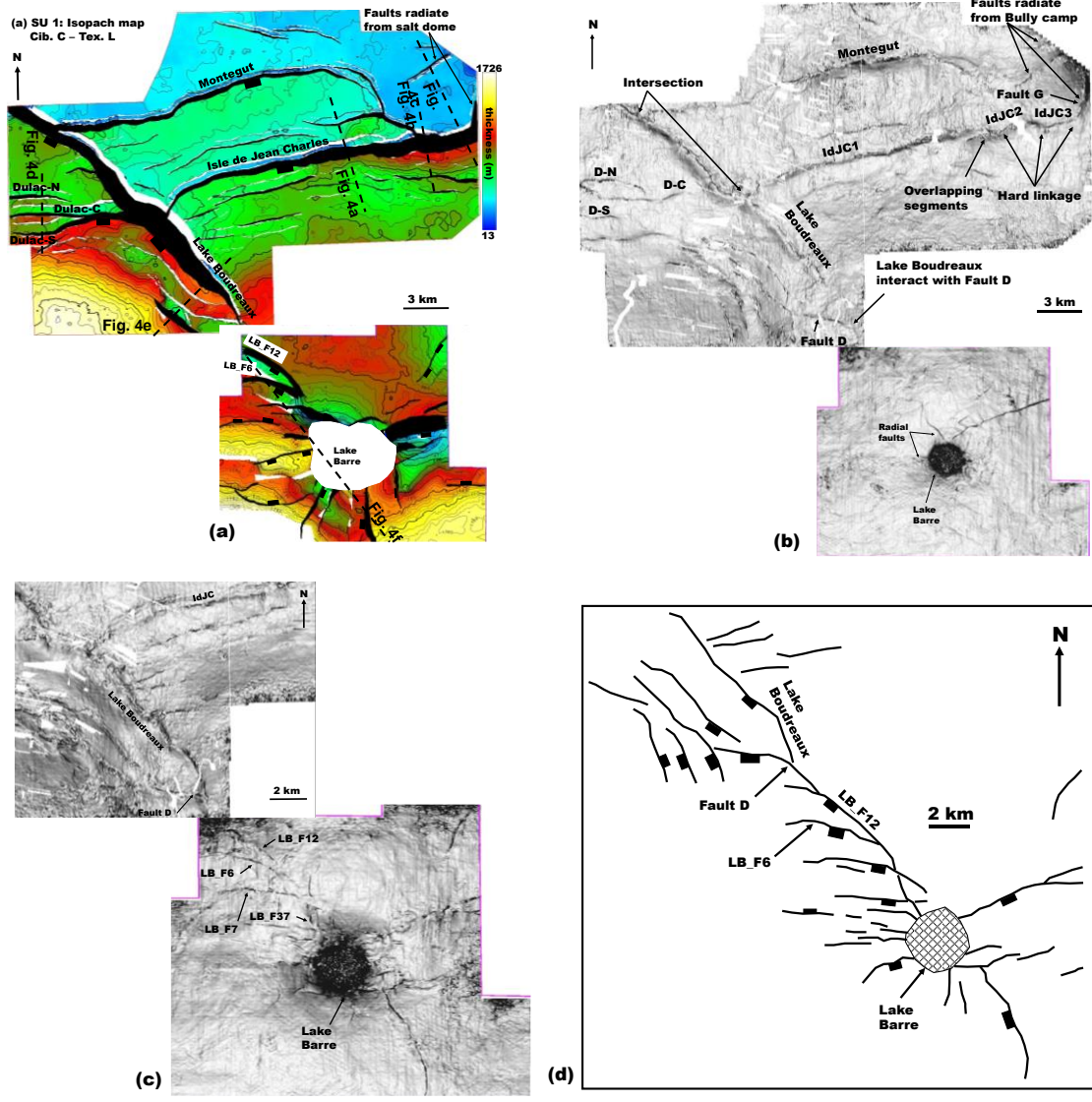
Figure 3.3. (a) Isopach map for stratal unit 1 (SU1). The IdJC fault appears as a single continuous fault. Strata thickness increases eastwards along IdJC, whereas thickness is higher on the SE portion of the Lake Boudreaux fault compare to its NW portion. The IdJC and Dulac-Center intersect Lake Boudreaux. Dulac-South intersects Dulac-Center, whereas Dulac-North did not intersect the later. Towards the southeast, Lake Boudreaux interacts with Fault D, whereas Fault D interacts with LB_F12. Broken lines show the location of seismic profiles in Fig. 3.4 (b) Dip of maximum similarity attribute map at 2.1 secs. The IdJC fault occurs as three segments at shallow strata units. Each segment is hard-linked to the next one. At the same time, only three radial faults are seen around Lake Barre salt stock. (c) A dip of maximum similarity attribute map at 2.6 secs. Lake Boudreaux fault interacts and bends towards Fault D. The later interacts with LB_F12. More radial faults and large faults interact with Lake Barre at this time. (d) A cartoon image of Fig 3.3c. All the faults except three around Lake Barre did not displace reflectors above 2.1 secs (see Fig. 3.3b)
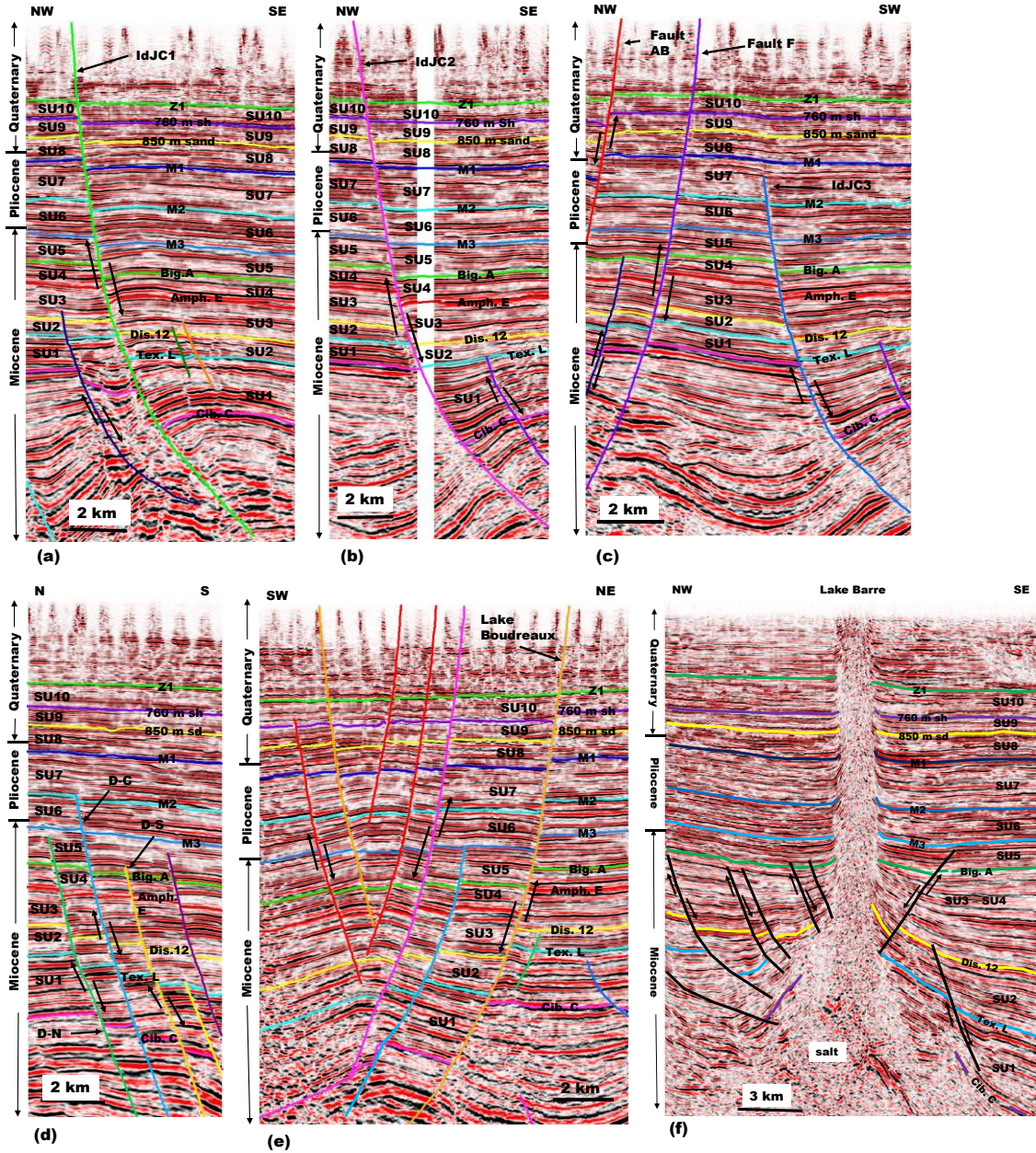
Figure 3.4. Seismic profiles show across fault strata thickening. Note the displacement on IdJC, Lake Boudreaux, Fault AB, and F extends to the top of the profile. (a) IdJC1. (b) IdJC2. (c) IdJC3, radial faults AB and G. Note the large offset of Z1 on Fault AB compare to Fault F. (c) Seismic profile showing Dulac-North (D-N), Dulac-Center (D-C) and Dulac-South (D-S). (d) The profile shows Lake Boudreaux and its graben. (e) Seismic profile across Lake Barre salt stock. Radial faults around the stock are contained within the Late Miocene strata. The diameter of the stock increases from M3 to M2 then decrease from M2 to 850 m sand. However, the stock diameter increase from 850 m sand up to its caprock.

Strata thickness varies spatially along the fault traces. During the Late Miocene SU1 (Fig. 3.3a), the IdJC was a single continuous fault with the fault heave increasing in width eastward, suggesting an increase in fault throw. Strata thicken eastwards along the fault trace reaching a maximum thickness of 1074 m where it intersects with Fault G, a radial fault from the Bully camp salt stock. Strata thickness also varies along the Lake Boudreaux fault with the higher thickness occurring at the southeastern portion of the fault. Unlike the IdJC fault, the highest strata thickness of 1726 m is located at the southwest corner of the 3D survey. Furthermore, the fault heave decreases rapidly towards the southeastern portion of the fault suggesting a rapid decrease in fault throw. Along radial fault LB_F12, strata thicken towards the northwest.

From SU2, the IdJC fault had become three right-stepping en echelon segments, namely IdJC1, IdJC2, and IdJC3 (Figs. 3.1 and 3.3b). These segments are hard-linked with the fault tip of the hanging wall fault intersecting the footwall fault (e.g., Childs et al., 1995); the east tip of IdJC1 intersects IdJC2, the east tip of IdJC2 is linked to IdJC3 whereas the east tip of IdJC3 intersects Fault G. The link between IdJC and Fault G was broken during the Pliocene because IdJC3 did not breach strata younger than SU8 (Fig. 3.4c). Monoclinal fold characterized the area above this fault segment.

In addition to IdJC3, other faults that did not propagate into Pliocene strata are the east-west striking faults south of the IdJC, Fault Southend and radial faults around Lake Barre (Fig. 3.3b). Although the Dulac fault continues to displace Pliocene strata, it begins to retreat westward and cease to intersect the Lake Boudreaux fault. The retreat of the Dulac fault led to a less complicated fault geometry; the fault geometry among the Dulac, Lake

Boudreaux, and IdJC changed from double-dropped down (e.g., Dickinson, 1954) to a T or Y shaped geometry (e.g., Maerten et al., 1999).

3.4.2 Throw Analysis for Isle de Jean Charles fault

The displacement profile (Fig. 3.5a) of this fault is asymmetrical with a higher throw skewed towards the Bully Camp salt stock. The throw gradient is higher around the intersecting portion of the fault segments and corresponds to the location of three-throw maximal. The first maximal is located at the east tip of IdJC1 at approximately 14 km; the second maximal is between the center and west tip of IdJC2, whereas the third at the east tip of IdJC3. These throw maximal separated by two throw minimal at approximately 16 km, and 20 km coincide with where each segment of the fault interacts with each other (e.g., Willemse et al., 1996; Young et al., 2001). The location of the throw maximal on IdJC1 and IdJC2 gradually move away from the intersecting fault tip during the Late Miocene *Cib.C* to *Big.A*, towards the center of each fault segment from the Pliocene M3 to Quaternary Z1. Temporally, there is a rapid decrease in throw, about 700 m, between *Cib.C* and *Tex.L* compared to less than 100 m decrease between successive younger horizons. Furthermore, the displacement profile during *Cib.C* forms a single continuous profile compared to the younger horizons, *Tex.L* to Z1, where the throw drops to zero at the tip of the fault segments.

The contour pattern and characteristic of the IdJC throw map (Fig. 3.5b) is a mirror image of its displacement profile. The eastward decrease in contour spacing is contemporaneous with an increase in contour values confirming that throw is skewed towards the east. The eastward throw trend is interrupted twice by vertical contour lines

along the fault trace at 16 km and 20 km. These vertical contours suggest plunging of fault tips associated with fault segmentation and interaction (Barnett et al., 1987; Baudon and Cartwright, 2008a; Childs et al., 1995) as depicted by throw being minimal on the displacement profile. Contour patterns remain horizontal at the eastern edge suggesting that throw continues to increase towards the Bully camp salt stock.

Temporal variation in fault throw is indicated by top to bottom decrease in contour spacing, which indicates increasing throw, and the horizontal to sub-horizontal nature of the contour lines suggests that the fault is syn-depositional (Childs et al., 2003). Widely spaced contours at the middle portion of the map, the Pliocene interval, compare to relative closely spaced contours within the Quaternary section, suggesting that activity decreased during the Pliocene but was rejuvenated in the Early Quaternary.

The displacement on the IdJC fault was progressively backstripped (Fig. 3.6). By SU1 (Fig 3.6a), IdJC was a single continuous fault with its western tip being 5 km away from intersecting with the Lake Boudreaux fault. By (SU2 (Fig. 3.6b), the fault was within the vicinity of Lake Boudreaux fault about 1 km away. At the same time, the fault appears as three segments on the surface. Physical interaction and intersection of the IdJC1 segment with the Lake Boudreaux fault did not occur until the deposition of SU3 (Fig. 3.6c). Although the fault segments did not interact physically with each other until the Pliocene, maximum displacement on IdJC1 is close to the segment's eastern tip, the maximum on IdJC2 alternates between the segment center and western tip whereas throw increases eastward on IdJC3. This throw pattern suggests that displacement on each segment complemented each others with the fault segments acting as if they were a single fault (e.g., Walsh and Watterson, 1991).
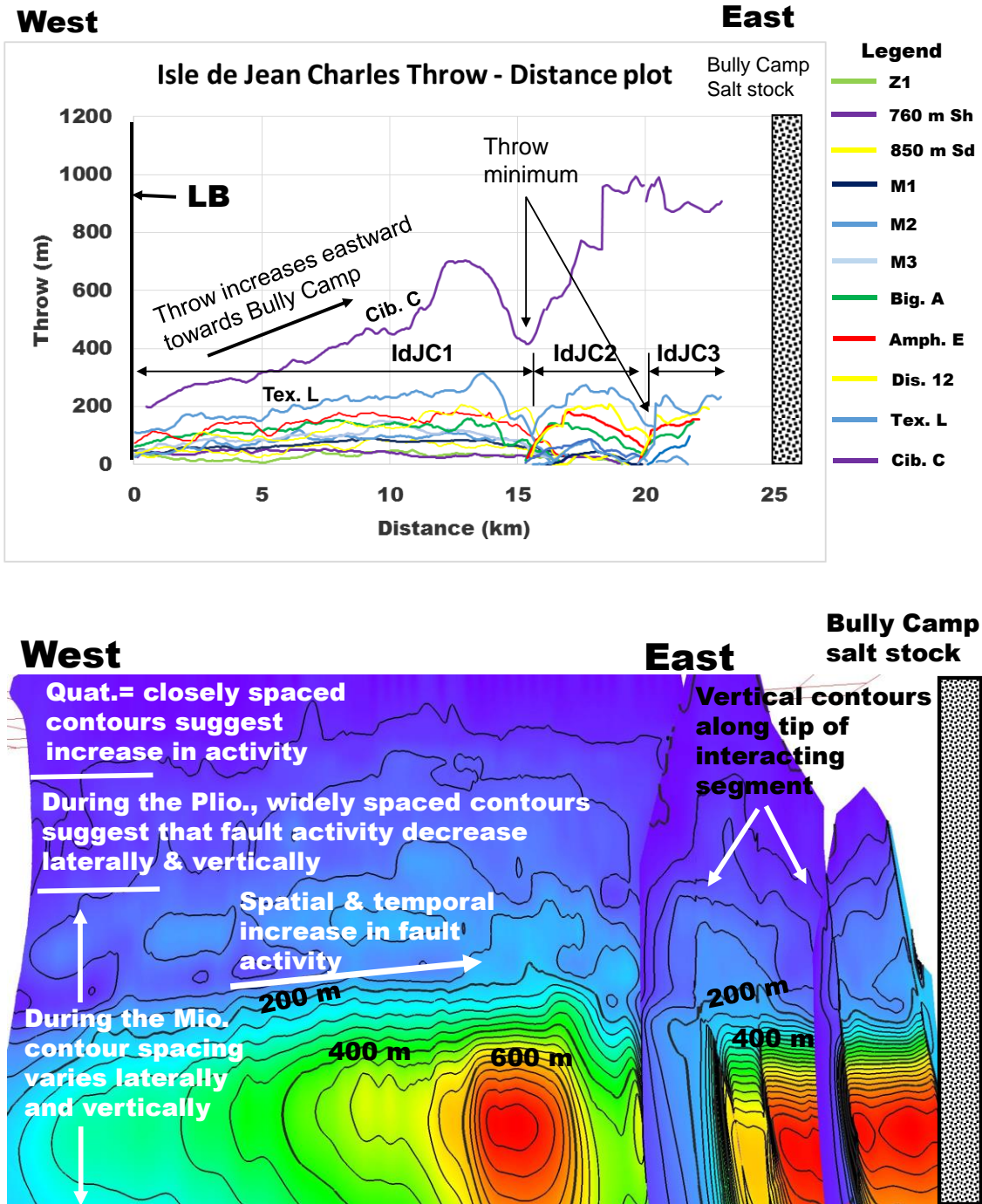
Figure 3.5. (a) Throw versus distance plot for Isle de Jean Charles. Throw increases eastward towards the Bully Camp salt stock. Throw minimal is located where each segment of the fault intersects each other. Overall, throw patterns show kinematic and geometric coherence. (b) Throw map for Isle de Jean Charles fault. Throw varies both spatially and temporally. Vertically contours towards the east are the location of fault intersection. Although segmented, the continuity of increasing throw towards the east suggests a kinematic and geometric coherent fault.

The throw-depth plot of the three segments of the Isle de Jean Charles fault (Fig. 3.7) shows a general increase in displacement. Their T-z plots show similar changes in gradient and three phases of activity. Phase 1 is characterized by a high gradient between 500 m and 750 m subsea, which corresponds to fast activity during the Quaternary period. A relatively low gradient follows this from the Quaternary-Pliocene boundary to about 2750 m that suggests a relatively slow activity. Phase 3, which is from 2750 m to 4300 m, corresponds to the Late Miocene has a higher gradient than the Pliocene and Quaternary and suggests a relatively fast activity. Although the fault segments show a similarity in general displacement pattern, their throw differs at similar depth. From 500 m to a depth of 2800 m, the throw of IdJC1 is higher than that of IdJC2 and IdJC3, suggesting that it was slipping faster than the two other segments, whereas from 3100 m to 4300 m, the throw of IdJC2 and IdJC3 are higher than that of IdJC1. Furthermore, between 2500 m and 3000 m, both IdJC2 and IdJC3 have almost identical throw.

Just like the throw map, T-x, and T-z plots, the expansion indices (Fig. 3.7) also show similar variation at similar depths and within strata units. During SU1, the high E.I. values of 3.3 and 3.8 for IdJC2 and IdJC3, respectively compared to 1.35 for IdJC1, suggest that both fault segments were slipping faster than IdJC1. By SU2, the E.I. had decreased on both IdJC2 and IdJC3, whereas E.I. of IdJC1 had increased to 1.7. From SU3 to SU5, the E.I. of the three segments had decreased to 1.2. During the Pliocene (SU6 –SU8), the E.I. further decrease on all segments to approximately 1, suggesting that very little syn-depositional activity (e.g., Thorsen 1963). This interval corresponds to the low gradient recorded on the T-z plot between 750 m and 2750 m. No E.I. values for IdJC3 beyond SU6 because the fault segment did not displace younger strata units. By

SU9, the E.I. began to increase on the remaining active segments, IdJC1 and IdJC2,

suggesting that strata expand across the fault due to the syn-depositional activity.
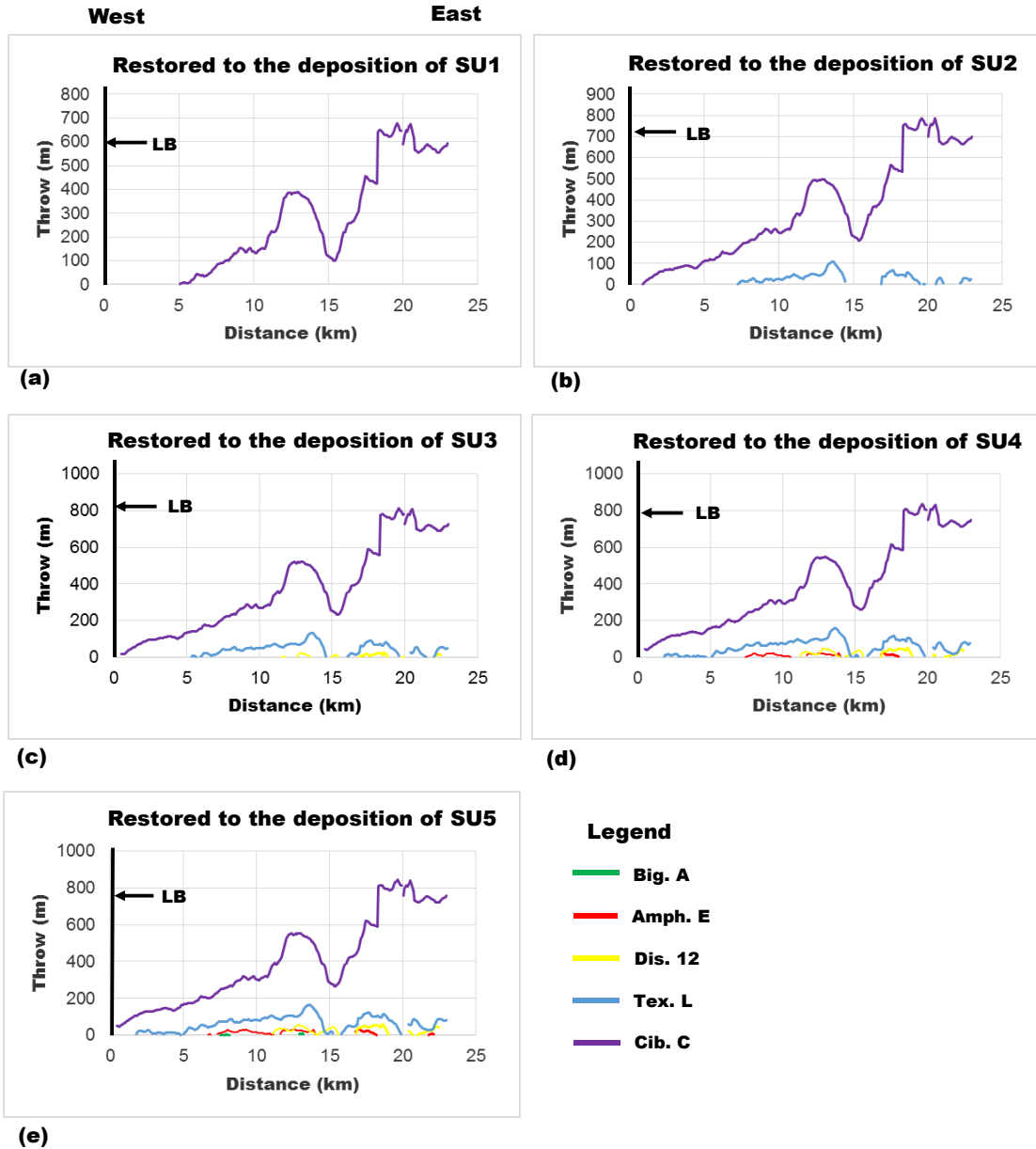
Figure 3.6. Backstrip throw profile for Isle de Jean Charles fault. (a) By SU1, the IdJC was 5 km away from the Lake Boudreaux fault. The fault continues to approach Lake Boudreaux during (b) SU2 until it eventually intersects the Lake Boudreaux fault during (c) SU3. Each segment of the IdJC fault begins to interact by (d) SU4 and (e) SU5.
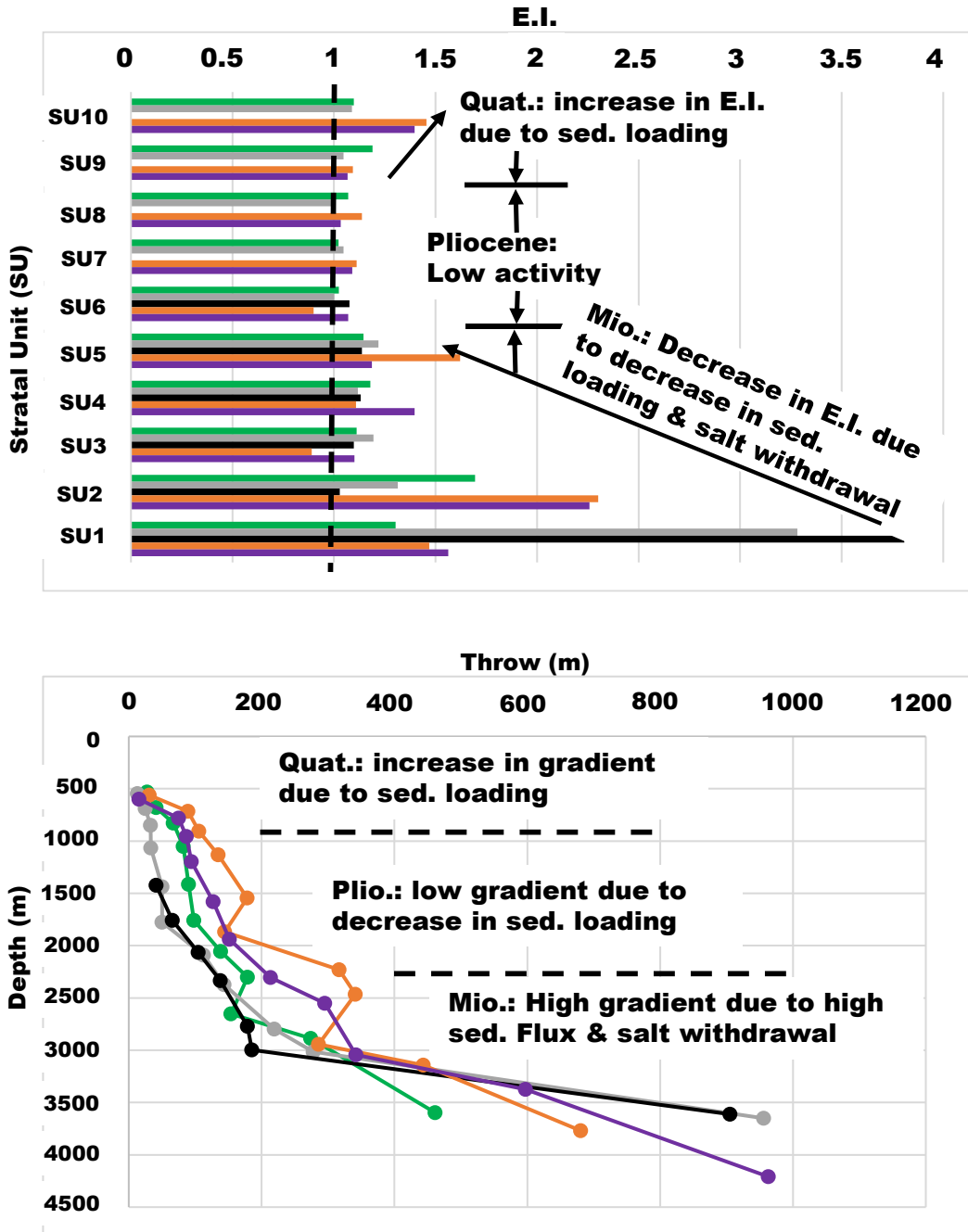
Figure 3.7. (Upper) The expansion Index for the IdJC1 (Green), IdJC2 (Black), IdJC3 (Gray), and Lake Boudreaux fault. The index decreased on both fault from SU1 to SU5. An index from SU6 to SU8 is approximately 1. However, the index increases upward from SU9. (Lower) Throw versus depth plot for Isle de Jean Charles segments and Lake Boudreaux fault. A relatively slow Pliocene activity separates the high activity during Quaternary and Miocene. The plot also shows that Lake Boudreaux's fault is slipping faster than the Isle de Jean Charles fault.

3.4.3 Throw Analysis for Dulac fault

The three faults accommodate the displacement on the Dulac fault (Fig. 3.8);
Dulac-North, Dulac-Center, and Dulac-South. The Dulac-North profile (Fig. 3.8a) is
asymmetrical in shape. The throw profile of the older Miocene horizons, *Cib.C*, *Tex.L,*
and *Dis.12*, is skewed towards the west, whereas that of the Latest Miocene horizons,
Amph.E and *Big.A* is skewed towards the east. At 3.2 km along the fault trace, there is a
rapid decrease in throw on all the horizons except *Big.A* that starts decreasing at 3.5 km.
This high gradient or steepness of the throw profile is characteristic of fault interaction,
i.e., soft-linkage and transfer of displacement to a neighboring fault (Peacock and
Sanderson, 1991), in this case, Dulac-Center.

The displacement profile of Dulac-South (Fig. 3.8c) differs from that of Dulac-
North. The Dulac-South intersect and physically interact with the Dulac-Center fault
from *Cib.C* to *Dis.12,* i.e., SU1 to SU2. Evidence of the interaction is seen in the throw
pattern of these horizons. The profile of *Cib.C* is asymmetrical and skewed towards the
east. Throw on this horizon began to plateau by 4 km until it reaches a maximum throw
of 397 m at 5.1 km. The throw pattern of *Tex.L* is almost symmetrical with throw
reaching a maximum of 150 m at approximately 2.9 km before decreasing to 2 m at 4.9
km. The profile of *Dis.12* also show a similar high gradient and decrease in throw at a
distance of 4 km. The *Amph.E, Big.A* and M3 show no evidence of an abrupt decrease in
throw because they do not physically interact with Dulac-Center.
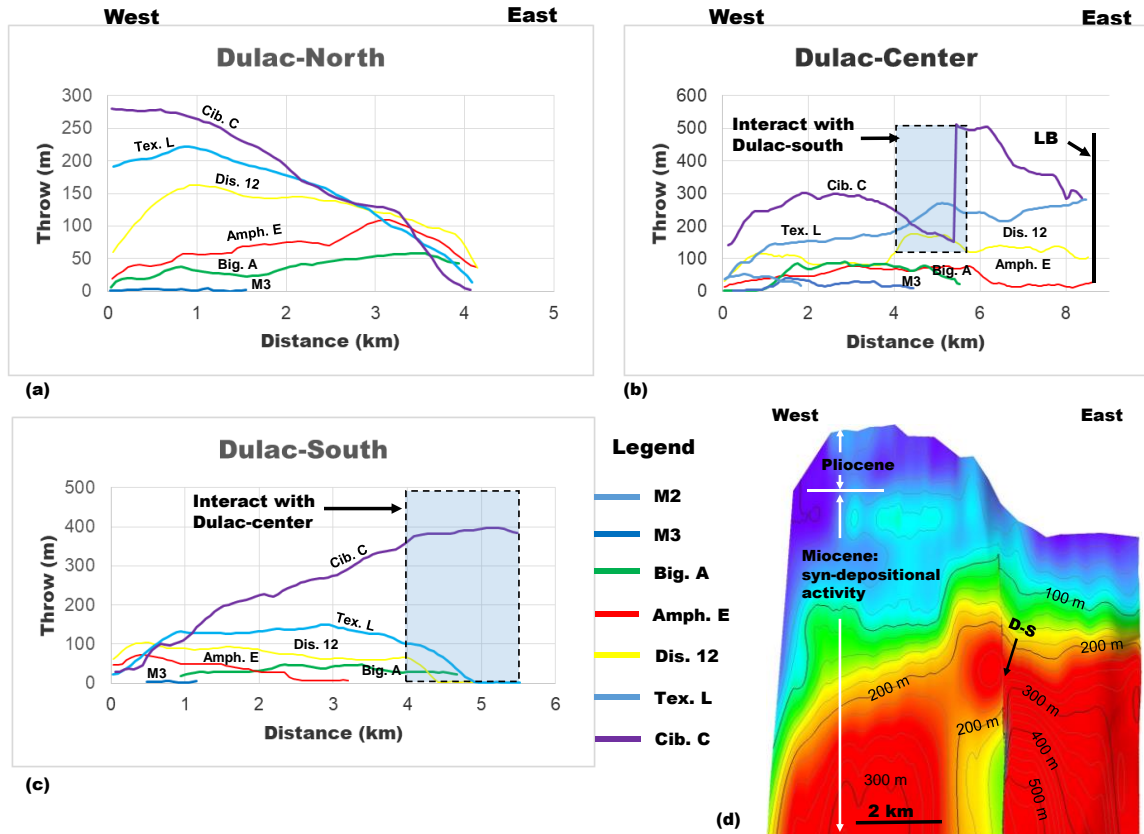
Figure 3.8. Dulac fault (a) Throw versus distance plot for Dulac-North. Throw increases toward the west. There is a high throw gradient at 3.2 km. (b) T-x plot of Dulac-Center. A rapid drop in throw at 5 km coincides with the intersection of Dulac-South. The vertical line at the east end of the profile is the intersecting location with Lake Boudreaux fault. (c) Throw versus distance plot for Dulac-South. Throw increase eastward towards Dulac-Center. (d) Throw map for Dulac-Center. Horizontal to sub-horizontal contours suggest a syn-depositional activity. The throw is higher on the east side compared to the west side.

The Dulac-Center (Fig. 3.8c) is interpreted as the master fault because it intersects the Lake Boudreaux fault, it interacts kinematically with Dulac-North, and physically and kinematically it also interacts with Dulac-South. Evidence supporting intersection with Lake Boudreaux fault is seen in the relatively high throw of 300 m for *Cib.C*, 280 m for *Tex.L*, 103 m for *Dis.12,* and 28 m for *Amph.E* at 8.3 km. The latest Miocene *Big.A* and the Pliocene M3 and M2 did not intersect the Lake Boudreaux fault. The abrupt increase

in throw of *Cib.C*, *Tex.L,* and *Dis.12* between 4 km and 5.5 km coincide with where Dulac-South intersect Dulac-center and where Dulac-North start accumulating displacement. The correlation of throw decrease on Dulac-North and Dulac-South with a corresponding increase on Dulac-North suggests a transfer of displacement to the latter (e.g., Peacock and Sanderson, 1991; Walsh et al., 2003). The throw increase on Dulac-Center by 150 m for *Cib.C* and 100 m for both *Tex.L* and *Dis.12*. The displacement profile of *Big.A* and M3 did not show any evidence of interaction with the other fault segments.

The throw map of Dulac-Center (Fig. 3.8d) shows a general increase in contour number towards the bottom of the fault, reaching a maximum of 520 m. The contour lines are mostly sub-horizontal to horizontal, suggesting syn-depositional activity (Childs et al., 2003). On the east side of the map, the lines are closely spaced and have higher contour values suggesting rapid activity compare to the widely spaced lines on the west side, which suggests relatively slower activity. Spatially, the contours plunge to the west edge, whereas there is an abrupt change in contour pattern at 5.5 km from sub-horizontal to sub-vertical and back to sub-horizontal. The sub-vertical lines are indicative of fault intersection (Barnett et al., 1987; Baudon and Cartwright, 2008a; Childs et al., 1995; Mansfield and Cartwright, 1996) in this case with Dulac-South. Similarly, higher throw values and sub-vertical lines characterized the east edge of the throw map suggesting intersection with the Lake Boudreaux fault.

The displacement profile of Dulac-Center was progressively backstripped (Fig. 3.9). The plot shows that Dulac-Center continues to intersect with Lake Boudreaux as early as SU1 (Fig. 3.9a). The gap on the backstrip of SU1 is due to the partial transfer of

displacement to Dulac-North and South. The Dulac fault continues to propagate upward throughout the Late Miocene (Fig. 3.9a-e).
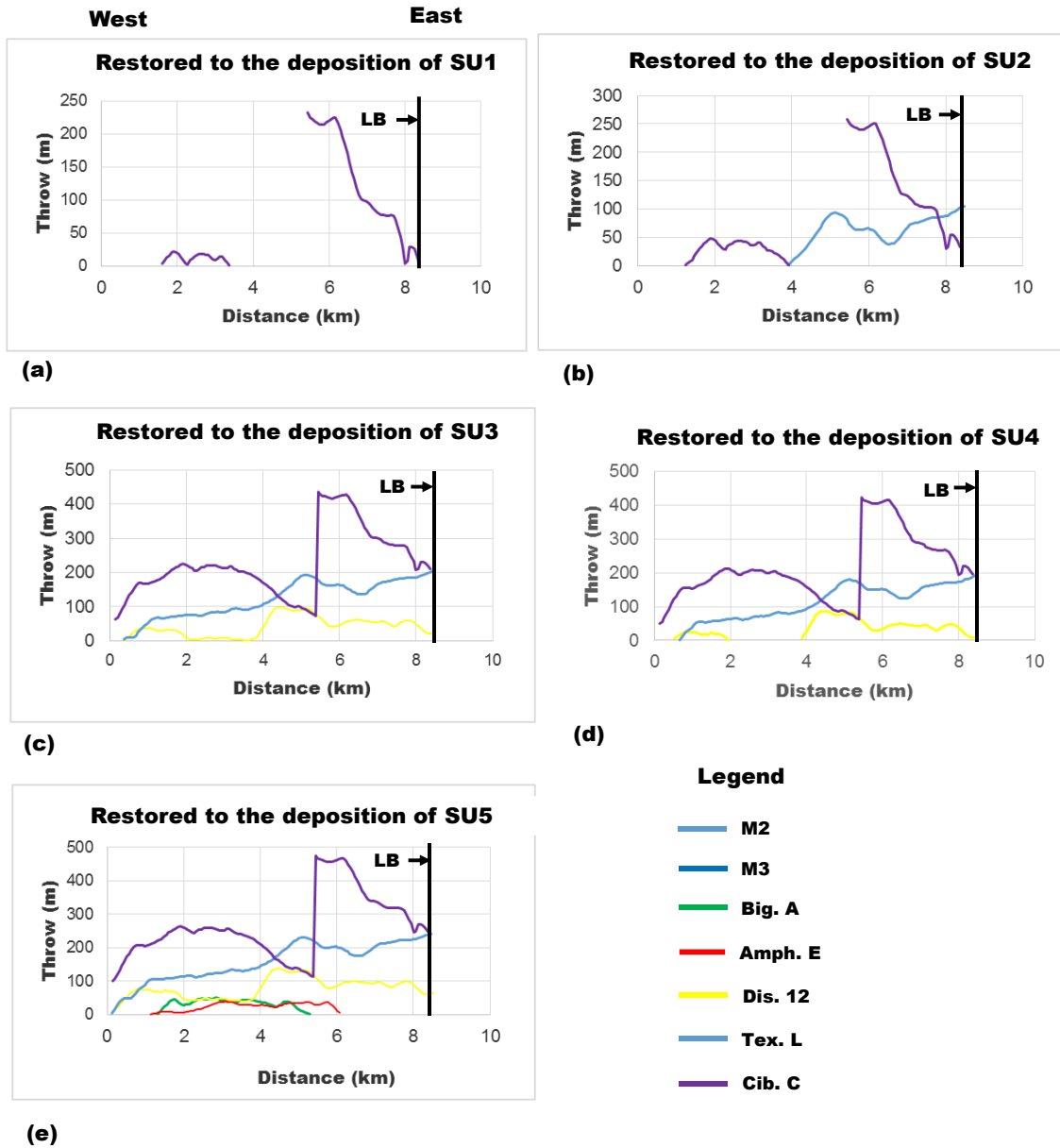
Figure 3.9. Backstripped plot for Dulac-Center. The fault had intersected Lake Boudreaux as early as SU1. The vertical black line is where the fault intersects the Lake Boudreaux fault.

3.4.4 Lake Boudreaux Fault

The displacement profile of the Lake Boudreaux fault (Fig. 3.10a) is asymmetrical even though the maximum throw is located at the fault center. The profile shows a low gradient at the northwest portion, changing to a high gradient at the southeast portion. Furthermore, throw decreases rapidly on the southeast portion, especially during *Cib.C*, *Tex.L,* and *Dis.12* where throw decreased by 1090 m, 855 m, 450 m, respectively, within a distance of 10 km. The decrease in throw on the northwest portion is not as rapid as that of the southeast portion. In addition to the general throw trend, throw also change abruptly along the fault strike. Instances of abrupt increase or decrease in throw correspond to where basinward dipping east-west striking faults intersect the Lake Boudreaux fault. The intersection and hard linkage of the Montegut and Isle de Jean Charles fault on the footwall resulted in a decrease in throw, whereas the intersection of Fault L and Dulac fault on the hanging wall led to an increase in throw.

Temporally throw decreases rapidly between Late Miocene horizons such as 338 m between *Cib.C* and *Tex.L*, 349 m between *Tex.L* and *Dis.12*, 121 m between *Dis.12* and *Amph.E.* The amount of decrease between two successive horizons began to diminish towards the end of the Miocene as indicated between *Amph.E* and *Big.A* with a 40 m decrease. This trend of minimal decrease in throw continues throughout the Pliocene, from M3 to M1, averaging about 17 m. However, during the Quaternary period, the throw decrease of 80 m between 760 m Shale and Z1 suggests a rejuvenation of fault activity.
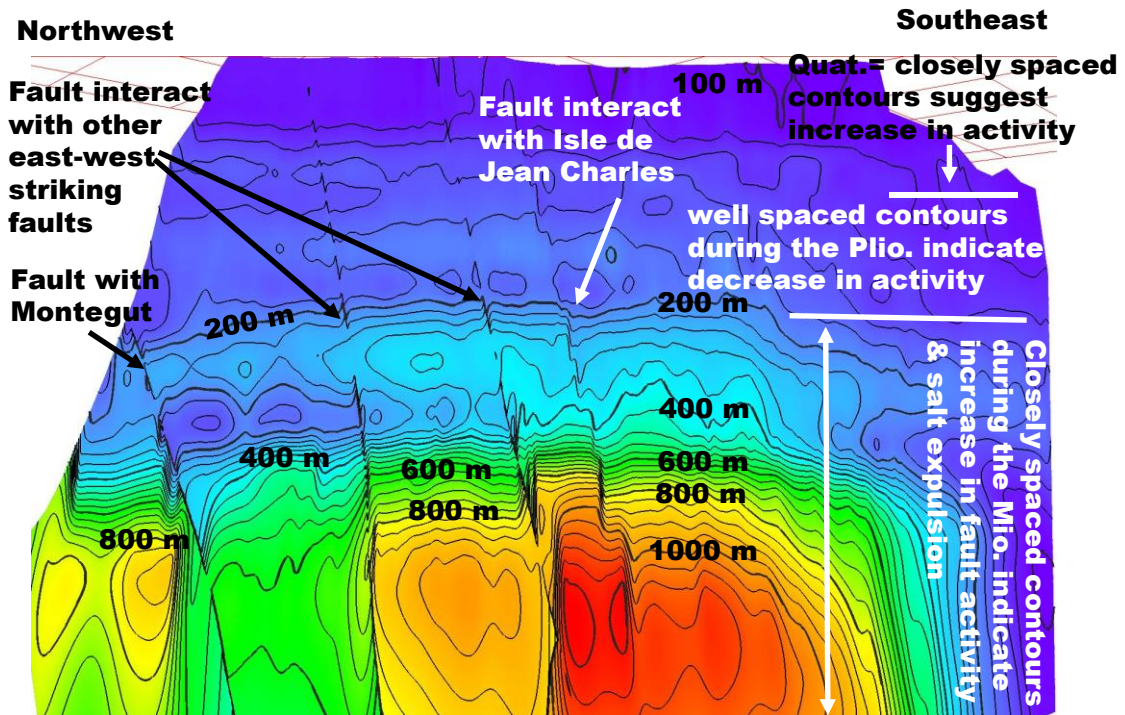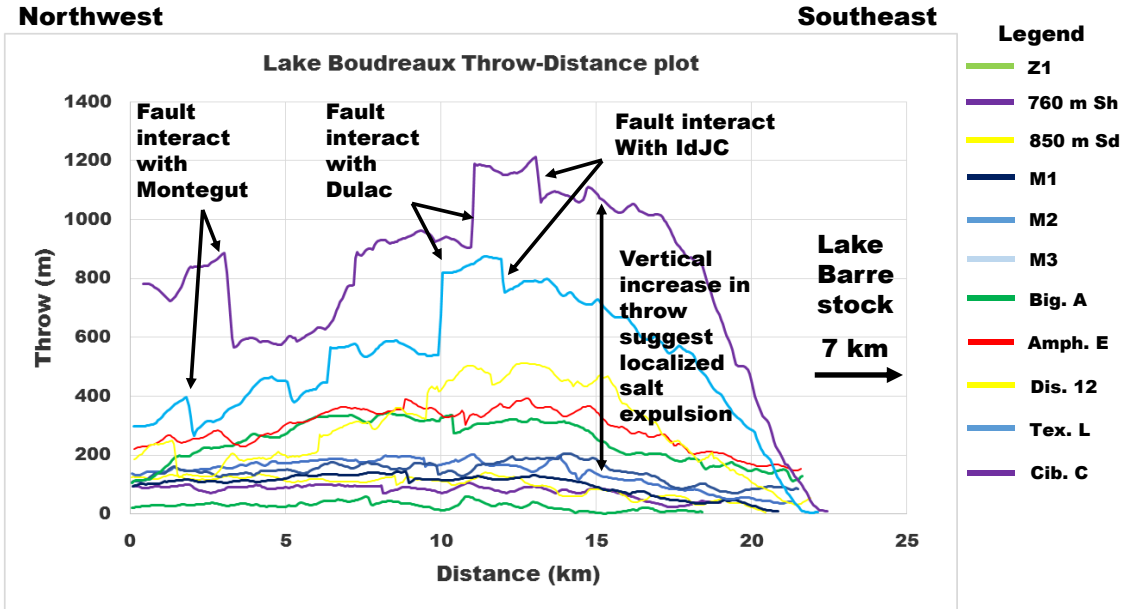
Figure 3.10. (a, upper) Throw versus distance plot for Lake Boudreaux fault. The throw gradient is higher on the southeast portion compare to the northwest portion of the fault. (b, lower) Throw map for Lake Boudreaux fault. The contour pattern abruptly changes from horizontal to vertical at the southeast portion as the fault approaches Lake Barre salt stock.

The contour map of the Lake Boudreaux fault (Fig. 3.10b) also shows spatial and temporal throw variation, as depicted on its throw profile. The contour lines are mostly sub-horizontal to horizontal, suggesting syn-depositional fault activity (Childs et al., 2003). The sub-horizontal lines at the northwest edge of the map suggest that syn-depositional fault activity extends beyond the limit of the 3D survey. There are areas where the contour lines are not horizontal, e.g., plunging vertical contours toward the southeast edge of the fault suggest the fault tipping outward. There are also intervals of abrupt change in contour pattern from horizontal to sub-vertical, suggesting fault intersection (e.g., Mansfield and Cartwright 1995). These instances correspond to where east-west striking faults intersect and are hard-linked to the Lake Boudreaux fault; contour values decreasing abruptly when the Montegut intersects the fault, whereas contour value increases when intersected by Dulac fault.

The map also shows temporal throw variation as depicted by variation in contour spacing. Contours in the upper half of the map are well spaced compared to closely spaced contours at the bottom that indicate rapid fault activity. Within the upper portion, the amount of spacing also varies. The contours are relatively closely spaced at the top of the upper quarter compare to the middle portion of the fault suggesting that fault was slipping faster during the Quaternary than the Pliocene.

The throw–depth plot (Fig. 3.7) show a general increase in throw with depth. Just like the T-z of IdJC, fault activity on this fault is sub-divided into three phases based on throw gradient. The first phase, a high gradient phase, is from 500 m to 750 m, the second phase with a relatively low gradient corresponds to 750 m to 2750 m, whereas the third phase is from 2750 m downward. Of the three phases, the third phase, with a

85

gradient of 0.48 and 0.53 for the northwest and southeast portion respectively, has the highest gradient and corresponds to a period of rapid faulting during the Late Miocene SU1-SU3, i.e., *Cib.C* to *Dis.12*. Activity differs on the northwest and southeast portion of Lake Boudreaux fault.

During the Quaternary and Pliocene, i.e., phases one and two, respectively, the northwest portion of the fault was slipping faster than the southeast portion. However, by the Late Miocene *Dis.12* or SU3, the southeast portion began to slip faster than the northwest portion.

The expansion indices (Fig. 3.7) also show a temporal variation on the fault. Fault activity was high during SU1 and SU2, as indicated by E.I. reaching 2.3 and 2.2 on the northwest and southeast portion, respectively. From SU3, syn-depositional activity began to decrease, as suggested by a drop in E.I. values to 0.9 and 1.1 on the northwest and southeast portion. However, during SU4 and SU5, E.I. increases intermittently on the southeast and northwest portion, respectively. Strata expansion across the fault was minimal during SU6 and SU7. However, by SU8, activity began to peak on the fault reaching an E.I. of 1.4 by SU10.

3.4.5 Lake Barre Fault 12

LB_F12 is a fault that radiates within the vicinity of the Lake Barre salt stock (Figs. 3.1, 3.3a, 3.3b, and 3.3d). This fault strike northwest for its first 5.9 km before bending west. It is restricted within the Miocene section displacing *Cib.C*, *Tex.L*, *Dis.12*, *Amph.E,* and *Big.A* horizon (Fig. 3.3b, 3.3c, and 3.3d). Throw profile (Fig. 3.11) of these horizons is asymmetrical, with throw increasing towards the northwest. The maximum

throw attained during *Cib.C*, *Tex.L* and *Dis.12* are 761 m, 510 m, and 253 m,

respectively. Based on the northwest throw increase and the bend in fault strike, this fault

may be associated with a structure that is located northwest or west of Lake Barre salt

stock, probably the Bay St. Elaine salt stock.

The faults around Lake Barre radiates outward from the salt stock. These faults

mainly displace Late Miocene strata, i.e., SU1 to SU5. Rock strata thin towards the salt

stock. From SU6 upward, none of the faults breached the Pliocene and Quaternary

horizons. However, there is a remarkable change in the diameter of the stock. The

average diameter of the stock during SU is 1.7 km. By SU6, the stock's diameter had

decreased by 29% to 1.2 km. However, the diameter increased again from M1 to Z1 to

1.6 km.
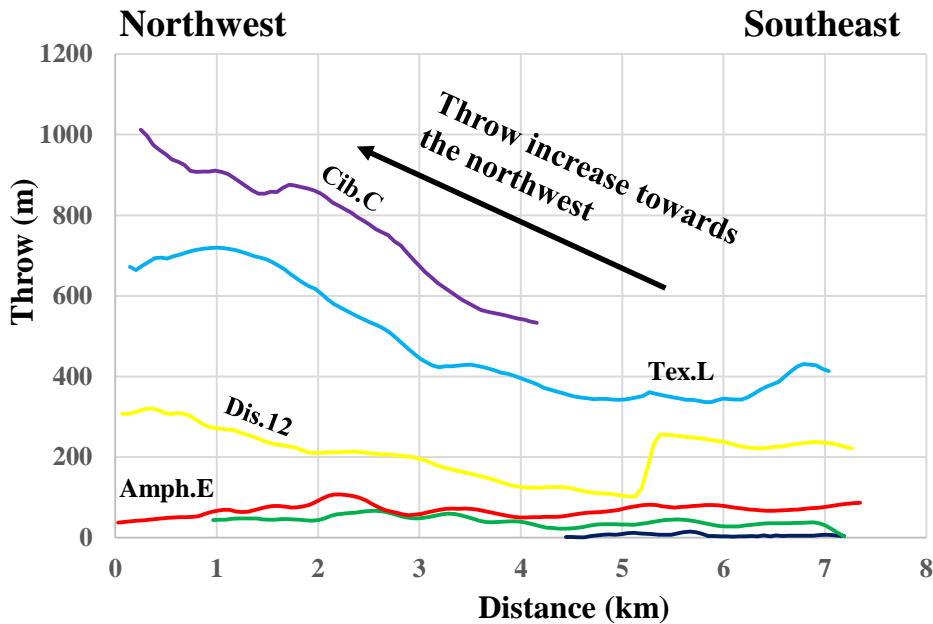
Figure 3.11. Throw versus distance plot for F-12. Throw increases toward the northwest,
suggesting that the fault does not intersect the Lake Barre salt stock.

3.5 Interpretation of fault patterns

3.5.1 Mechanism of propagation of the Isle de Jean Charles fault

The three fault segments of the IdJC fault, IdJC1, IdJC2, and IdJC3, appear to be kinematic and geometric coherent, i.e., they are slipping like a single fault array (e.g., Childs et al., 1995; Walsh & Watterson, 1991; Walsh et al., 2003). Evidence to support their genetic, kinematic and geometric coherence is a) fault throw increases towards the Bully Camp salt stock, b) the three fault segments behave like a continuous single fault trace, c) the pattern of strata thickness are higher on certain portions of the fault, and d) location of throw maximum and direction of propagation.

The asymmetrical displacement profile of the fault and the general eastward increase in throw (Fig. 3.5a and b) with the maximum throw located within the vicinity of Bully camp stock suggest that the segments were not unrelated isolated faults but are coherent fault segments (e.g., Walsh and Watterson, 1991; Childs et al., 1995; Walsh et al., 2003). Furthermore, the relative high throw gradient of IdJC2 and IdJC3 at the beginning of the Late Miocene, as seem on the T-z plot (Fig. 3.7), suggest that throw continue to increase towards the stock.

The IdJC segments propagate like a single fault. The transfer of displacement between each segment, as depicted by an eastward increase in throw on throw map, complement each other (Fig. 3.5b). The segments intersect/link at depth (Figs. 3.1 and 3.3b) to form an intersection line similar to the L-shape branchline of Walsh et al. (1999) and suggest that the three segments form a single master fault.

The pattern of the strata thickness along the IdJC suggests that the fault behaves like a continuous fault. The depocenter is continuous during SU1 with strata thickness

88

increasing eastward and reaching a maximum thickness exceeding 1000 m (Fig. 3.3a) around Bully Camp stock. Furthermore, the relative high E.I. of IdJC2 and IdJC3 with respect to IdJC1 during SU1 (Fig. 3.7) confirms that the fault was a single continuous fault at the beginning of the Late Miocene. However, during SU5, the fault was segmented with each segment having a depocenter.

The IdJC fault propagate from Bully Camp eastwards. The pattern of displacement and location of the throw maximal on the eastern portion of IdJC1, IdJC2, and IdJC3 contradicts that of interacting or intersecting isolated faults (e.g., Peacock and Sanderson, 1991; Willemse et al., 1996). Plots of displacement backstripping (Fig. 3.6) shows the IdJC fault as a single continuous fault propagating towards the Lake Boudreaux fault. It was not until SU3 (Fig. 3.6c) that the fault intersected the Lake Boudreaux fault. This pattern of fault propagation and the location of throw maximum at the third segment of the fault array indicate that the IdJC fault is genetically coherent.

3.5.2 Relationship between the Dulac and Isle de Jean Charles faults

A comparison of the displacement profile and the backstripped displacement of Dulac fault (Figs. 3.8b and 3.9) and IdJC (Figs. 3.5a and 3.6) suggest that these two faults are not related. Both the displacement profile and throw map of IdJC show decreasing throw towards the intersection with Lake Boudreaux fault. Around the intersection point, the throw of IdJC on *Cib.C*, *Tex.L,* and *Dis.12* are 200 m, 110 m, and 41 m, respectively. These throw values are lower than those on the Dulac fault for *Cib.C*, *Tex.L,* and *Dis.12* whose throw values are 290 m, 280 m, and 104 m, respectively. Furthermore, the contour pattern of IdJC plunges downward at the intersection point, whereas those of Dulac fault

89

is horizontal to sub-horizontal. Furthermore, the cumulative throw of Dulac-North, Dulac-Center, and Dulac-South show that throw increases westward, suggesting that Dulac fault is distinct from IdJC and propagated eastward to Lake Boudreaux fault.

The propagation direction of both faults based on displacement backstripping show that both faults propagated in opposite directions (Figs. 3.6 and 3.9). As early as SU1 (Fig. 3.9a), the Dulac fault had intersected the Lake Boudreaux fault while the IdJC fault (Fig. 3.6a) was still propagation toward it and was 5 km away from intersecting the Lake Boudreaux fault. Intersection and linkage of IdJC with Lake Boudreaux fault did not occur until SU3 (Fig. 3.6c).

3.5.3 Interaction of the IdJC fault with the Bully Camp salt stock

The increase in throw towards Bully Camp salt stock (Fig. 5a and b) and the interaction of a radial fault with IdJC (Figs. 3.1, 3.3a, and 3.3b) suggest that the Bully Camp salt stock strongly controls IdJC displacement pattern. Salt-fault interaction in salt basins show that displacement is highest at the point of interaction of a fault with a salt structure (e.g., Tvedt et al., 2016). Displacement consequently decreases outward from the salt structure (Fig. 3.5a and b).

3.5.4 Mechanisms responsible for throw variation on the Lake Boudreaux fault.

The throw on the Lake Boudreaux fault varies spatially due to three different mechanisms a) interaction with a radial fault, b) interaction with an east-west striking fault, c) interaction with graben faults and d) influence of the Lake Barre salt stock.

Lake Boudreaux decrease in throw as its approach radial fault LB_F12 (Figs. 3.1, 3.3c, 3.3d, 3.10a, and 3.10b). There is no hard linkage between both faults. The kinematic of both faults is different. The LB_F12 displaced strata older than the Pliocene (Figs. 3.1, 3.3a, 3.3c, 3.3d, 3.11) and did not propagate above 2.1 secs (Fig. 3.3b), whereas the displacement on the Lake Boudreaux fault extends into the Quaternary strata (Fig. 3.4d). The difference in the displacement pattern of both faults suggests that different stress states perturb them.

The displacement on Lake Boudreaux fault is inhibited by the presence of an east-west striking fault, Fault Southend (Fig. 3.1). This fault dips northward and appears not to displace strata younger than the Early Pliocene, just like the majority of the other east-west striking faults. The location and orientation of this fault may have restricted further propagation of the Lake Boudreaux fault towards Lake Barre salt stock.

The graben and the Lake Boudreaux fault are kinematically coupled (Figs 3.3b, 3.3c, 3.3d, and 3.4. The two faults that define the east edge of the graben, Fault D and Fault E (Figs. 3.1 and 3.3d), show evidence of an increase in throw towards the southeast, whereas throw on Lake Boudreaux decreases southeastwards. Both Fault D and Fault E appear to continue southwards and probably interact with the same salt structure as LB_F12.

The stress regime within the vicinity of Lake Barre appears to inhibit further southward fault propagation. Most radial faults that are associated with the Lake Barre salt stock are restricted to the Miocene strata, i.e., below 2.1 secs (Figs. 3.3c and 3.4f). The absence of fault displacement above 2.1 secs coincides with the Pliocene time interval. At the same time, the diameter of the Lake Barre salt stock increased by 25 %

(Fig. 3.4f). The absence of faults during the Pliocene and Quaternary, and the increase in stock diameter is a characteristic feature of the transition from active to passive diapirism (e.g., Vendeville and Jackson, 1992; Sabate, 1968). Passive diapirism is favored when the regional extension ceases or decreased significantly with salt stock accommodating all the strain/extension (Vendeville and Jackson, 1992b). The lack of propagation of Lake Boudreaux into the Lake Barre is due to the absorption of the strain by the salt stock.

3.5.5 Similarity between the Lake Boudreaux and the Isle de Jean Charles fault

Both the Lake Boudreaux and Isle de Jean Charles fault show similar temporal throw history. Both show three phases of activity. The first being rapid activity during the Late Miocene, which is due to rapid sediment loading (Galloway, 2001; Galloway et al., 2011) and salt withdrawal (Frey and Grimes, 1970; McBride, 1998; Schuster, 1995; Seni, 1992). This is followed by a relative quiescent phase, the Pliocene phase, associated with decreasing fault activity on the large faults and cessation of the majority of the east-west striking faults and radial faults around the Lake Barre. This decrease in activity is due to the location of the Pliocene depocenter south/basinward of the study area (Galloway, 2001). Rejuvenation of fault activity is common to both faults during the Quaternary. This is due to the reloading of the area with sediment during the Quaternary (Coleman and Roberts, 1988a; Coleman and Roberts, 1988b; Galloway, 2001).

The slip rates on both faults vary temporally (Table 3.1). During the Late Miocene, the IdJC fault was slipping faster than the Lake Boudreaux fault by at least 0.2 mm/yr. The former began to slip faster towards the latest Miocene with a rate of 0.054 mm/yr compared to the IdJC rate of 0.069 mm/yr. The Pliocene to the Quaternary rates

shows that Lake Boudreaux was slipping faster. This higher rate correlates with relative

high E.I of Lake Boudreaux during SU7 and SU8.

Table 3.1. Slip rates of Isle de Jean Charles and Lake Boudreaux fault. The rates decrease
from SU1 to SU4

Stratal Unit	IdJC 1	IdJC 2	IdJC 3	LB NW	LB SE
——— 850 m Sand					
SU 5 to SU 8	0.012	0.013		0.036	0.022
——— Big. A					
SU 4	0.09	0.069	0.07	0.054	0.18
——— Amph. E					
SU 3	-0.018	0.056	0.03	-0.041	0.035
——— Dis. 12					
SU 2	0.23	0.11	0.012	0.3	0.48
——— Tex. L					
SU 1	0.20	0.74	0.78	0.26	0.4
——— Cib. C					

3.6 Discussion and implications for fault kinematics in salt basins

The temporal throw pattern of faults in the Lapeyrouse-Chauvin area is

comparable with those in offshore Angola (Dutton and Trudgill, 2009), Eugene Island in

the Gulf of Mexico (Alexander and Flemings, 1995), and Viking Graben in the North Sea

offshore Norway (Jackson, 2017). Faults in these basins show three distinct phases of

fault activity; inception, rapid growth phase, and fault cessation (Alexander and

Flemings, 1995; Dutton and Trudgill, 2009; Jackson, 2017). In contrast, the temporal

history of the Lapeyrouse-Chauvin faults, due to limited biostratigraphy data, is assessed

from the Miocene rapid growth stage to recent. The rapid growth phase of Angola

(Dutton and Trudgill, 2009), Eugene (Alexander and Flemings, 1995), North Sea

(Jackson, 2017), and the Lapeyrouse-Chauvin area faults are associated with high sediment flux and salt withdrawal. Fault activity in these basins stopped due to salt depletion and welding of depocenter, whereas activity in the Lapeyrouse-Chauvin area was punctuated by the offshore migration of the Pliocene depocenter.

Omale and Lorenzo (2015), in their kinematic study of faults in the onshore Gulf of Mexico, observed episodic fault activity. Faults in southeastern Louisiana show two periods of high activity, a Paleocene and Miocene phase separated by low activity from the Eocene to the Oligocene (Omale and Lorenzo, 2015). In comparison, faults within my study area show Miocene and Quaternary activity separated by relatively low activity during the Pliocene. The result of my work and Omale and Lorenzo (2015) shows that faults in southeastern Louisiana have experienced at least three phases of rapid activity separated by low activity. Fault activity in this region is directly correlated with sediment loading.

The spatial history of the Lapeyrouse faults is compared to faults in other basins based on their kinematical and geometrical coherence and the diapiric stress perturbation. An example of coherent fault is the Sembo Relay System in offshore Angola (Dutton and Trudgill, 2009). Two faults make up the relay zone, a footwall fault and a hanging wall fault. Both faults are connected by a linkage fault. Unlike the IdJC, whose segments are formed simultaneously, the footwall fault in the Sembo Relay System is older than the hanging wall fault. The time difference in fault propagation has kinematic implications. At deep depth, both faults show no evidence of interaction or coherence. However, at a shallower depth, both faults are kinematically coherent. The IdJC, on the other hand, shows kinematic coherence throughout its history (Fig. 3.5b).

Another example is from the Central North Sea (Childs et al., 1995). Two overlapping right stepping faults, Fault 2 and Fault 1 that are 2 km and 3.2 km in length respectively, are soft-linked. A plot of throw against distance and throw map shows the throw on the smaller fault, Fault 2, transferred onto Fault 1. Unlike interacting isolated faults where there is a large throw minimal at the interacting point (e.g., Peacock and Sanderson, 1991), the pattern of throw distribution on the North Sea faults show an increase in throw from Fault 2 to Fault 1, suggesting that both faults are kinematic coherent. This is similar to the displacement distribution on the IdJC fault except that the maximum throw is located on the smallest segment, IdJC3.

Faults in the Gulf of Mexico show evidence of genetic coherence (Childs et al., 1995). In Childs' study, a fault is single and continuous during the pre-rift strata, whereas it propagates as two segments during the syn-depositional phase. The transition from a single fault to a segmented fault occurs just before the deposition of the syn-depositional strata. In contrast, the transition from a single fault to segmented faults for the IdJC occurred due to the decreasing sedimentation rate toward the end of the Miocene.

On a basin scale, the displacement pattern of a basin-bounding fault, Fault B, in the northern Polhem Subplatform, southwest Barents Sea (Kairanov et al., 2019) shows similarities and differences with the IdJC. Fault B is 40 km long within the Polhem 3D dataset but extends beyond the data boundary (Kairanov et al., 2019), whereas the IdJC is 23 km long. Both faults initially propagated as segmented faults but later linked to form a single fault. However, Fault B differs from IdJC in that before linkage, each segment has a distinct depocenter and displacement pattern (Kairanov et al., 2019), which suggests that it propagated as unrelated isolated segments. In contrast, the IdJC fault behaves as a

single fault from initiation, having a continuous depocenter at the beginning of the Late Miocene.

The throw pattern of the IdJC fault also compares to faults within the Egersund Basin in the Norwegian North Sea. Three faults in this basin are at least 12 km in length, and they interact with one of the two salt stocks, Delta and Omega stocks (Tvedt et al., 2016), just like the IdJC fault interact with the Bully Camp stock. The strike of the North Sea faults changes by 90^0 towards the stocks before intersecting it (Tvedt et al., 2016). Similarly, the change in the strike of the IdJC by approximately 100^0 is due to its intersection with a radial fault from the Bully Camp stock. The abrupt change in the strike of both faults suggests that the stress field of the salt stocks influences the displacement pattern.

The influence of hoop stress can also leave behind evidence of pre-existing or different stress states. In the North Sea, faults that were initially formed as polygonal faults and later rotated to radiate faults due to the influence of hoop stress of the North and South Pierce stocks have a dumb-bell displacement profile (Carruthers et al., 2013). Similarly, radial faults around the Lake Barre stock were constrained within the Miocene strata, i.e., below 2.1 seconds compared to the Lake Boudreaux fault that extends to the top of the seismic survey. The lateral extent of the hoop stress around the North Pierce stock increased during the Late Oligocene active diapirism, whereas the extent shrunk during the Early Miocene due to decreased diapirism (Carruthers et al., 2013). The maximum extent of hoop stress around the Lake Barre during the Miocene, estimated using 2-6 times the radius of a diapir (Bowers, 2007; Carruthers et al., 2013; Fredrich et al., 2003; Sanz and Dasari, 2010) is 9 km. The last 1 km of the southeast fault tip of Lake

Boudreaux falls within Lake Barre's stress field. The overlap of the fault with the stress field suggests that the Lake Barre perturbed the fault's displacement pattern and caused the rapid decrease in throw towards the stock.

The outcome of this work suggests that faults around salt stocks may be subjected to a different level of stress. For basin analysis, geologists should carefully compare the similarity in geometry and mechanism of formation of faults before using the stress analyses of a known fault for another fault. Though two salt stocks may have formed simultaneously and show similarity in radial fault patterns, the magnitude of hoop stress and their effect on nearby fault may differ from one to another. This stress, if not properly evaluated, can cause significant damage to the wellbore.

3.7. Conclusions

Kinematic analysis of spatial and temporal variation along salt-related faults led to the following findings;
 i) the Lake Boudreaux and the Isle de Jean Charles faults show similar temporal history
ii) spatial variation in throw on the IdJC fault is due to its mechanism of formation; genetically coherence fault array whereas spatial variation in throw on the Lake Boudreaux fault is influenced by intersection and interaction with east-west striking faults.
iii) both faults interacted with adjacent salt stock in different ways. The interaction of IdJC with Bully Camp led to an increase in throw towards the stock, whereas the interaction of Lake Boudreaux with a radial fault led to a rapid decrease in throw.

Furthermore, Pliocene and Quaternary strain/extension within the Lake Barre area is accommodated by an increase in the diameter of the Lake Barre stock.

Chapter 4

Geometry and characteristics of faults connecting two salt stocks: Insights from the Gulf of Mexico

Abstract

Faults in salt basins often intersect and connect two nearby salt structures. In this study, three different conceptual models are considered to explain the formation of this type of salt-related fault. Model 1 involves the propagation and intersection of two radial faults from two separate salt stocks. Model 2 is a hypothetical radial fault formed adjacent to a stock that propagates into neighboring stock. The last model considers a fault that develops between two stocks and eventually intersects both. Fault formed by each model has a unique displacement pattern. Using isopach maps, throw-distance plots, throw maps, and displacement backstripping, these hypothetical scenarios were tested using a large 3D mega-survey data from the Terrebonne Salt Withdrawal Basin in the Gulf of Mexico. The results show that these faults are explained by models 1 and 2, but not 3. An example of model 3 was not found because faults that initiate at the salt-sediment interface propagate faster than those that form within the sediment. Also, the geomechanical barrier around a stock with existing radial faults makes it difficult for a fault to intersect the stock. These faults can have either a large positive or a negative throw gradient at the salt-fault contact. Using root mean square seismic attribute maps, it can be shown that throw gradient is related to the brittleness or ductility of rocks. The

results show that ductile rocks can accommodate strain, whereas throw is more pronounced in brittle rocks at the salt-fault contact.

4.1 Introduction

Faults that connect adjacent salt structures are important because they serve as regional or counter-regional faults that can help interpret the history of a salt basin. These faults are usually large and can control the location of sediment depocenter (e.g., Carruthers et al., 2013; Tvedt et al., 2016), serve as migration paths for hydrocarbon between adjacent salt structures (e.g., Mattos and Alves, 2018) and from source rock to reservoir. Studies on the growth of diapiric structures (Vendeville and Jackson, 1992a, b), their stress perturbation (Heidari et al., 2017; Nikolinakou et al., 2014), and radial faults (Coleman et al., 2018; Stewart, 2006) focused on a single salt structure. However, we see faults that link neighboring salt structures, and it is unclear if radial faults evolve to form these faults and the faults mechanism of propagation.

Faults that connect salt structures are observed in subsurface geological studies (e.g., Schuster, 1995; Rowan et al., 1999; Carruthers et al., 2013; Tvedt et al., 2016). These faults often coincide with a salt ridge that serves as a base for salt stocks. (e.g., Tvedt et al., 2016). The large displacement on these faults suggests that they grow faster compared to faults formed within the sediment. Near the salt-fault contact, the faults can exhibit one of the two distinct throw gradients; throw may rapidly increase or decrease towards the salt stock (e.g., Mattos and Alves, 2018). These characteristic displacement patterns can be used to interpret the pattern of initiation and propagation.

Coleman et al. (2018) used two mechanisms, stem push and stretching of a

stock's overburden, to explain the formation of radial faults and their displacement

patterns. According to the authors, diapiric force at the flank of stock forms radial faults

with a maximum throw at the salt-fault interface. In contrast, radial faults formed on the

roof of a rising diapir and later shouldered aside have the throw maximum at a distance

from the salt-sediment contact. The stress at the stock flank can perturb faults formed by

the second mechanism and throw pattern readjusted to resemble those formed by the

stock flank. Despite their findings, the authors did not consider the effect of lateral

variation of lithology on the location of throw maximum on the radial faults.

This study proposes three hypothetical scenarios to explain the formation and

propagation of faults that connect two adjacent salt stocks (Fig. 4.1a). In the first, Model

1, two radial faults, F1 and F2, formed at different salt stocks A and B, respectively,

propagate towards each other; both faults eventually interact and link to form a single

fault. The displacement profile of this linked fault will show a high gradient and throw at

the salt-fault contact and a relatively low throw at the point of linkage. In model 2, a

radial fault, F3, from stock C propagates towards stock D. Although the adjoining stock

has radial faults, none propagate towards stock C. Fault F3 from the stock C eventually

intersects stock D. In this scenario, the throw is relatively high at the salt-fault contact at

stock C compared to stock D. Conceptual model 3 is different from 1 and 2, in that a fault

develops in between two salt stocks, relatively independent of any salt effects. As

sediment loading and salt evacuation continue, the fault tips propagate toward both stocks

and intersect them. In this model, the throw is expected to be maximum at the center of

the fault. Fault throw is maximum at the salt-fault contact for models 1 and 2. In all these

models, it is assumed that there is an unlimited salt supply, and the same salt source actively feeds the stocks during the formative stage of the fault.

The present study also examines the cause of increase and decrease in fault throw as it intersects a salt structure. I interpret the lithology change across faults around the salt-sediment interface using seismic attribute maps to interpret lithology and computing sand/shale ratio.

Using fault kinematic determined by displacement backstripping and patterns of throw distribution, these models are tested using data that covers six salt stocks, the Dog Lake, Four Isle, Bay Saint Elaine, Lake Pelto, Caillou Island, and Lake Barre in the northern Gulf of Mexico (Fig. 4.1b). This area is a good place to study the validity of these conceptual models because there are abundant 3D seismic data, well logs, and biostratigraphy data. Also, there are numerous salt stocks (Schuster, 1995; Weitz, 1987) with faults connecting them (Schuster, 1995; Weitz, 1987). Lastly, the Gulf of Mexico is a type basin to study salt tectonics and salt-fault interactions.

Figure 4.1. a. A conceptual image shows the growth of faults that connects two salt stocks. Model 1 shows two radial faults from two stocks intersects each other to form a single fault. Model 2 shows a single fault from a stock approaching and eventually intersects another salt stock. Model 3 shows a fault that initiates between two salt stocks, approaches both stocks, and eventually intersects them. b. The location map of the Terrebonne Salt withdrawal basin (broken black polygon) within the broader Gulf of Mexico basin. The study area is along the shoreline of Louisiana. Faults (linear lines) and salt structures (black polygon) are rampant in the basin. The Lake Barre-Leville (LB-L) ridge lies within the basin, whereas the Caillou Island-Bay Marchand salt ridge (CI-BM; elongated black polygon) represents the southern boundary of the TSWB. The northern boundary is marked by the Golden Meadon fault zone (GMFZ). Data for salt stocks are from Seismic Exchange Inc, whereas the Caillou-Bay Marchand salt structure is from Abriel and Haworth (2011). Culpepper et al. (2019) compiled faults for Louisiana Coastal Hazard Atlas from multiple sources.
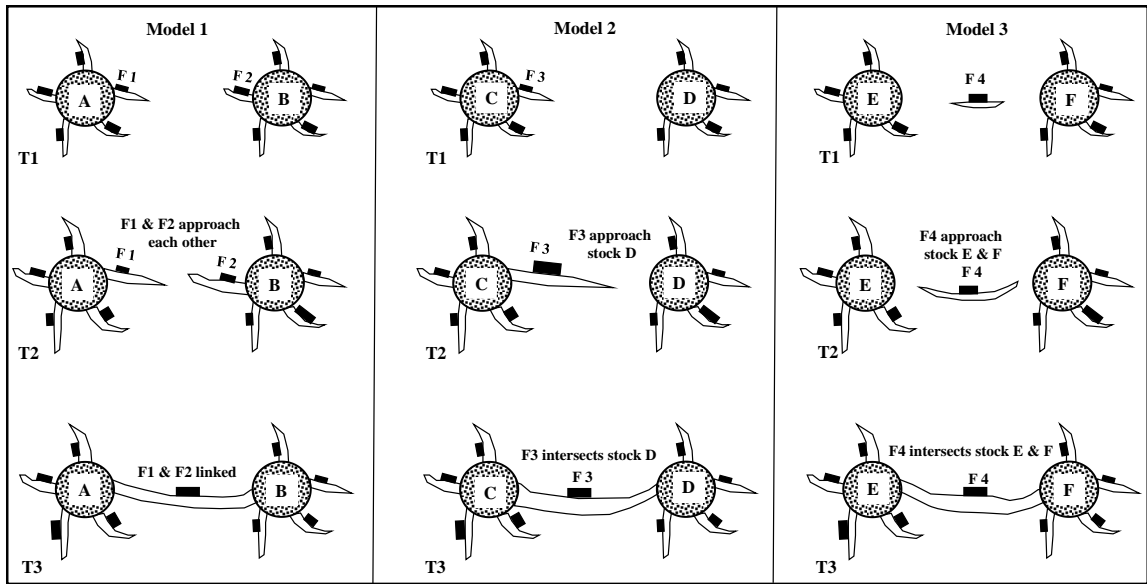
(a)
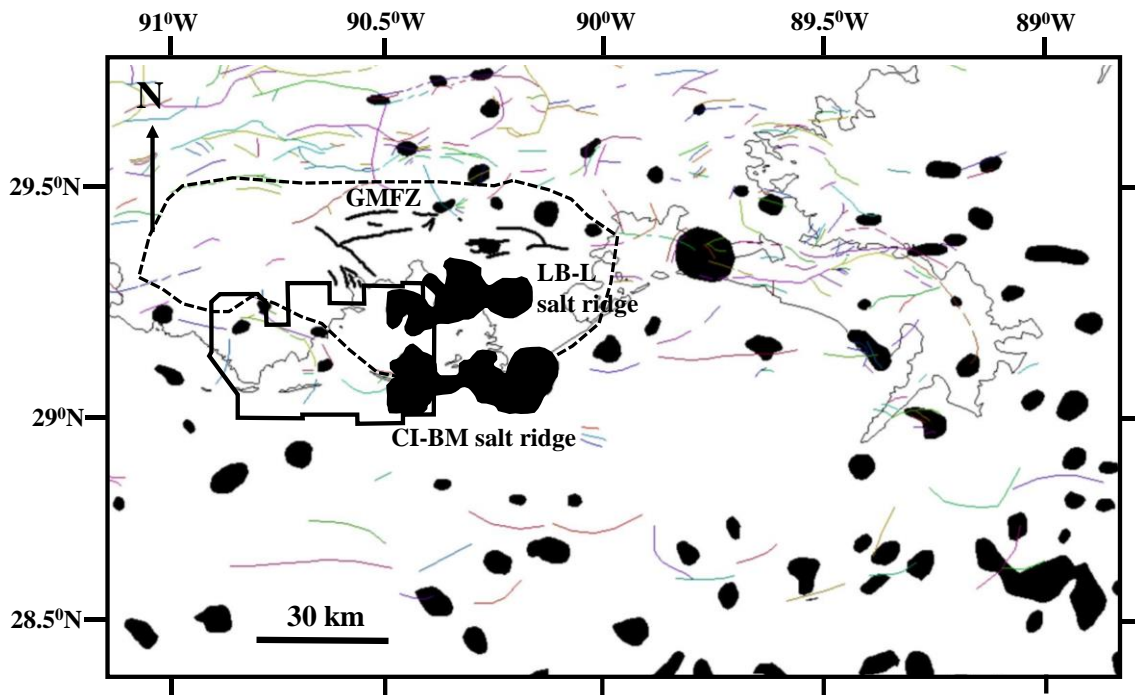
(b)

4.2. Geological Setting

The formation of the Gulf of Mexico is linked to the rifting of Pangea. This rifting, which took place during the middle Mesozoic, created the Gulf of Mexico (Buffler and Sawyer, 1985; Hudec et al., 2013). At the early stage of formation, the new basin was relatively small and contained super saline water, which favored the formation of the Jurassic Louann salt (Buffler and Sawyer, 1985). Precipitation of the Louann ceased because the rifted continents continue to move apart (Hudec et al., 2013), causing an influx of less saline water into the basin.

During this time, the autochthonous salt remains at the basin margins but was later expelled basinward, i.e., to the Terrebonne area, by prograding sediment. This expelled salt formed an Eocene allochthonous salt canopy (McBride, 1998; Peel et al., 1995) that was later covered by Late Eocene, sediment (McBride, 1998; Peel et al., 1995). High sediment flux during the Miocene led to the deformation of the salt canopy and salt expulsion (Frey and Grimes, 1970; McBride, 1998; Seni, 1992). The expelled salt formed stocks and ridges (Frey and Grimes, 1970; Ingram, 1991; McBride, 1998; Peel et al., 1995; Schuster, 1995; Seni, 1992), whereas the place previously occupied by the expelled salt now serves a basin, in this case, the Terrebonne Salt Withdrawal basin (Schuster, 1995).

The formation of faults and an increase in fault activity accompanied this new basin (McBride, 1998). One such fault, the Golden Meadow Fault Zone (GMFZ), is at the northern margin of the TSWB (Schuster, 1996; McBride 1998; Fig. 4.1b). In contrast, the southern boundary comprises of a counter-regional system that includes landward dipping faults (McBride, 1998; Schuster, 1995) and a salt ridge (Abriel and Haworth,

104

2011; Atwater and Forman, 1959; Frey and Grimes, 1970; Ingram, 1991; Rowan et al., 1999). The ridge connects the Bay Marchand, Timbalier, and Calliou Island stocks (Atwater and Forman, 1959; Ingram, 1991; Schuster, 1995; Steiner, 1976). Also, Lake Pelto, Bay St. Elaine, Four Isle (Vidrine, 1971; Weitz, 1987) are rooted in the same ridge with Caillou Island (Weitz, 1987). Dog Lake is on a ridge (Vodicka, 1987), but it is not clear if the ridge is the same as the Four Isle-Bay Marchand ridge. The Lake Barre is rooted in another ridge north of the Four Isle-Bay Marchand ridge (e.g., Abriel and Haworth, 2011).

By the Pliocene, the depocenter had moved to offshore Gulf of Mexico (Galloway, 2001). According to (McBride, 1998), the decrease in fault activity during this time suggests the amount of salt within the withdrawn basin is relatively small. In contrast, there was renew deposition within the basin during part of the Pleistocene (Coleman and Roberts, 1988b; Galloway, 2001) and Holocene (Coleman and Roberts, 1988b).

4.3. Data sources and Methodology

Oil industry data were used to interpret the strata geometry and salt structure. The data used are well logs, mainly raster logs, that comprise of Gamma-Ray (GR), Spontaneous Potential (SP), and resistivity logs were downloaded from the website of the Strategic Online Natural Resources Information System (SONRIS). These logs are very old, mostly acquired between 1950 and 1980. The logs were loaded into IHS Petra software and used primarily to correlate and map a Mid-Pleistocene shale that lies on the 2700 ft sand of Kolvoord et al. (2008) from the Golden Meadow area (located 25 km

northeast of study area) into the Terrebonne Bay survey. The Terrebonne Bay survey is a

1410 sq.km proprietary 3D seismic data, provided by Chevron USA, which is located in

Terrebonne parish Louisiana and lies along the coastline of Louisiana (Fig. 4.1b). The

data range from 0 secs, which is approximately sea level, to 5 secs TWTT, and it is a TTI

Kirchhoff sedonly depth migration data. The survey has a bin spacing of 24.15 m and

SEG normal polarity, i.e., an increase in acoustic impedance corresponds to a positive

polarity.

Fault architecture was defined by mapping, using IHS Kingdom software, of

faults on seismic profiles that are perpendicular to the fault strike using a sampling

interval of 10 lines. This mapping led to the interpretation of 250 faults. Horizon mapping

proceeds fault mapping with the mapping of 13 selected horizons (Fig. 4.2). Some of the

horizons are constrained by published age such as the 760 m shale, on top of the 2700 ft

sand, of Kolvoord et al. (2008). Some horizons were constrained by biodata provided by

Paleodata Inc, whereas the remaining horizons were mapped based on seismic reflector

strength and continuity. The selected horizons were spaced temporally to show variation

in strata structures and fault displacement.

The 13 horizons were grouped into four sub-groups based on geologic age (Fig.

4.2). The first group contains the top of the salt. Top salt is interpreted where continuous

reflectors that have a peak-trough-peak characteristic overlie reflectors that are chaotic,

discontinuous, and truncated (Jackson and Hudec, 2017). The salt weld, the evacuated

salt interval, was interpreted where the peak-trough-peak reflector sequence merges with

the trough-peak-trough reflector sequence. The second group, the Late Miocene, is made

up of horizons from the oldest *Cibicides Cartensi* (*Cib. C*), *Textularia L* (*Tex. L*),

Discorbis 12 (*Dis. 12*), *Amphistenia E* (*Amph. E*), *Biginerinia A* (*Big. A*) and *Robulus E* (*Rob. E*). The *Robulus E* horizon marks the Miocene-Pliocene Boundary. The third group, the Pliocene, is made up of 4 horizons, from the oldest M3, M2, M1, and *Lenticulina 1* (*Lenti. 1*). The *Lenticulina 1* horizon marks the Pliocene-Quaternary boundary. The fourth group, the Quaternary section, is made up of the Mid-Pleistocene 760 m shale and Z1.

The time data of each mapped horizon was used to generate a Time structure map. This time map was converted to subsea depth using velocity data from Velocity Databank Inc. The thickness between two successive depth structure maps was calculated, and the thickness data was used to generate an isopach map. Sources of error for this map may be due to thickness between two inclined strata leading to underestimation of the strata thickness. Displacement data were extracted from each structure map using Badley's Geoscience Traptester7 (T7) software. Displacement data were used to generate throw (T) versus distance (x) profile to interpret interaction with salt stocks (e.g., Tvedt et al., 2016; Coleman et al., 2018), fault interaction and linkage (e.g., Peacock and Sanderson 1991; Willemse et al., 1996; Gupta and Scholz 2000; Cowie and Robets 2001, Walsh et al., 2003). Also, the data was used to generate throw map to interpret fault growth, temporal and spatial fault throw variation (Baudon and Cartwright, 2008a; Childs et al., 2003), fault interaction and linkage(e.g., Childs et al., 2003; Baudon and Cartwright, 2008; Dutton and Trudgill, 2009).

Geologic Age	Stratal Unit	Index Fossil	Reflector mapped	Age (Ma)
Quaternary			Z1	?
	SU 10		760 m Shale	1.54
	SU 9			
		Lenticulina 1	Lenti.	2.39
	SU 8			
Pliocene			M1	?
	SU 7		M2	?
	SU 6			
			M3	?
	SU 5b			
		Robulus E	Rob. E	5.97
	SU 5a			
		Bigenerina A	Big. A	7.39
	SU 4			
Miocene		Amphistegina E	Amph. E	7.84
	SU 3			
		Discorbis 12	Dis. 12	9.18
	SU 2			
		Textularia L	Tex. L	9.71
	SU 1			
		Cibicides Cartensi	Cib. C	10.63
?		Louann Salt	Salt	?

Figure 4.2. Stratigraphy chart shows the 13 mapped horizons that define the 11 stratal units (SU) and their corresponding ages. The age of the Mid-Pleistocene shale is from Kolvoord et al. (2008), whereas that of the other horizons is from biostratigraphy data from PaleoData.

Displacement backstripping was performed using the maximum throw subtraction method (Dutton and Trudgill, 2009; Jackson et al., 2017; Rowan et al., 1998). This method was selected and used over the vertical throw subtraction method (Chapman and Meneilly, 1991; Childs et al., 1993) because faults that connect salt structure intersects

salt both at their tips and at depth. Therefore, these faults will concurrently propagate laterally and accumulate displacement.

4.4. Basin Architecture

4.4.1 Salt Structure

The salt structure is an east-west trending structure (Fig. 4.3a). The northern part of the structure is continuous compare to the southern region. This continuous portion serves as a base for salt stocks. Seven (7) structural highs were identified within the salt structure map, but six (6) of the structural highs correspond to salt stocks based on their shape, height, discontinuous, chaotic seismic reflectors characteristics within the stock, and published literature (Atwater and Forman, 1959; Vidrine, 1971; Vodicka, 1987; Weitz, 1987; Ingram, 1991; Abriel and Haworth, 2011; Fig. 4.3b).

Figure 4.3a. Structure map of Terrebonne Bay salt. The map shows the Dog Lake (DL), Four Isle (FL), Bay St. Elaine (BSE), Lake Pelto (LP), and Lake Barre (LB) stocks connected by a single salt ridge, whereas the Caillou Island (CI)stock appears isolated. b) A dip of maximum similarity attribute map at 2.55 secs. The faults, linear-curvilinear features, interact with the salt stocks, i.e., the black circular features. c) Seismic profile showing Dog Lake and Four Isle stocks (see Fig. 4.3b for location) d) Seismic profile showing Caillou Island stocks (see Fig. 4.3b for location) e) Seismic profile showing Lake Pelto (see Fig. 4.3b for location).

(a) Salt structure map

(b) Dip of maximum similarity map at 2.9 km (subsea)

(c) (d) (e)

110
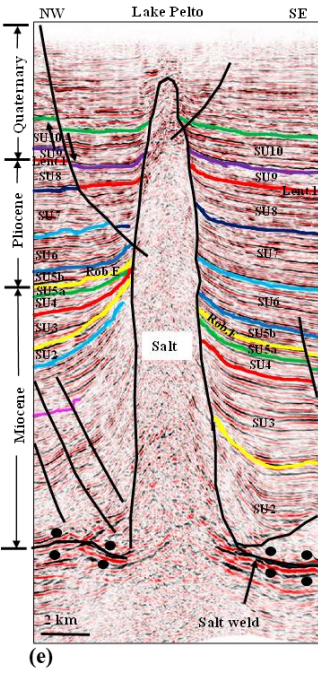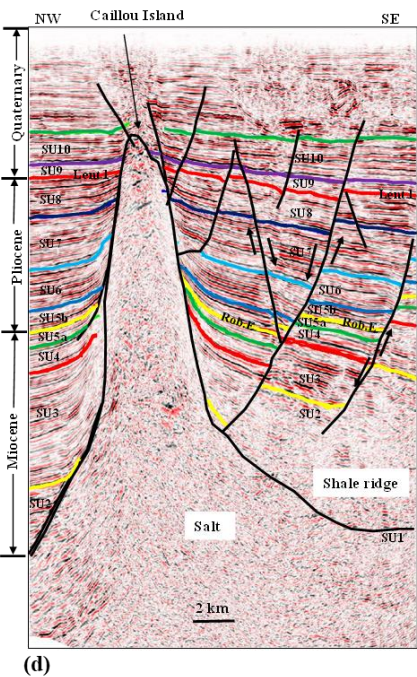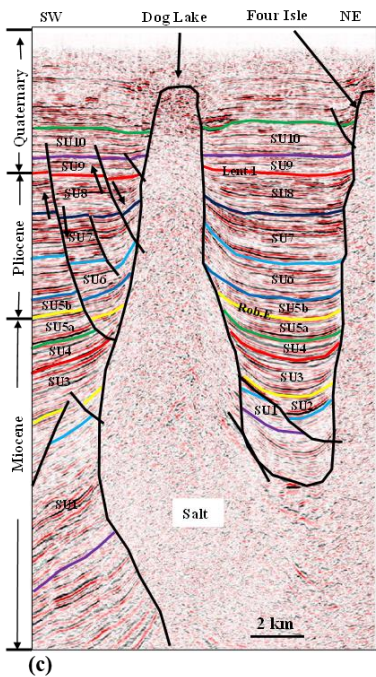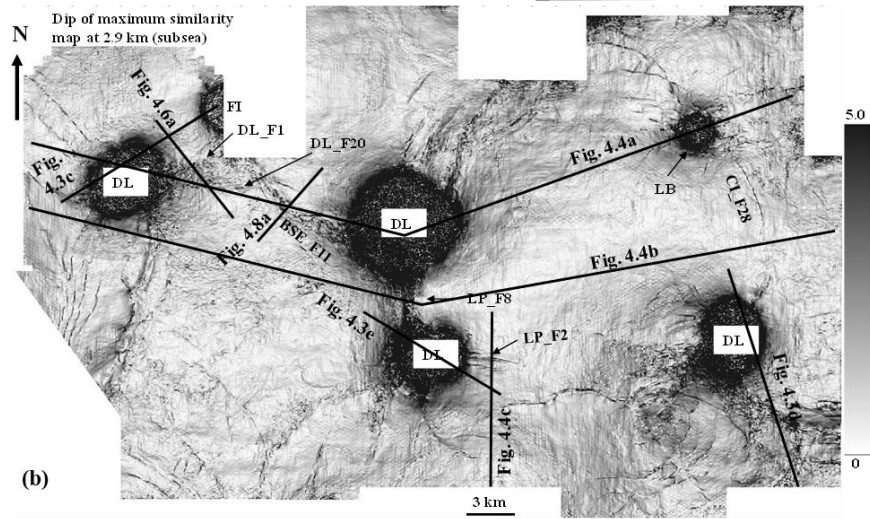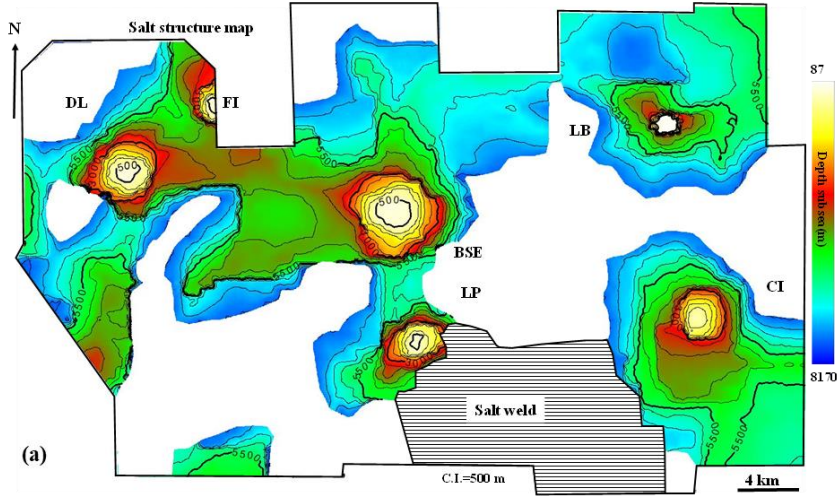
The first stock, Dog Lake, is a west-leaning vertical stock (Fig. 4.3c & 4.4a). The top of this stock is 300 m subsea. The next stock, the Four Isle, is partially contained within the survey (Fig. 4.3c). Its top is 340 m below sea level. Southeast of the Four Isle is the Bay St. Elaine stock (Fig. 4.4a). Its top is 320 m subsea. From Bay St. Elaine, the salt ridge extends eastward and southward (Fig. 4.3a). To the east is the Lake Barre stock (Fig. 4.4a). It top 87 m below sea level. South of Bay St. Elaine is the Lake Pelto stock (Fig. 4.3a, 4.3b & 4.3e). The top of this stock is 400 m below the sea level. The top of the Caillou Island is 600 m below sea level. Although this stock does not appear rooted in the same salt ridge as the other stocks, the presence of fault CI_F28 linking Caillou Island with Lake Barre (Fig. 4.3b & 4.4b) and east-west striking faults between Caillou Island and Lake Pelto (Fig. 4.3b) suggest that all these stocks were once connected.

The 7th structural high could not be interpreted in full because it lies at the edge of the survey, and there is a 7 km data gap between the Chevron's data and the next survey south of it. Based on the salt structure and the fault architecture south of Dog Lake stock (Fig. 4.3b & 4.4b), this high could be a small salt structure or an extension of the salt ridge that eventually connects the Coon Point salt stock (e.g., Ingram 1991).

The discontinuous part of the salt structure is in the southwest and east-central portions of the survey. The top of the salt could not be mapped because of the vertical extent, i.e., 5 seconds, of the seismic survey. However, towards the southern part of the east-central portion (Fig. 4.3a), i.e., southeast of Lake Pelto, there is a unique seismic characteristic. A strong peak-trough-peak reflector package is resting on a strong trough-peak-trough reflector package (Fig. 4.3e). Below these reflectors, the seismic reflectors are not discontinuous and chaotic. Instead, they are continuous with moderate amplitude.

This set of reflector sequence suggests the presence of a salt wedge and coincide with the location of salt weld within the Terrebonne Salt Withdrawal basin (Schuster, 1995). Furthermore, the east flank of the Lake Pelto stock appears not to sole or rest into an underlying salt ridge (Fig. 4.3e). Instead, it terminates into the weld reflector sequence. One of the faults that lies above the weld and radiates out of the Lake Pelto salt stock, LP_F2, has both normal and reverse sense of slip (Fig. 4.3b, 4.4c & d). The normal slip is observed from Z1 to *Amp.E*, whereas the reverse displacement is from *Dis.12* to *Tex.L* (Fig. 4.4c).

4.4.2 Shale Ridge

At the south flank of the Caillou Island stock, a low amplitude semi-continuous set of reflectors rests on the discontinuous chaotic reflectors (Fig. 4.3d). These reflectors anomaly is an east-west trending structure south of Caillou Island stock. Spontaneous Potential and Gamma-Ray logs of well within this portion of the survey show that these discontinuous reflectors are predominantly shale. Based on the well logs, the seismic characteristics, and published papers on the Caillou Island (Atwater and Forman, 1959; Freeman, 1965; Frey and Grimes, 1970), these reflectors anomaly is a shale ridge. This shale ridge extends eastward towards the Timbalier Bay stock (Freeman, 1965; Frey and Grimes, 1970), and the presence of diapiric shale on the south flank of Bay Marchand (Abriel and Haworth, 2011; Frey and Grimes, 1970) suggests that the shale ridge extends towards the later. The shale ridge area is structurally complex (e.g., Murray 1966; Frey and Grimes, 1970), with the east-west striking faults and the northwest-southeast striking faults intersecting each other (Fig. 4.3b and 4.3d). These faults sole into the ridge and truncate the Miocene and Pliocene sediment that overly the ridge.

112

4.4.3 Sediment Distribution Pattern

The strata sequence shows a general eastward increase in strata thickness (Fig. 4.4a & 4.4b). Strata unit 1 (SU 1) did not cover the entire survey because of its base, *Cib.C*. The *Cib.C* horizon is not continuous west of the Bay St. Elaine-Lake Pelto stocks (e.g., Vodicka, 1987). This area is characterized by abrupt truncation of reflectors and inclined reflectors inside it. This sequence of reflectors suggests an erosional surface (e.g., Vodicka, 1987) that indicates channel activities. An example of such a channel is on the footwall of BSE_F1 (Fig. 4.8a). Channels transversing the area at the beginning of the Late Miocene eroded previously deposited *Cib.C* horizon (Fig. 4.5a). East of this Bay St. Elaine-Lake Pelto stocks, *Cib.C* could not be mapped in the bottom half of the area because of the vertical extent of the seismic survey, i.e., 5 secs (5920 m).

Figure 4.4a. East-West seismic profile showing sediment distribution from Dog Lake, Bay St. Elaine, and Lake Barre stocks (see Fig. 4.3b for location). b) East-West seismic profile showing sediment distribution pattern. Strata thicken across LP_F8 (see Fig. 4.3b for location) c) Seismic profile and d) throw map of LP_F2 (see Fig. 4.3b for location). The fault radiates out of the Lake Pelto stock and lies above a salt weld. The fault has a normal displacement from Z1 to *Big.A* and reverse displacement from *Amph.E* to *Tex.L.* The throw maps show similar throw pattern. The positive contour lines suggest normal throw, whereas negative contour lines at the bottom of the map indicate a reverse throw.

113

(a)

(b)

(c)

(d)
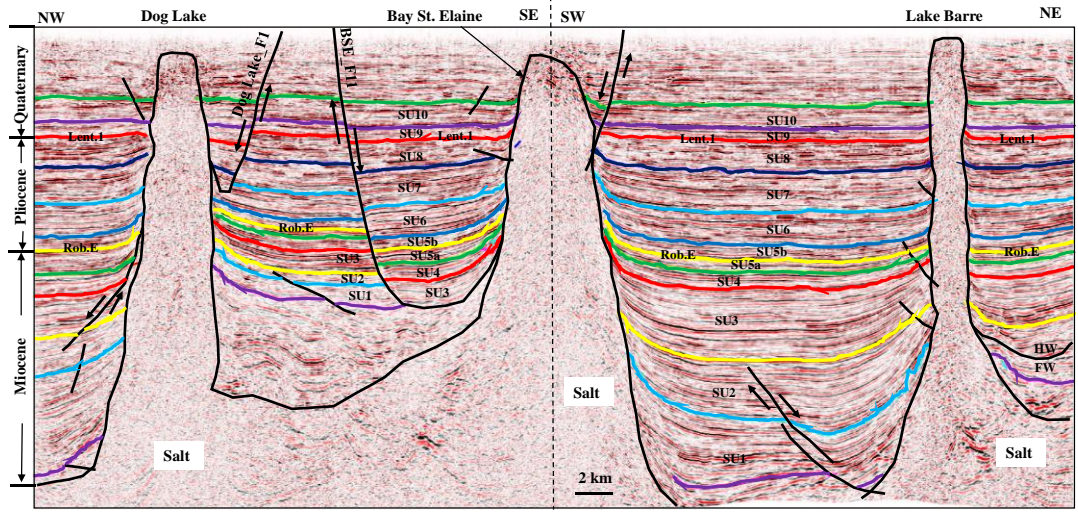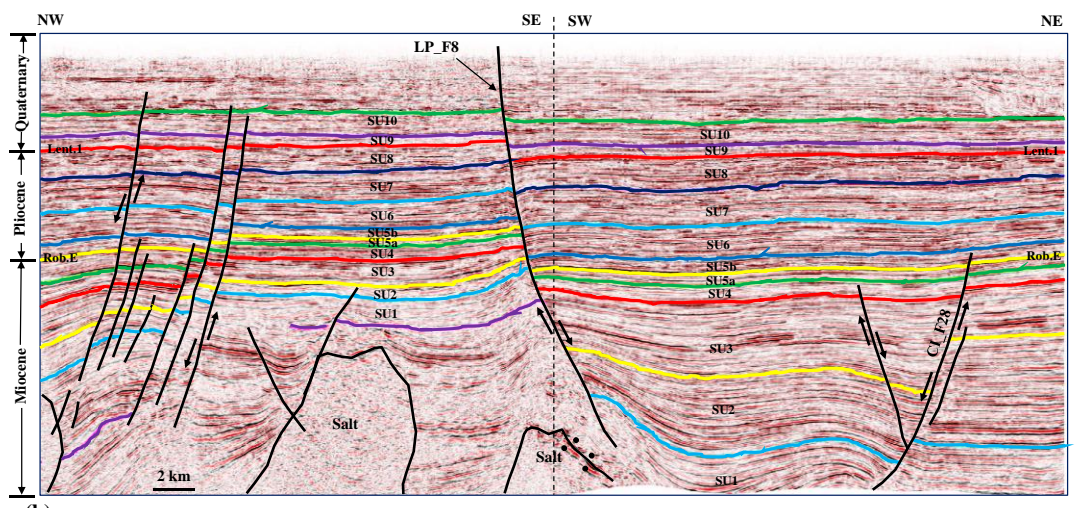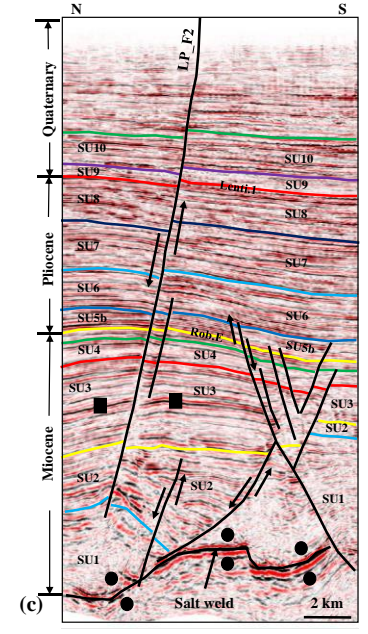
Where mapped, *Cib.C* and *Tex.L* were both used to generate an isopach map for SU1 (Fig. 4.5a). This map shows that the highest strata thickness is in the northwest and north-central portion of the survey. The BSE_F11 fault shows evidence of thickening across fault from 400 m on the footwall to 1000 m on the hanging wall. Strata continue to thicken across BSE_F11 during SU2 (Fig. 4.5b). During this period, the locus of deposition was on the east side of the survey, with the strata thickness reaching 2750 m. The strata thins westward acr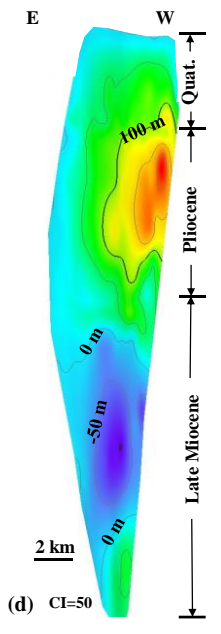oss the CI_F28 before the depocenter makes a south turn/bend and starts thickening towards the south. The southwest block defined by Dog Lake-Four Isle-Bay St. Elaine-Lake Pelto received minimal deposition at this time.

Minimum deposition continues to define the southwest block during the SU3 (Fig. 4.5c), whereas strata began thickening across CI_F28, LP_F8, and BSE_F11. By SU4 (Fig. 4.5d), the deposition was not only concentrated between LP_F8 and CI_F28, but also north of Bay St. Elaine stock, north and southwest of Dog Lake stock and southwest of Lake Pelto stock. Faults connecting these salt stocks show considerable thicken of strata across them. By SU5a (Fig. 4.5e), the depocenter had shifted to the northwest corner of the survey around Dog Lake and Four Isle salt stocks. Little or no across fault thickening is recorded on CI_F28 and LP_F8. Also, the east-west striking faults on the west flank of Lake Barre stock begun to retreat.

The beginning of the Pliocene, SU5b, is marked by relatively high deposition in the southwest of Dog Lake stock and between LP_F8 and CI_F28 (Fig. 4.5f). Although strata thickening is high between these two faults, LP_F8 shows considerably thickening across it, thus it continued growing. In contrast, CI_F28 shows very little across fault thickening; therefore, the fault starts to retreat southward. The east-west fault that

115

characterized the west flank of Lake Barre stock and its associated radial faults continue retreat towards the stock. Faults retreat continues into SU6 (Fig. 4.5g). By this time, CI_F28 had retreated south towards CI stock, whereas LP_F8 continues to grow during SU7 (Fig. 4.5h). In comparison to the Late Miocene strata, SU1 to SU5a, the population of faults during the Pliocene drastically decreased. By the end of the Pliocene, SU8, high deposition is concentrated towards the south flank of Lake Pelto stock. The faults that connect stocks, BSE_F11, DL_F1, and LP_F8 continue to grow (Fig. 4.5i).

At the beginning of the Quaternary, SU9, the locus of deposition is south of Lake Pelto and around Dog Lake-Four Isle stocks (Fig. 4.5j). The DL-F1, BSE_F11, and LP_F8 continued to grow. These faults grew until SU10 (Fig. 4.5k).

4.5. Kinematics of faults connecting salt stocks

There are several faults in this study area that interacts and intersects salt stocks. This study focuses on faults that connect two adjacent salt stocks. Therefore, kinematic analyses were conducted for DL_F1, BSE_F11, FI_F1, LP_F8, and CI_F28.
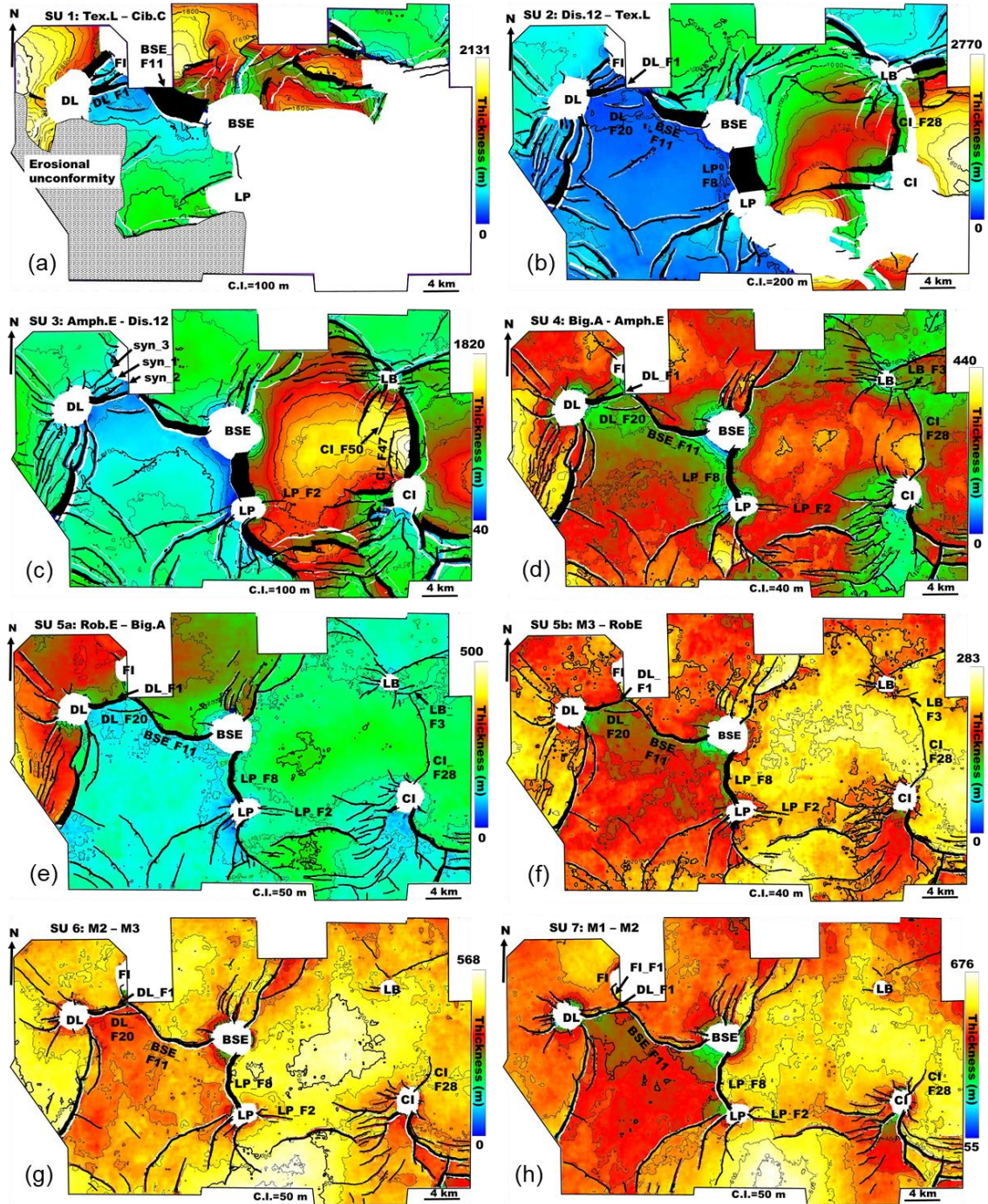
Figure 4.5. Isopach map show sediment distribution and accumulation for each stratal unit (SU). Sediment loading during the Late Miocene is shown in (a) SU 1 (b) for SU 2 (c) for SU 3 (d) for SU 4 (e) for SU 5a. Pliocene sediment loading is defined by (f) for SU 5b (g) for SU 6 (h) for SU 7 (I) for SU 8, whereas (j) for SU 9 and (k) for SU 10 defined sediment dispersal and fault growth during the Quaternary.

117
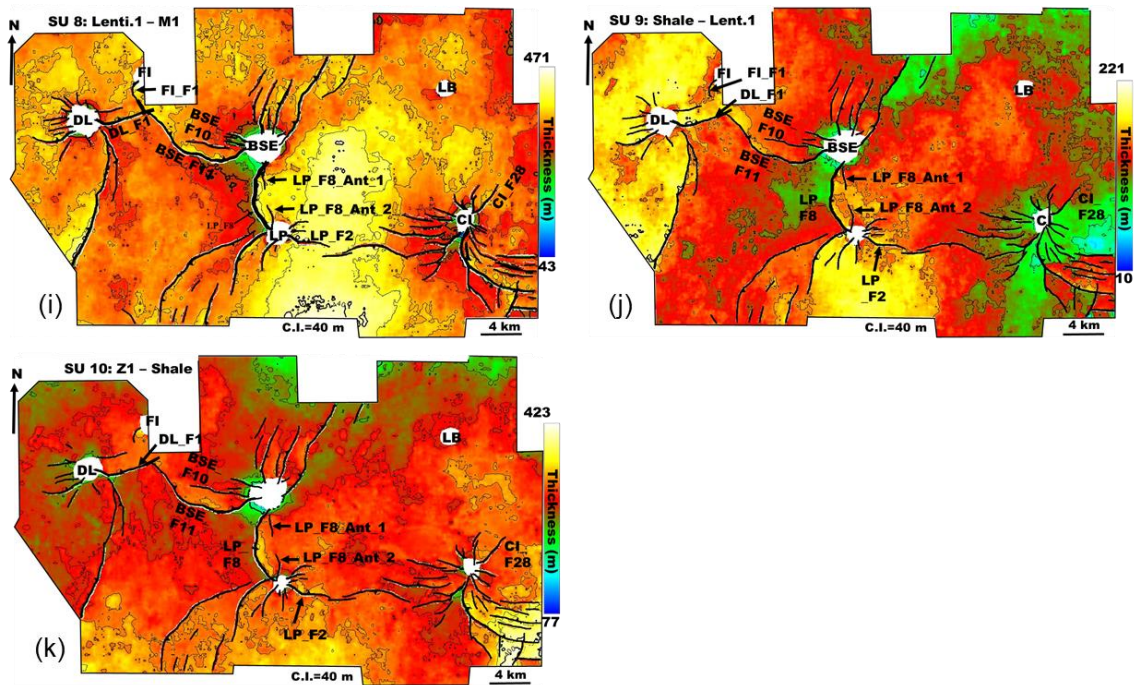
(Figure 4.5 cont'd)

4.5.1 DL_F1

The Dog Lake_F1 (DL_F1) is a 6.5 km long northeast-southwest striking fault (Fig. 4.3b & 4.5), dips northward, and a maximum cumulative throw of 1100 m (Fig. 4.6a, 4.6b & 4.6c). In older literature, this fault is referred to as F-Theta (Vodicka, 1987). On the southwest end, the fault intersects the east flank of Dog Lake stock (e.g., Vodicka 1987; Fig. 4.3b; Fig. 4.4a; Fig. 4.5), whereas, towards its northeast tip, it is intersected by FI_F1 (Fig. 4.5i & 4.5h) and the Bay St. Elaine_F11 (BSE_F11). The upper tip extends to the top of the seismic data, whereas the bottom tip sole into the salt ridge (Fig. 4.4a & 4.6a). The DL_F1 is associated with three synthetic faults (Fig. 4.5) Two of these synthetic faults, DL_F1_syn_1 and DL_F1_syn_3, directly intersect both Dog Lake and

Four Isle salt stocks, whereas the third fault, DL_F1_syn_2, intersects both DL_F1 and

Four Isle stock.

The throw-distance plot of DL_F1 is asymmetrical in shape with the highest

throw for each horizon located at the southwest tip, where it intersects the Dog Lake

stock (Fig. 4.6c). The throw decreases from the salt-fault interphase at Dog Lake towards

the northeast, where FI_F11 and BSE_F11 intersect the fault. At the intersection point

with BSE_F11, there is an abrupt decrease in throw, whereas the reduction in throw

where FI_F1 intersects it is relatively small. Temporally, throw increase from the

youngest Z1 horizon to the deepest *Cib.C* horizon. However, the throw profile for *Big.A*,

Amph.E, *Dis.12*, *Tex.L,* and *Cib.C* cross each other between 0.5 km and 3.5 km. This is

due to the presence of three synthetic faults, DL_F1_syn_1, DL_F1_syn_2, and

DL_F1_syn_3, that were active throughout the Late Miocene. The distribution of throw

across multiple closely spaced faults is a characteristic feature of kinematic and

geometric coherent faults (Childs et al., 1995; Walsh et al., 2003; Walsh and Watterson,

1991).

 Figure 4.6a. Seismic profile across DL_F1 (see Fig. 4.3b for location). Both the b)
Throw map (V.E. = 4) and c) T-x plot shows an asymmetrical profile. Throw decrease
from the fault-salt interphase at Dog Lake stock towards the northeast, where BSE_F11
and FI_F1 intersect it. d) 3D fault plane map shows a continuous increase in throw until
the fault-salt interphase. The hangingwall (HW) and footwall (FW) cutoffs are for the top
of *Dis.12.*
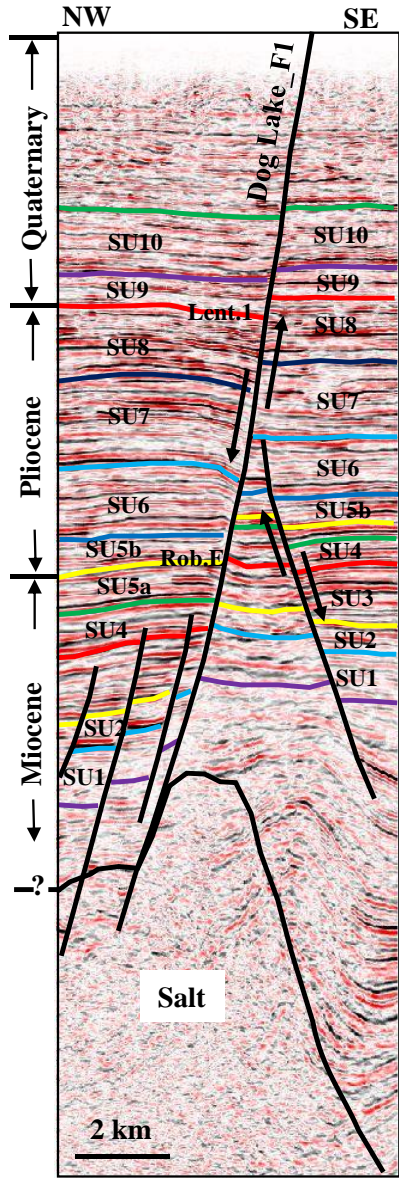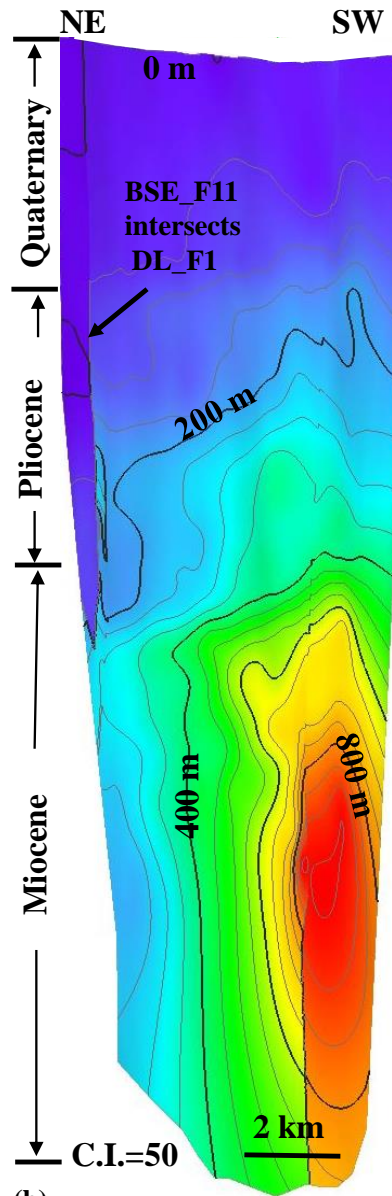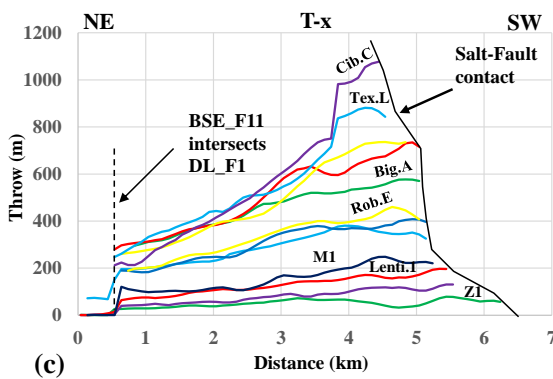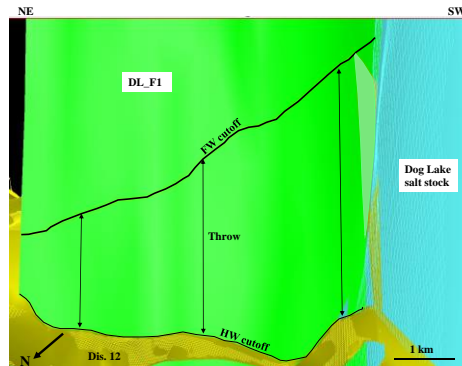
The throw map of DL_F1 shows similar throw distribution and characteristics like its throw-distance profile (Fig. 4.6b). The contour lines are sub-horizontal between 0 and 400 m with an associated decrease in contour spacing, suggesting syn-depositional activity and increasing fault throw, respectively (e.g., Childs et al., 2003). About 500 m towards the northeast tip, there is a change in contour pattern from sub-horizontal to sub-vertical. This contour change coincides with the intersection of BSE_F11 with DL_F1. Northeast of the 400 m contour, the contour lines are vertical to sub-vertical, and contour values decrease to the northeast tip. Southwest of the 400 m contour, the throw increase to over 800 m at the salt-fault interphase. There is an abrupt change in contour values across the vertical 800 m contour line. This area of the sudden increase in fault throw coincides with the location where one of the synthetic faults, DL_F1_syn_2, intersects DL_F1.

The displacement profile of DL_F1 was backstripped from SU10 to SU1 (Fig. 4.7). The backstrip plot of SU10 to SU8 did not show fault tip retreat on the older Miocene and Pliocene horizons (Fig. 4.7a-7c). However, after restoring to SU7, the northeast tip began to retreat. By SU6, the entire northeast tip had receded y at least 1.2 km (Fig. 4.7e). This retreat of the fault northwest tip continues until the deposition of SU1 (Fig. 4.7f-4.7k). The overall backstrip profile indicates that the fault grew rapidly in length and displacement from SU1 to SU7. By the deposition of SU8, the fault had reached its final length and only continue to accumulate displacement.
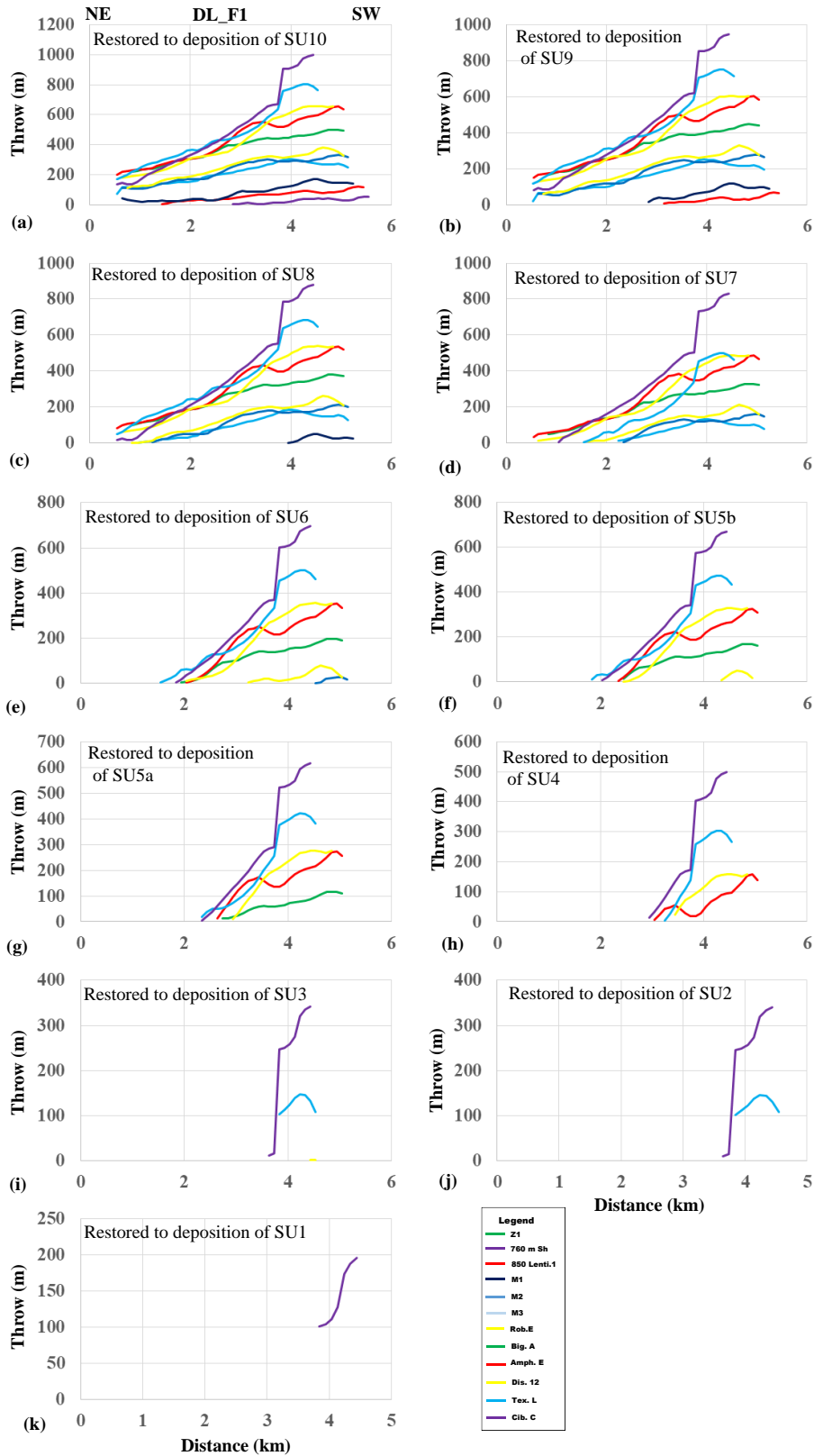
Figure 4.7. Bacstripped displacement plot for Dog Lake_F1

122

4.5.2 BSE_F11

The Bay St. Elaine (BSE_F11) is a 12.6 km long northwest-southeast striking fault, and it dips northward (Fig. 4.3b, 4.4a, 4.5 & 4.8a). The fault intersects the DL_F1 at its northwest tip and intersects the BSE stock at its southeast tip (Fig. 4.5). In old literature, this fault is the same as F-4 (Schneider, 1959) and Fault Theta (Weitz, 1987). The fault has a calculated maximum throw of 2650 m. At deeper depth, i.e., the *Big.A* to *Tex.L*, a synthetic fault interacts with it at its northwest portion whereas at a shallower depth (Fig. 4.5b-4.5f), Z1 to M2, an antithetic fault interacts with it (Fig. 4.5h-4.5k).

The throw-distance profile of BSE_F11 is also asymmetrical in shape (Fig. 4.8c). The maximum throw on each horizon is at the southeast end of the fault, i.e., where BSE_F11 intersects the Bay St. Elaine stock. The throw is maximum at the salt-fault interphase for all the horizons except M1, where throw rapidly decreases about 500 m towards the salt stock. About 1.5 km to the northwest fault tip, fault throw starts increasing. This increase is due to its intersection with DL_F1 in conjunction with a sudden rise in throw on *Dis.12* at 9.5 km. The location coincides with where a synthetic fault intersects BSE_F11. Temporally, throw gradually increases from Z1 to *Amph.E.*, whereas from *Dis.12* to *Cib.C*, there is a rapid increase in the throw.

The throw map shows a general increase in throw with depth (Fig. 4.8b). At the top-half portion of the map, the contour pattern is horizontal to sub-horizontal, suggesting syn-sedimentary activities (e.g., Childs et al., 2003). Also, the contour lines tilt towards the northwest. This contour pattern indicates that throw is higher on the southeast portion of the fault. From the 400 m contour downward, the contours show evidence of abrupt change in pattern from sub-horizontal to sub-vertical at two different locations. These

123

correspond to the location of fault intersection with the synthetic fault. These intersections led to a deficit in throw between the two intersection lines.

The throw was backstripped from the deposition of SU10 to SU1 (Fig. 4.9). After backstripping from SU10 to SU7 (Fig. 4.9a-4.9d), the shale to the M3 horizon profile retreated towards the Bay St. Elaine. Restoration from SU6 to SU4 shows little retreat at the northwest tip. However, the northwest tip began to retreat from SU3 to SU1 (Fig. 4.9i-4.9k) towards the Bay St. Elaine stock. This backstrip pattern suggests that the fault accumulated displacement and laterally propagated until it intersects the DL_F1 at the end of the Pliocene SU8. Further propagation of the BSE_F1 was restricted by the DL_F1 fault.
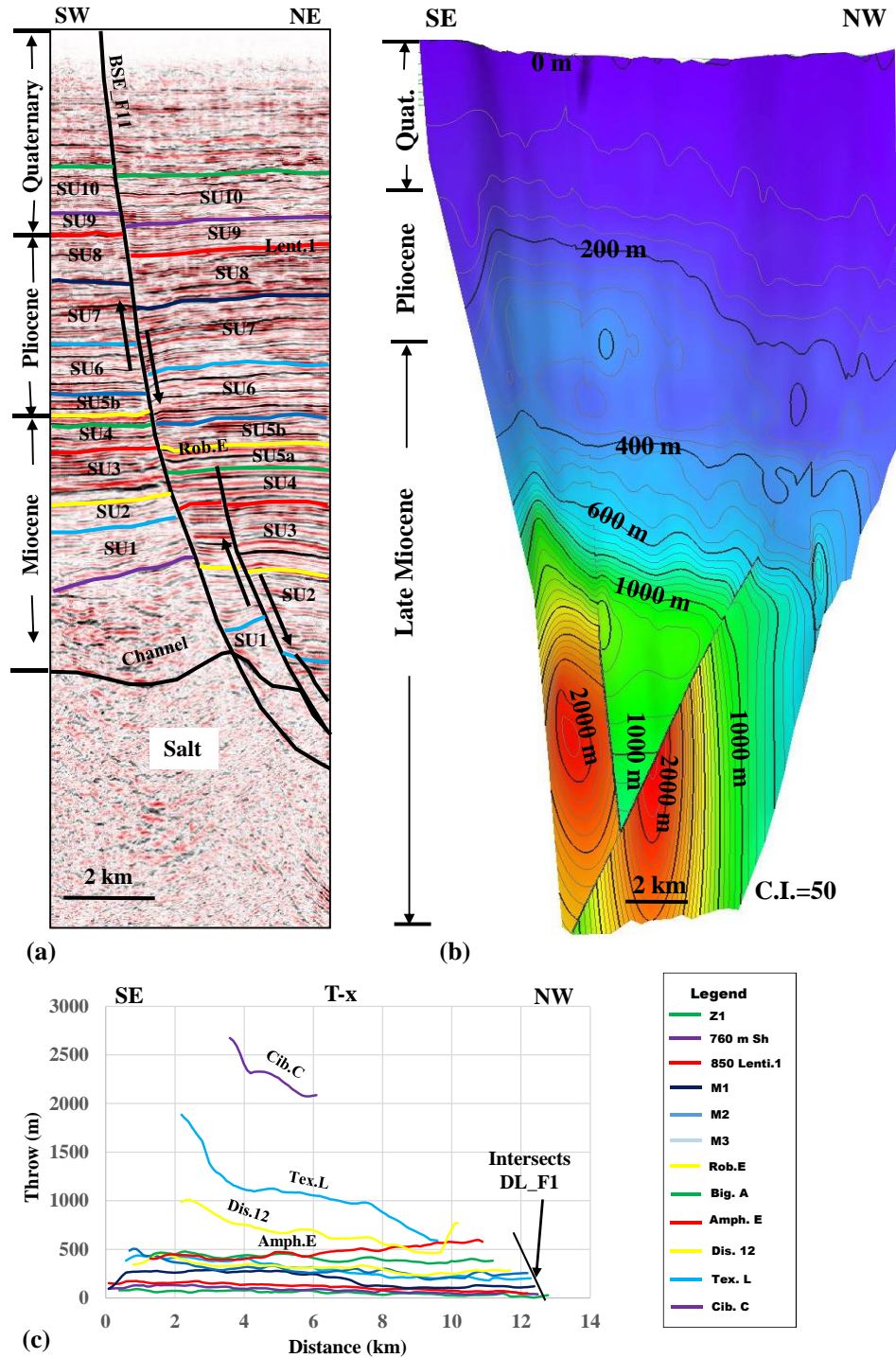
Figure 4.8a. Seismic profile across BSE_F11 (see Fig. 4.3b for location). Both the b) Throw map (V.E. = 4) and c) T-x plot of BSE_Fll shows an asymmetrical profile. Throw decrease from the fault-salt interphase at Bay St. Elaine stock towards the northwest where the fault intersects DL_F1.
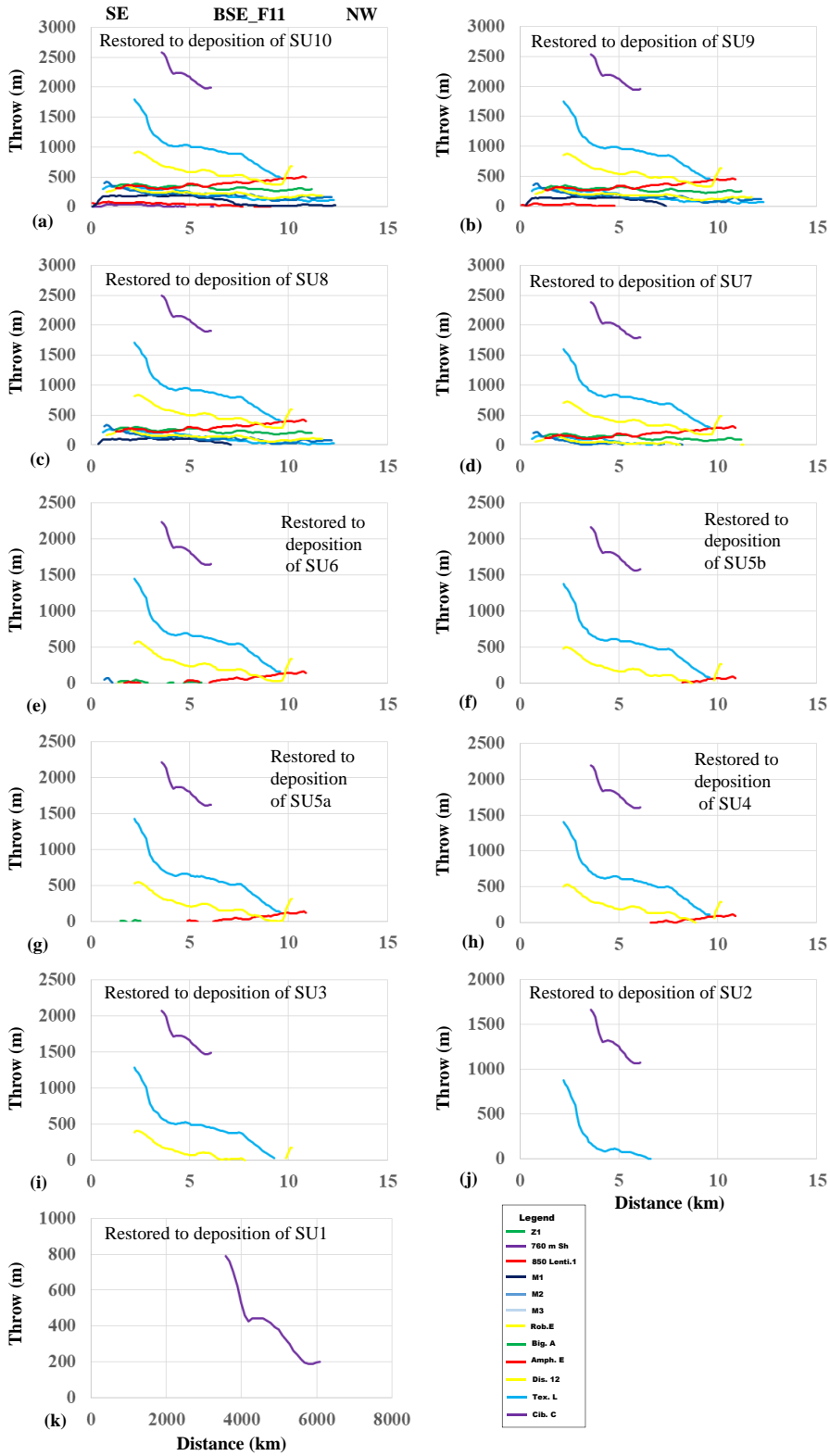
Figure 4.9. Bacstripped displacement plot for BSE_F11

126

4.5.3 FI_F1

The Four Isle_F1 (FI_F1) is an east-dipping fault that radiates out of the Four Isle stock, and it is partly contained within the 3D seismic data (Fig. 4.5g-4.5k). The fault is 4 km in length and strikes north-south. Its south tip intersects DL_F1 from M1 to older horizons (Fig. 4.10) and its throw decrease towards the southern tip. Throw backstripping shows a reduction in throw at the northern portion compare to the southern portion (Fig. 4.11). Also, after backstripping from SU10 to SU7, the southern tip of the fault receeded to the north. This pattern suggests that at each time interval, the fault accumulated more throw at the fault-contact and therefore propagated from the Four Isle stock. It is not clear when the fault intersection the DL_F1 fault.
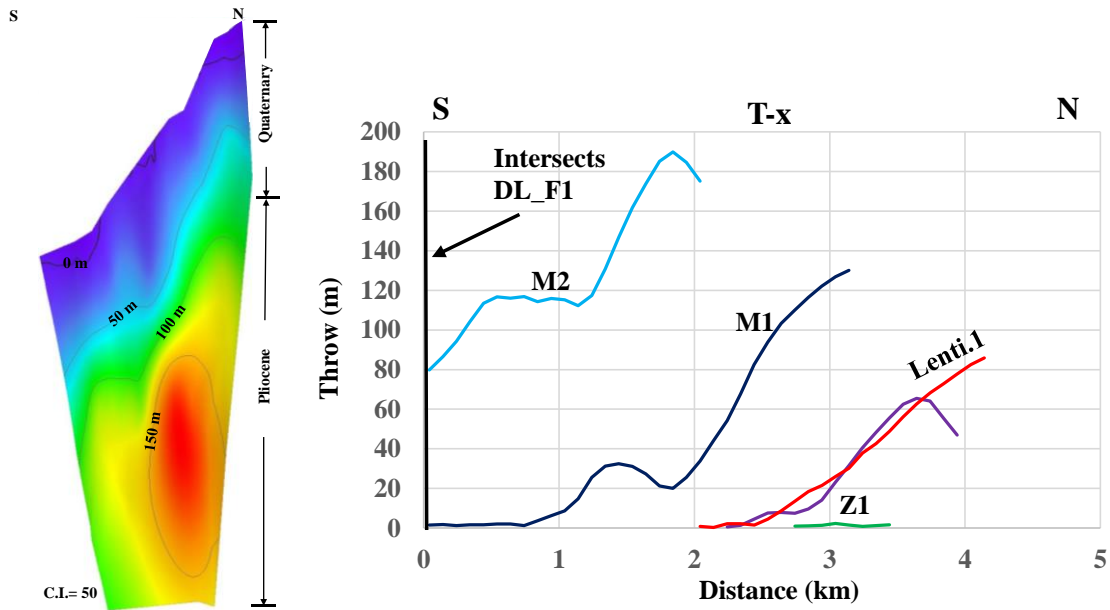
Figure 4.10a. Throw map (V.E. = 4) and b) T-x plot of FI_F1
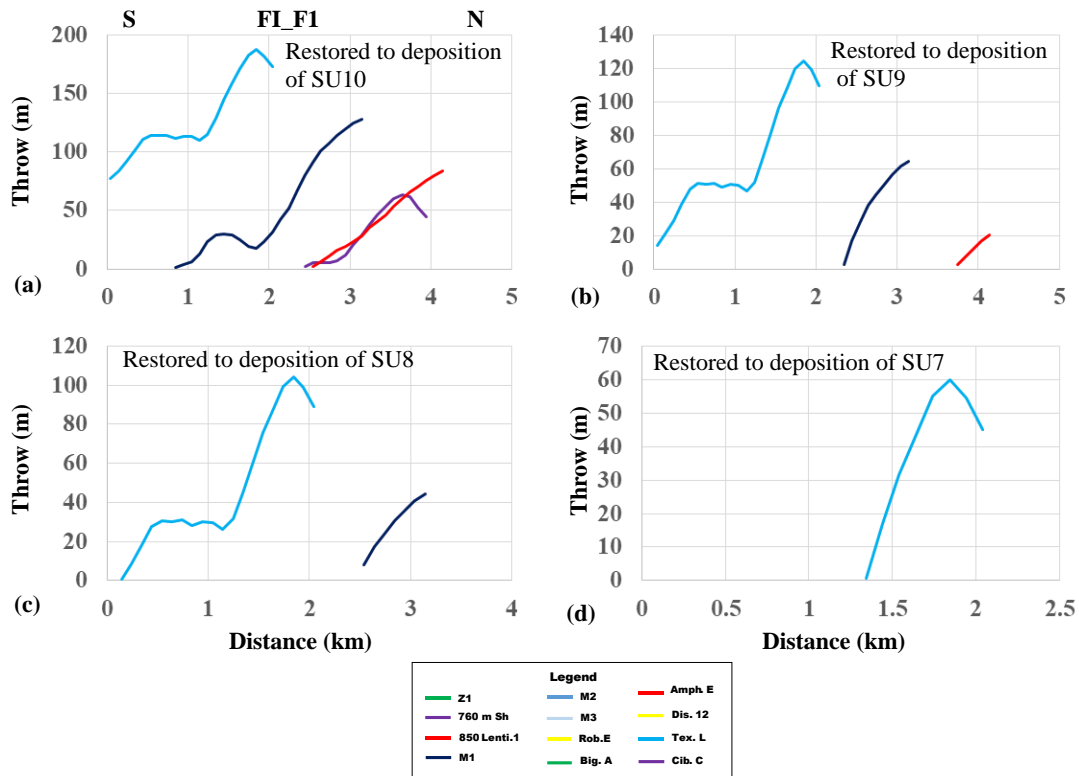
Figure 4.11. Backstripped displacement plot for FI_F1

4.5.4 LP_F8

The Lake Pelto_F8 (LP_F8), a west-dipping fault, is an 8.2 km long north-south

striking curvilinear fault with a maximum calculated throw of approximately 2900 m

(Figs. 4.3b, 4.4b, 4.5, 4.12). In older literature, this fault is the same as F-3 (Schneider,

1959) and Fault Epsilon (Weitz, 1987). At its northern tip, the fault intersects the Bay St.

Elaine stock (e.g., Schneider, 1959; Weitz, 1987), whereas its southern tips intersect the

Lake Pelto stock (e.g., Fails, 1965). Two radial faults, LP_F8_Ant_1 and LP_F8_Ant_2,

that intersect Bay St. Elaine, and Lake Pelto respectively, are antithetic to LP_F8 (Fig.

4.5i-4.5k). Both faults truncate strata from Late Pliocene (SU8) to Quaternary (SU10).
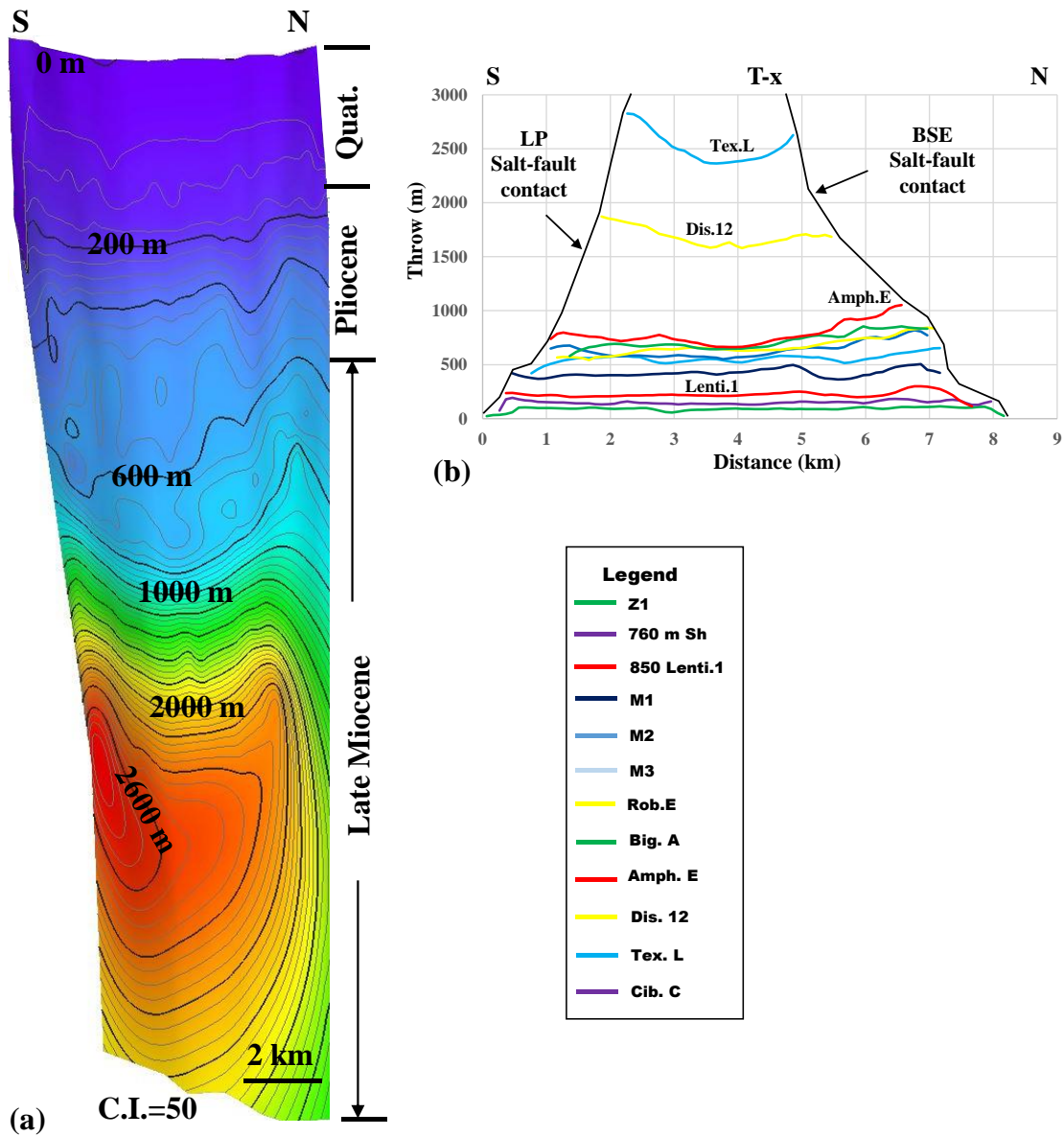
Figure 4.12a. Throw map of LP_F8 shows sub-horizontal contours at the upper map portion, whereas the lines are concave up at the lower part (V.E. = 4). b) T-x plot of LP_F8 shows concave down profile from Z1 to M2 and concave up profile from M3 to *Tex.L*. Both the map and plot show two throw maximal at each end of the fault.

The throw-distance plot of LP_F8 is unique and different from those of DL_F1 and BSE_F11. Its profile is asymmetrical in shape (Fig. 4.12b). Unlike the throw profile of the two former faults that are generally concave down and show a decrease in throw

from one fault tip to another, LP_F8 has a hybrid of a concave down and concave up profiles. From Z1 to M2, the throw profile is concave down. However, by M3, the throw-distance plot starts bending upwards. The upward concavity increases rapidly towards the profile of *Tex.L*. Secondly, for the concave down profile, i.e., Z1 to M2, the maximum throw is located at the north tip of the fault, and the minimum throw is at the south tip. In comparison, the concave up profile has two throw maximal—one at the north tip and the other at the south tip. The throw minimal is approximately at the fault center.

The throw map shows a distinct distribution of contour lines and characteristics (Fig. 4.12a). From 0 m to 600 m, the contour lines are horizontal to sub-horizontal, suggesting syn-depositional (e.g., Childs et al., 2003). From 800 m downward, the contour lines are relatively closely spaced, parallel, and characterized by upward concavities. This pattern of contours indicates that the throw is higher on both fault ends compare to the fault center. The northern end also shows a change in fault pattern from sub-horizontal to sub-vertical, suggesting that the fault throw slightly decreases before the salt-fault interphase at Bay St. Elaine. In contrast, the throw at the Lake Pelto salt-fault interphase is relatively high.

Throw backstripping shows no change in the concave upward pattern after backstrip to the deposition of SU7 (Fig. 4.13a-4.13d). By SU6, the fault had broken down into two segments; a northern and southern segments. These segments are illustrated by the profiles of M3, *Rob.E,* and *Big.A* (Fig. 4.13e). The throw maximum on each segment is at the fault-salt intercept with Bay St. Elaine and Lake Pelto respectively. Restoration from SU5b to SU4 only show the northern segment (Fig. 4.13f-4.13h).
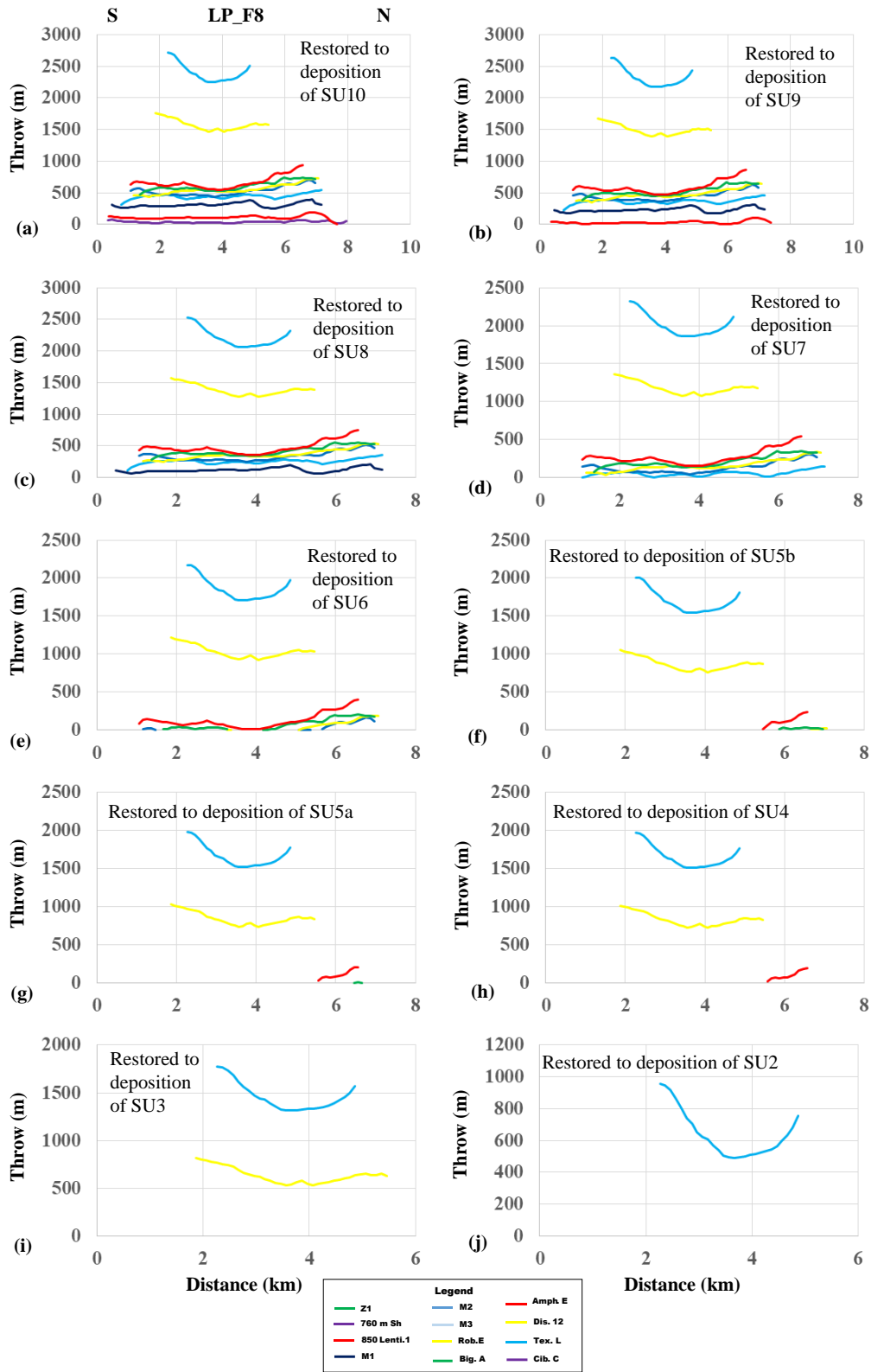
Figure 4.13. Backstripped displacement plot for LP_8

After backstripping to the SU2, the profile of *Tex.L* still shows a concave upward pattern (Fig. 4.13j). This concave upward profile suggests that the fault was formed by two isolated faults that later linked to create a single continuous fault. The location of the throw maxima at both fault tips and the throw minimal at the fault center confirms that the fault formed by linkage (e.g., Peacock and Sanderson, 1991; Willemse et al., 1996). The switch from concave upward to concave downward signifies the moment the fault accumulated enough displacement at its center. Thus, the displacement profile is adjusted to resemble that of a single continuous fault (e.g., Willemse et al., 1996; Gupta and Schilz, 2000).

4.5.5 CI_F28

The Caillou Island_F28 (CI_F28) fault, a west-dipping fault (e.g., Frey and Grimes, 1970), is a 13 km long, north-south striking, curvilinear fault (e.g., Abriel and Haworth, 2011; Fig. 4.3b; Fig. 4.4; Fig. 4.5). Its southern tip intersects the Caillou Island stock (e.g., Frey and Grimes, 1970; Abriel and Howorth 2011), whereas its northern tip intersects the Lake Barre stock (e.g., Abriel and Haworth 2011) at a deeper depth (SU2 – SU3). From SU4 to SU5a, the fault intersects east-west striking LB_F3 (Fig. 5d-5e). At shallow depth (SU5b – SU10), the fault retreats laterally towards the Caillou Island stock (Fig. 4.5f-4.5k). North-south and northeast-southwest striking faults truncate strata on the hanging wall of LP_F8. Two of these faults, CI_F47 and CI_F50, strikes towards each other (Fig. 4.5b-4.5e). In contrast to the antithetic faults associated with LP_F8, these faults have opposite dips and different strikes.
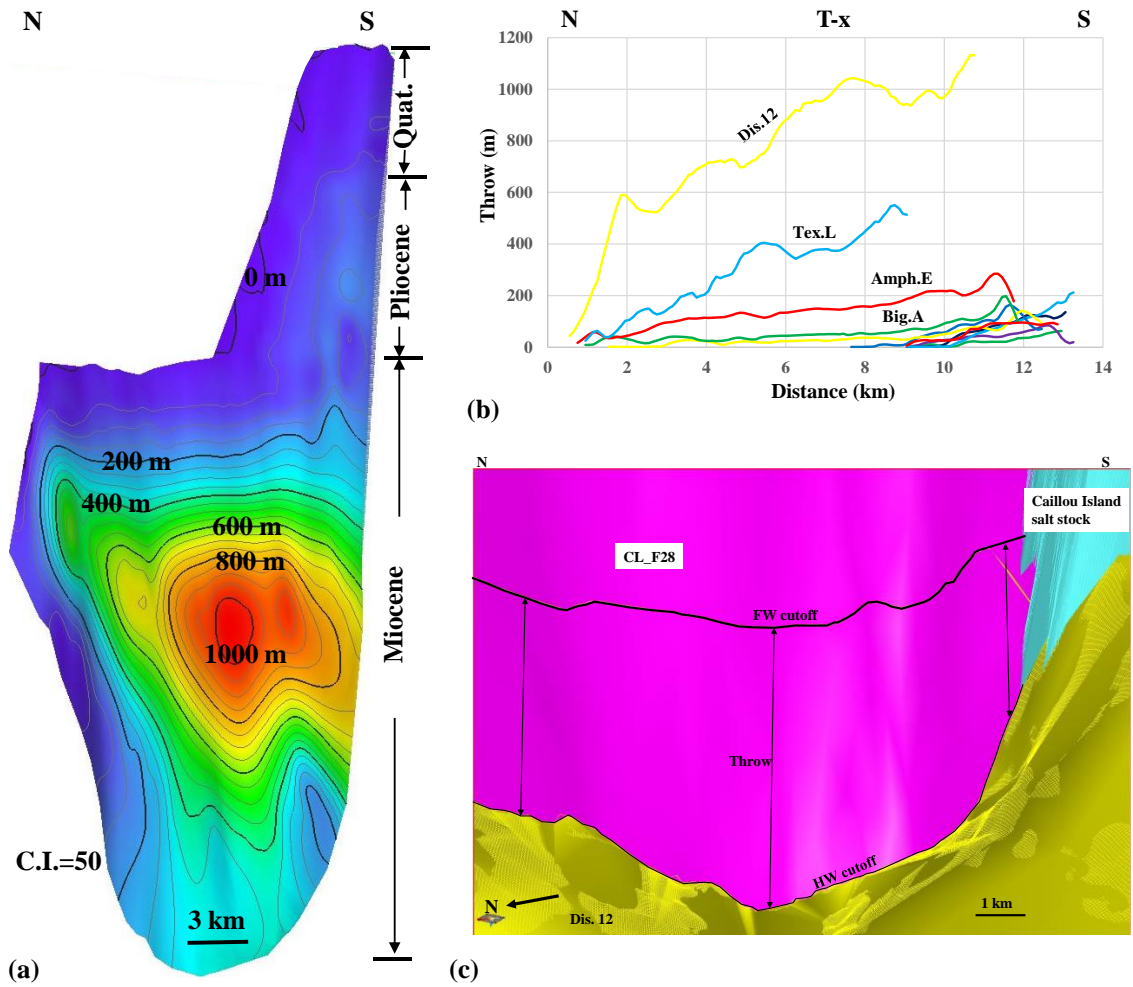
Figure 4.14a. Throw map of CI_F28 shows two throw maximal—the first at the upper portion and the second at the lower part of the map (V.E. = 4). b) T-x plot of CI_F28 shows an asymmetric displacement throw. Also, the throw on specific horizons decreases rapidly about 1 km before the fault intersects the Caillou Island stock. c) 3D fault plane map of CI_F28 showing high throw gradient and rapid decrease in throw within the vicinity of the Caillou Island stock. The hangingwall (HW) and footwall (FW) cutoffs are for the top of *Dis.12*.

The throw-distance profile of CI_F28 is asymmetrical in shape and throw on each profile increases southwards (Fig. 4.14b). The throw profile of *Dis.12* shows a very high displacement gradient at the north end compares to other horizons. This gradient is due to its intersection with the flank of Lake Barre. The fault gradient on *Lenti.1*, M1, and M2

continue to increase southwards until the fault intersects the Caillou Island stock. On the

contrary, on the remaining horizons, i.e., 760 m shale, M3, *Big.A*, *Amph.E*, *Dis.12*, and

Tex.L throw began to drop rapidly about 0.5 km to 1 km before the fault intersects the

stock (Fig. 4.14b & 4.14c). Thus, the maximum throw is not at the salt-fault interphase

(e.g., Mattos and Alves, 2018; Coleman et al., 2018).

The throw map generally shows horizontal to sub-horizontal contours suggesting

syn-depositional fault activity (e.g., Childs et al., 2003). The throw map is not a simple

elliptical or rectangular shape map. Instead, its shape resembles that of a shovel. The

southern portion of the fault intersects the earth's surface, whereas the northern part did

not. At the south part of the fault, the top of the map shows vertical to sub-vertical

contour lines with a throw maximal of 175 m. A second throw maximal is in the middle

part of the map and about 3 km from the salt-fault contact. Both throw maximal are

separated by a throw minimal, and this pattern suggests fault's growth through

superimposition and dip linkage (e.g., Mansfield and Cartwright 1996; Morley et al.,

2007; Tvedt et al., 2013). The contour lines, from the map's middle to bottom portion, are

horizontal to sub-horizontal, and their spacing decrease downwards. This contour pattern

suggests syn-depositional and increasing fault activity, respectively.

The displacement profile of CI_F28 was successively backstripped from the

youngest SU10 to the SU3 (Fig. 4.15). The backstrip plot of SU10 to SU8 shows the

retreat, on Shale to *Big.A* profile towards the north fault tip (Fig. 4.15a-4.15c). After

restoration to the deposition of SU7, the north tip, as shown on the *Amph.E* and *Tex.L*

profile, began to recede towards Caillou Island (Fig. 4.15d). This retreat continues until

the deposition of SU3 (Fig. 4.15e-4.15i). Throughout the backstripping process, the
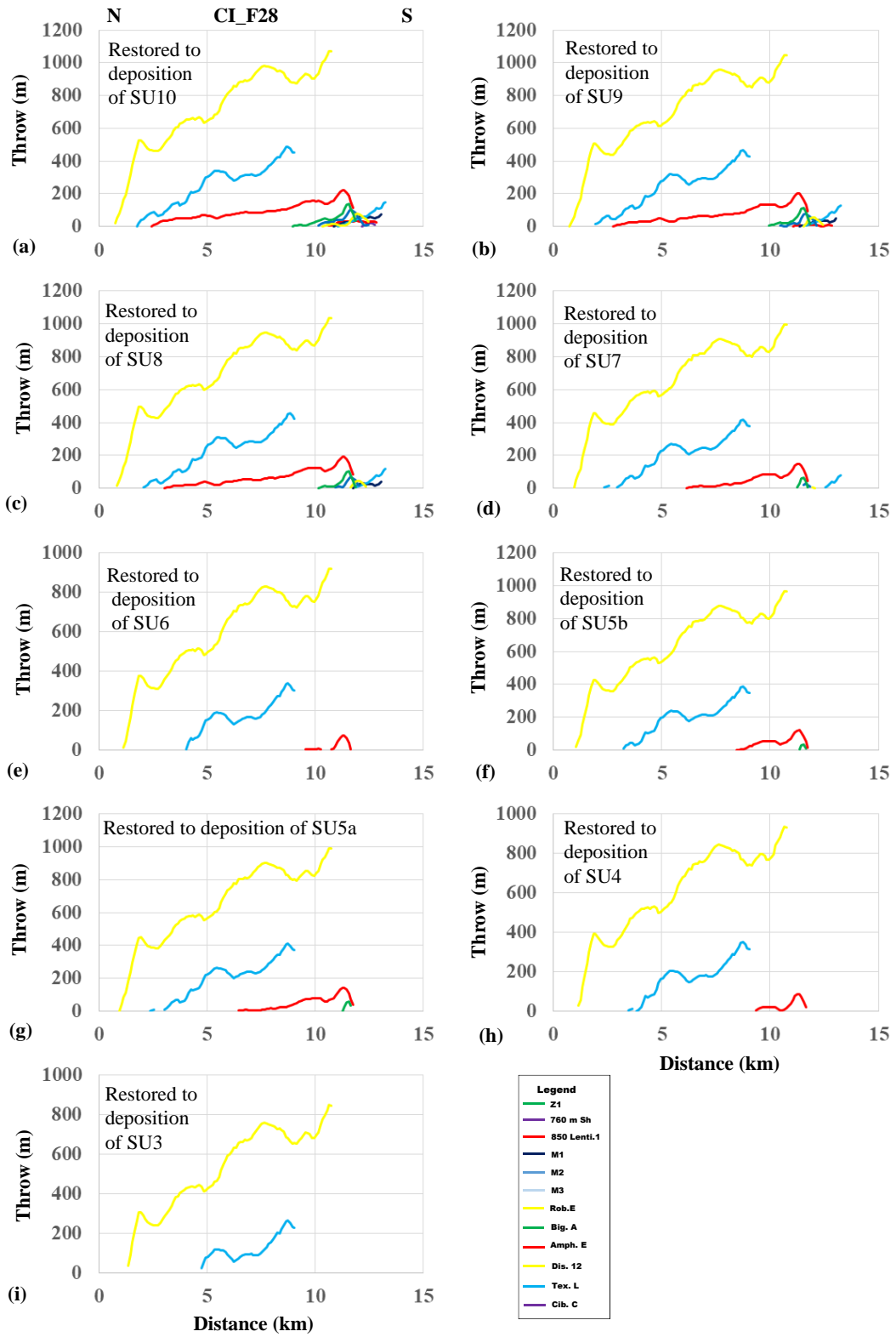
Figure 4.15. Backstripped displacement plot for CI_F28

Dis.12 profile only shows a decrease in the throw. There was no evidence of lateral fault retreat. The lateral retreat on other horizons suggests that the fault propagated from Caillou Island to Lake Barre stock.

4.5.6 Relationship between fault gradient and lithology at fault-salt contact

Faults that intersect and connect adjacent salt stocks show two unique throw patterns within 1.5 km of intersecting a stock structure. The throw either continues to increase towards the fault-salt interphase (Fig. 4.6c & 4.6d), or it decreases rapidly towards it (Fig. 4.14b & 4.14c). This throw gradient anomaly was examined by comparing it to the lithology within 1.5 km around the salt stock. The lithology was interpreted using Gamma Ray and Spontaneous Potential logs from wells close to the fault-salt contact. The thickness of sand and shale were computed from the top of each horizon to 100 m below it. The total thickness of sand was divided by the total shale thickness to calculate the sand/shale ratio (Table 1). This ratio is plotted against the throw gradient (Fig. 4.16) computed within 1.5 km of the salt-fault contact.

The plot for all faults (Fig. 4.16a) shows a negative correlation between gradient and sand-shale ratio, i.e., an increase in gradient corresponds to a decrease in sand/shale ratio. On the plot, increasing gradient towards a stock is represented by blue dots, whereas black dots represent decrease in throw towards a stock. It is observed that the data are not evenly distributed around the fitted line and a majority of the data points cluster below the fitted line. This clustered data have a gradient that ranges from 0 to 0.2 and sand/shale ratio between 0 and 1.2.

Table 4.1. Fault gradient and sand/shale ratio of DL_F1, BSE_F11, LP_F8, and CI_F28

	DL_F1		BSE_F11		LP_F8 north		LP_F8 south		CI_F28	
	Gradient	sd/sh ratio	Gradient	sd/sh ratio	Gradient	sd/sh ratio	Gradient	sd/sh ratio	Gradient	sd/sh ratio
Z1			0.00394	2.75						
Shale	0.0127	1	0.0122	0.071	0.00726	0.071			-0.144	0.111
Lenti	0.0326	0.875	0.0189	0.2	-0.552	0.304			0.0025	2
M1	0.096		-0.139	1.14	0.0148	2.75	0.0101	1.14	0.0569	1.5
M2	-0.0455	2	0.0178	3.14	0.0913	2.75	-0.188	0.57	0.0822	1
M3	0.0373	4	0.0991	4	0.111	1	0.139	2.75	-0.14	0.429
RobE	0.08	0.76	-0.145	0.76	0.0355	0.5			-0.103	1
BigA	0.0539	0.66	0.00988	0.5	0.0624	0.5	-0.165	0.76	-0.33	1.5
AmphE	0.128	2	0.0308	0.765	0.197	0.5	0.07	0.304	-0.34	2
Dis12	0.195	0.304	0.185	0.25	0.131	1	0.175	0.2	-0.418	0.5
Tex.L	0.11	0.033	0.599	0.0111	0.421	0.304	0.417	0.304		
Cib.C	0.162		0.667							
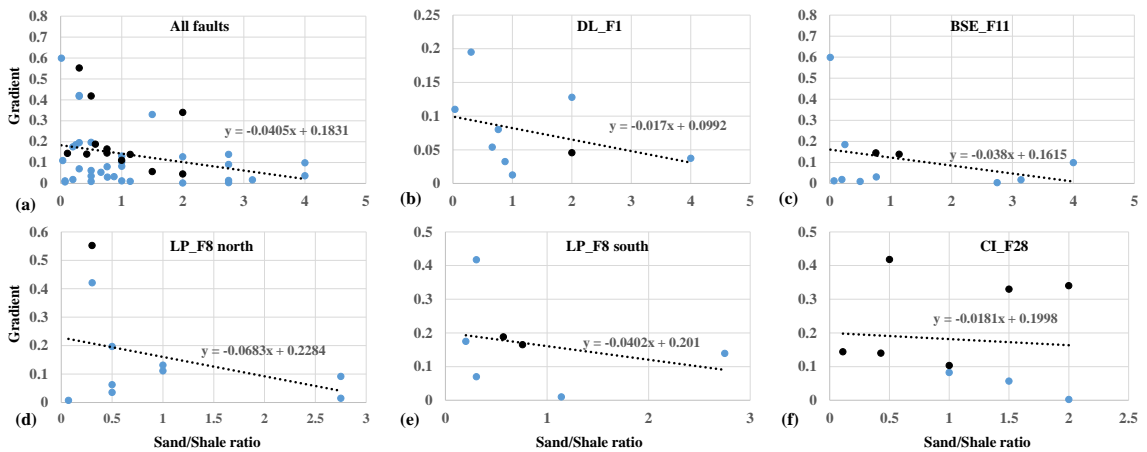
Figure 4.16. A plot of throw gradient against sand/shale ratio for a) all the fault, b) DL_F1, c) BSE_F11, d) LP_F8 north, e) LP_F8 south and f) CI_F28

The data are separated into each corresponding fault for better comparison between the gradient and sand/shale ratio. The plot for each fault also shows a negative correlation between throw gradient and sand/shale ratio (Fig. 4.16b-4.16f). The slope of the best-fit line is steeper for BSE_F11, LP_F8 north, and LP_F8 south compared to DL_F1 and CI_F28. Despite the similarity in the slope of the DL_F1 and CI_F28, they

137

are different in the way they interact with the salt stock. On most horizons except M2, throw on DL_F1 continues to increase towards the Dog Lake stock. Fault throw for CI_F28 increase towards Caillou Island stock during *Lenti.1*, M1, and M2. On the remaining horizons, the fault shows a decrease in throw and a high gradient towards the Caillou Island stock.

The variation in the sand/shale ratio with depth (Table 1) suggests change in the depositional environments i.e., from terrestrial to marine environment. This environment can also change laterally due to the pattern of sediment dispersal. The spatial and temporal variations in the environment mean that the sand/shale ratio from the well data may not fully represent the change in lithology. Therefore, 3D seismic volume was used to compute a seismic attribute in this case, root mean square (rms). A root mean square (rms) map suggests variation in grain sizes. Areas with high value (bright color) suggest coarse grain sediment, whereas areas with low value (cold color) suggest fine-grain sediment. The attribute was calculated for each strata unit. The top and base of each strata unit define the sampling window. This interval was used so as to compute the average grain size for each point, easily compare the attribute map with thickness variation as interpreted from the isopach map, and throw pattern for the top and base of each strata unit.
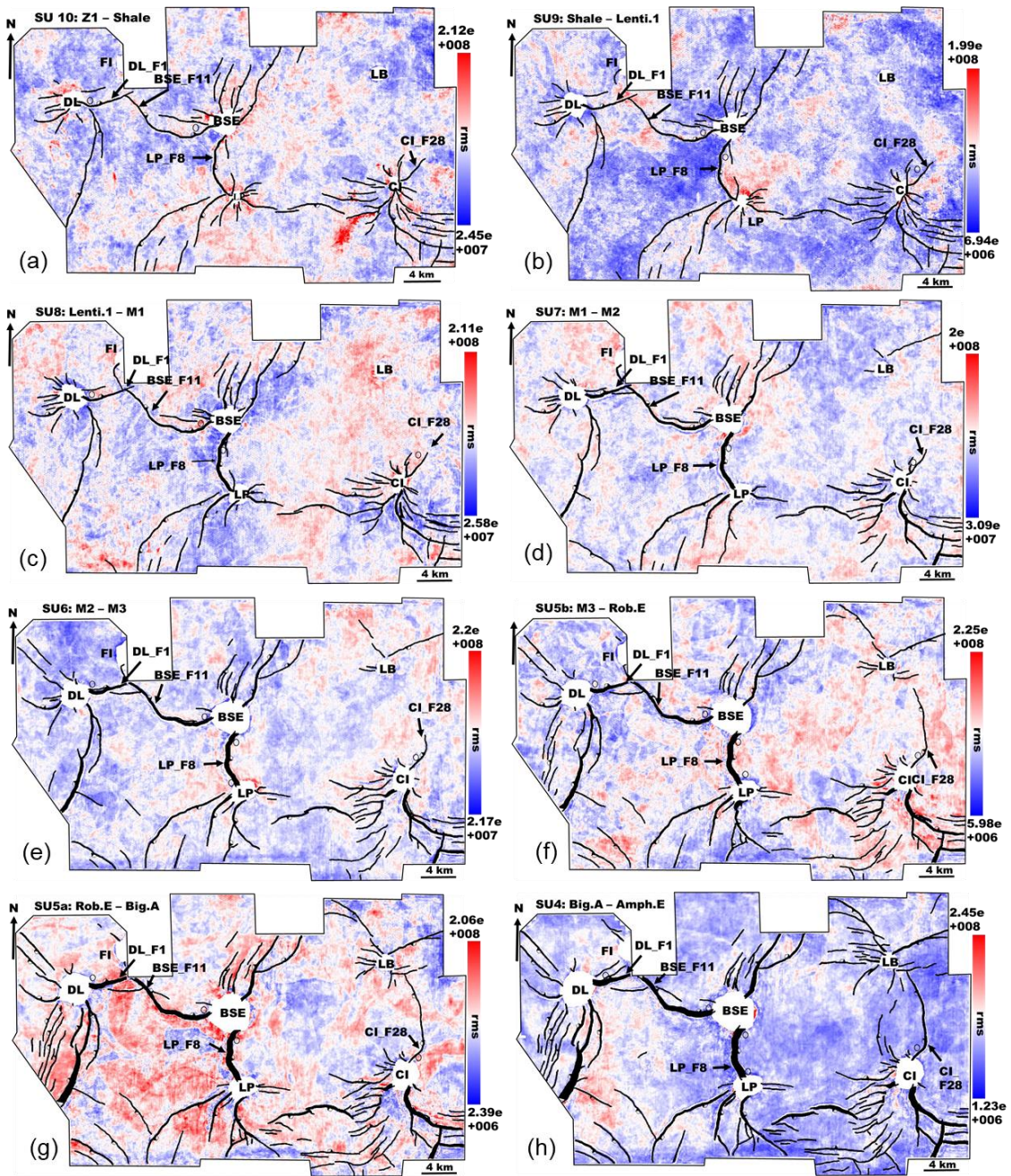
Figure 4.17. Root mean square (rms) seismic attribute maps showing a variation on grain sizes along fault traces. Black circles represent the location of wells used to compute the sand/shale ratio.
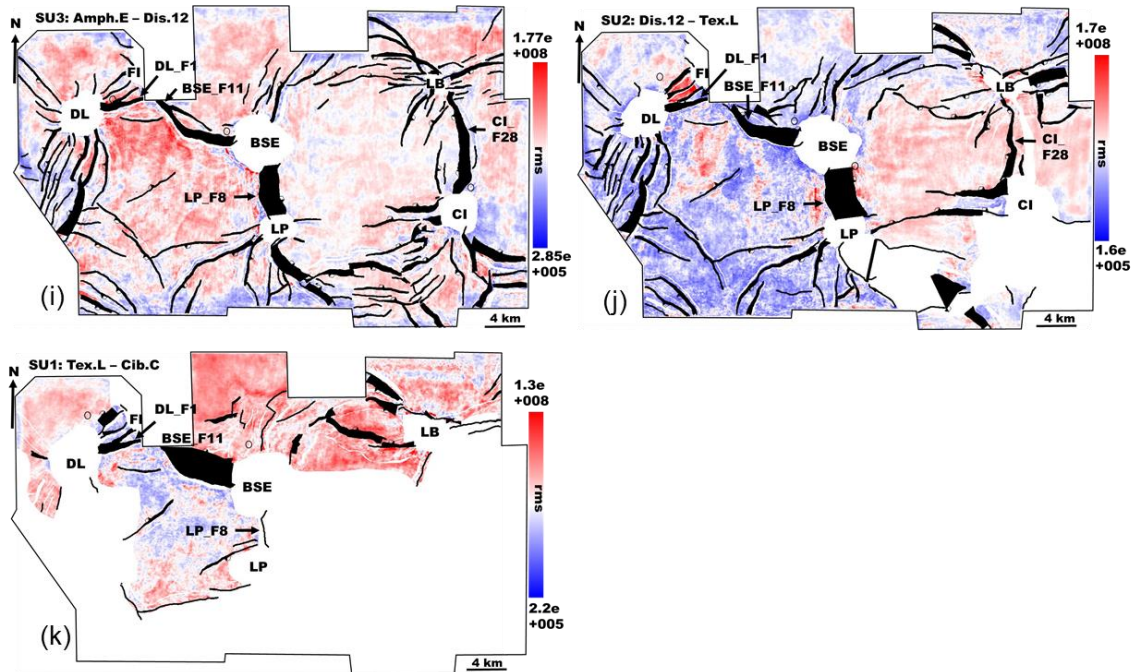
(Figure 4.17 cont'd)

Around DL_F1, the result of the attribute map agrees with the well data calculation. High rms values are found at the contact of DL_F1 with Dog Lake salt for all strata units excepts SU1 and SU6 (Fig. 4.17k & 4.17e). The rms is moderate to slightly high along the footwall cutoff on SU6 (Fig. 4.17e), whereas it varies from low to moderate on the hanging wall cutoff. The SU1 attribute shows low rms around the fault-salt contact suggesting fine-grain sediment compare to the well data value, which is obtained about 4 km north of the fault (Fig. 4.17k).

For CL_F28, high rms around the fault-salt contact from SU10 to SU6 suggest the presence of coarse-grained sediment (Fig. 4.17a-4.17e). The attribute map agrees with the sand/shale ratio. Despite the high rms values on both sides of the fault during SU9 (760 m shale), the throw decreases towards the salt-fault contact (Fig. 4.14b). The Late Pliocene SU5b shows high rms on the hanging wall and low to moderate on its footwall

(Fig. 4.17f). Despite the high rms along the fault during SU5a (Fig. 4.17g), throw

decreases rapidly toward Caillou Island (Fig. 4.14b). Low rms along the CI_F28 during

SU4 suggest fine-grain sediment (Fig. 4.17h). This corresponds to a decreasing fault

throw towards the fault contact (Fig. 4.4b). Although rms is high around CI_F28, during

SU3, rms is low within 1 km of the fault trace on both the upthrown and downthrown

block (Fig. 4.17i). Whereas on SU2, rms vary from moderate to high within salt-fault

contact (Fig. 4.17j).

4.6. Interpretation

4.6.1 Mechanism of fault formation

The result of the study of faults in the Terrebonne Bay area shows that Model 1,

i.e., a fault formed by the linkage of faults from adjacent salt stocks and Model 2, i.e., a

fault formed by the propagation of a fault from one stock to another, explain the

formation of fault connecting two salt stocks. There is no example of Model 3, i.e., a fault

that initiates within the strata and propagates and connects two adjacent salt stocks. The

growth of LP_F8 can be explained by Model 1 based on the fault geometry (Fig. 4.1a,

4.3b & 4.5) and the throw pattern (Fig. 4.12). The throw is high at each end of the fault,

where it intersects the Bay St. Elaine and Lake Pelto stocks, respectively (Fig. 4.12a &

4.12b). The location of the throw minimal at the fault center, especially for the Pliocene

M1 to Miocene *Tex.L* horizons, suggests that the fault did not initiate at the center. The

backstripped plot of the throw profile, SU4, SU3, and SU2 shows that the concave up

pattern persists after subtracting the younger throw (Fig. 4.13h - 4.13j). This

displacement low is typical of faults that formed through insection of two faults (Peacock

and Sanderson, 1991; Willemse et al., 1996). The presence of two fault segments, a

northern and southern segment during SU6, suggests that LP_F8 was initiated as two isolated faults that eventually linked to form a single fault. Thus this confirms that LP_F8 was formed by the propagation of two radial faults towards each other; one fault propagates from Bay St. Elaine and the other from Lake Pelto. Both faults linked and eventually formed a single fault.

Another fault that is formed through Model 1 is the DL_F1 and BSE_F11. The BSE_F1 and FI_F1 intersect the DL_F1 at its northeastern (Fig. 4.5h - 4.5k). Both the BSE_F11 and FI_F1 have been interpreted as a single fault that connects the Four Isle and the Bay St. Elaine stock (e.g., Ingram, 1991). However, the present study suggests that both faults are formed by the intersection of two independent faults. The isopach maps and backstripped plot (Fig. 4.9 & 4.11) show that the FI_F1 only intersected the DL_F1 during the Pliocene and Miocene. Also, it throws at the point of intersection is relatively small compared to the throw on BSE_F11. If FI_F1 and BSE_F11 were initially a single fault that was later truncated by DL_F1, the throw on the hanging wall of FI_F1 should be higher at the intersection (e.g., Dickson, 1954). The DL_F1 and BSE_F11 intersect the seafloor throughout their entire length whereas, FI_F1 retreated towards the Four Isle stock from the Late Pliocene to the Quaternary.

The DL_F1 and BSE_F11 are formed by Model 1 because their throw is maximum at the fault-salt contact and decreases towards the intersection of the faults. Throw drops abruptly on DL_F1 at the intersection point with BSE_F11. The last 500 m towards the northeast tip of DL_F1 have very little throw. Based on the backstripped profiles, both faults propagated towards each other during the Miocene, and by the Late Pliocene SU8, the BSE_F11 intersects the DL_F1. The inactive portion of the DL_F1 is

142

still present from SU8 to SU10 (Fig. 4.5i - 4.5k), and it is associated with negligible throw (Fig. 4.6b & 4.6c)

The CI_F28 is an example of a fault that was initiated and propagated by the mechanisms explained by Model 2 (Fig. 4.1a). This interpretation is based on the location of the throw maximum near Caillou Island and throw minimum near Lake Barre (Fig. 4.14a & 4.14b). Furthermore, CI_F28 did not directly intersect Lake Barre. Instead, it intersects an east-west striking radial fault, LB_F3, from Lake Barre (Fig. 4.3b, 4.5d - 4.5e). This evidence suggests that CI_F28 propagated from Caillou Island and later intersected LB_F3. This conclusion is confirmed by both the displacement backstripped plot of CI_F28, and the isopach maps simultaneously show CI_F28 retreating towards Caillou Island. The backstripped plot show *Amph.E* and *Tex.L* profile retreating after being backstrip to SU4 and SU3, respectively (Fig. 4.15h & 4.15i). The isopach map and the T-x plot shows the fault retreating towards Caillou Island from the Pliocene SU5b to the Quaternary Z1 (Fig. 4.5f - 5.5k). This further supports the conclusion that CI_F28 propagates from Caillou Island stock to Lake Barre stock.

4.6.2 Fault gradient at stock and effect of sand/shale ratio

In the Terrebonne Bay area, faults at the salt-fault interface have a geometry that can be explained using both the sand/shale ratio and the rms attribute map. The fault pattern is classified into three groups. The first group is when displacement increases towards salt contact, and throw is maximum at the salt-fault contact (e.g., Coleman et al., 2018; Mattos and Alves, 2018; Fig. 4.6d). Furthermore, this study found that strata that are truncated by this fault have a high sand/shale ratio and high rms at the salt-fault

143

contact. For example, the DL_F1 maximum throw is at the salt-sediment interface, and

the sand/shale ratio and rms are relatively high where the fault intersects the Dog Lake

stock (Fig. 4.17). Based on the rheology of different rocks, a high sand/shale ratio and

high rms suggest coarse grain rocks, e.g., sandstone. Sandstone responds to extensional

deformation by being brittle. Thus fault displacement will be high at the salt contact, and

deformation or accommodation of strain will take place inside the salt stock (Fig. 4.18).
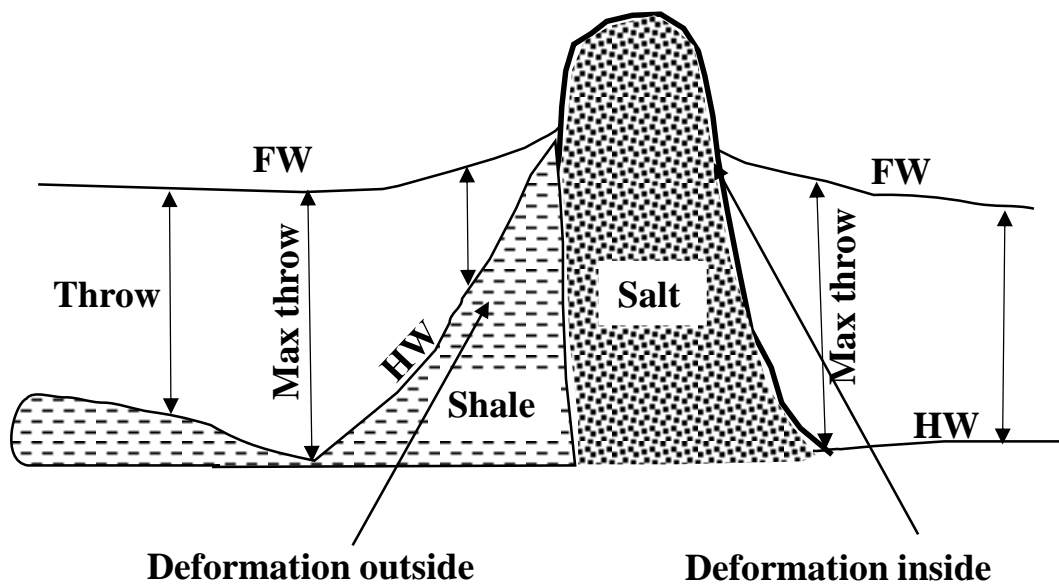
Figure 4.18. Cartoon diagram shows two different ways in which fault intersects and
interacts with salt stock. On the left side, throw reaches a maximum just before the salt
stock and then decreases rapidly towards the salt-fault interphase. The strain/deformation
is accommodated outside the salt by shale. On the right-hand side, fault throw continues
to increase towards the stock and reaches a maximum at the salt-fault interphase. Here
strain/deformation is accommodated inside the salt stock.

The second type of displacement pattern occurs when the maximum displacement

is a little farther from the salt-fault contact (e.g., Coleman et al., 2018). In this study, the

throw maximum is within 1.5 km from the salt-fault contact, and throw begins to drop

rapidly from the maximum towards the salt-fault contact (Fig. 4.14c). This sudden

decrease in throw occurs in shale strata that are truncated by faults. It can also occur on

the horizon that shows fine-grained sediment as indicated by the low sand/shale ratio and

low rms value around the fault-salt contact (Fig. 4.17h). The CI_F28 is an example of a

fault that shows this pattern. Although on SU3 and SU2, coarse grain sediment around

the salt-fault contact should favor a continuous increase in throw towards the stock (Fig.

4.17i & 4.17j), instead the throw decrease towards it (Fig. 4.14b). This anomaly may be

due to the presence of a shale ridge around the Caillou Island stock (Atwater and Forman,

1959; Freeman, 1965; Frey and Grimes, 1970; Fig. 4.3d). Shale is ductile and absorbs

strain in response to deformation by bending or folding. The ductility of shale will

accommodate strain and throw outside the salt stock (Fig. 4.18).

In most cases, a fault has a hybrid of both displacement patterns. On some strata,

a fault may have its maximum throw at the salt-fault contact, whereas on other strata, the

fault throw will rapidly decrease within the vicinity of the stock. This change in

displacement pattern from one stratum to another is due to a change in the sand/shale

ratio suggesting a shift in the depositional environment.

4.7. Discussion

The geometry and characteristics of these conceptual models are comparable with

a stepped counter-regional system (SCRS). Two known examples of SCRS that lie east of

the study areas are Bay Marchand-Grand Isle 16 and Bourbon-West Delta 133 (Schuster,

1995). These systems are similar to the examples of the conceptual models, i.e., the Dog

Lake-Bay St. Elaine and the Bay St. Elaine-Lake Pelto stocks in that they have landward

145

dipping counter-regional faults. Strata on the hanging wall of these faults thicken towards the footwall cutoff.

The fault that connects Bay Marchand with Grand Isle 16 stocks and Bourbon with West Delta 133 stocks differ from my models in their mechanism of formation. The fault between the Bay Marchand-Grand Isle 16 and Bourbon-West Delta 133 is a pseudo-fault because the surface is formed by the expulsion of salt from a basinward leaning salt body (Schuster, 1995) instead of displacement of strata. After the salt was completely expelled, the strata initially on both sides of the salt body are juxtaposed. In contrast, the faults in all my models are formed by the displacement of strata. Therefore, the horizontal and vertical offset represent actual extension and subsidence, respectively. In contrast, the horizontal offset in the SCRS is not due to an extension. Along the dip of the pseudo faults i.e., the Bourbon-West Delta 133 and Bay Marchand-Grand Isle 16 faults, there is a small sediment-sediment offset updip , whereas, at the down dip, the surface grade into a salt weld (Schuster, 1995).

An example of a fault formed by model 2 is in Egersund Basin, the Norwegian North Sea (Tvedt et al., 2016). This fault, F7, is 16 km long and bounded by two salt stocks, Delta and Omega (Tvedt et al., 2016). The asymmetrical throw profile of the fault is skewed towards the Omega stock. Similarly, the throw profile of CI_F28 is skewed towards the Caillou Island stock.

Both faults differ in some ways. The F7 is a basin bounding fault, whereas CI_F28 is transverse to the TSWB. Fault F7 established its final length when the Delta and Omega stocks were in the formative stage, and the fault southeast tip was less than 1

146

km away from the Omega stock (Tvedt et al., 2016). The fault did not directly intersect Omega at its early stage due to the diapiric stress perturbation (Tvedt et al., 2016). However, as Omega stock continues to grow, F7 eventually intersects it. In contrast, CI-F28 is a radial fault from Caillou Island that propagates towards Lake Barre.

The formation of faults that connects salt stocks in Espirito Santo Basin, southeast Brazil (Mattos and Alves, 2018) can be explained by model 1. In this basin, two salt stocks that are 5 km apart, D1 and D3, are located west of a northwest-southeast striking salt ridge. A radial fault, F10, from stock D3 has its southeast tip overlapping with another radial fault from stock D1. Similarly, another radial fault, F9, from stock D1 overlaps with a radial fault from stock D3 by 0.5 km. In comparison, DL_F1 and BSE_F11 at the early stage propagate towards each other, and BSE_F11 eventually intersects DL_F1. Although the F9 and F10 are faults not hard-linked with their overlapping faults, the high gradient at the overlapping tips suggests that the faults are kinematically interacting with the overlapping faults (e.g., Peacock and Sanderson, 1991; Walsh and Watterson, 1991). If lateral fault propagation had continued, these faults would have linked.

Fault F11 in the Espirito Santo Basin is an example of a hard-linked fault (Mattos and Alves, 2018). This fault connects stock D3 with the northwest striking salt ridge. The throw profile of F11 shows at least three throw minima with the lowest throw at the fault center. The locations of these throws minima suggest that at least two segments propagate from stock D3 and the salt ridge, respectively linked to form F11.

There is no example of model 3 in this study because faults in direct contact with salt propagate faster than faults that are not in contact with salt. Also, a rising salt stock can establish a geomechanical barrier and prevent interaction with some faults. The result in Chapter 3 indicates that diapiric stress perturbation can inhibit the propagation of faults.

When considering the nature of propagation of faults that connect adjacent stocks, some of these stocks show a rapid decrease in throw within the vicinity of the stock, which comparable to the results of studies on radial faults initiation and propagation. In Coleman et al. (2018), fault throw is not maximum at the salt-fault contact for radial faults formed on the stock overburden, whereas throw is maximum at the salt-fault interface for radial faults formed by the stem of a stock. The underlying assumption in their research is that the lithology is the same both laterally and temporally. In contrast, using rms seismic attribute maps and sand/shale ratio, my result shows that lithology varies spatially and temporally. A variation in the depositional environment will cause a fluctuations between coarse grain deposits such as sandstone and fine-grain deposition forming rocks like shale.

There was a shale layer overlying the Terrebonne Salt Withdrawal Basin before salt diapirism was instigated by differential sediment deposition. As the stocks began to rise, the shale was shouldered to the flank of the stocks. This shale now encompasses Caillou Island stock (Atwater and Forman, 1959; Freeman, 1965; Frey and Grimes, 1970), and it is also present on the south flank of the stocks that made up the Bay Marchand-Caillou Island counter-regional system (Abriel and Haworth, 2011; Freeman, 1965; Frey and Grimes, 1970).

148

The presence of a ductile rock like shale can affect the throw pattern at the salt-fault interface. In Muraoka and Kamata (1983) work on the impact of lithology variation on fault throw, the authors show that fault throw rapidly decreases from brittle to ductile rocks. The throw decrease is due to the absorption of strain by ductile rocks (Muraoka and Kamata, 1983). Similarly, the throw of CI_F28 rapidly decreases around the salt-fault contact. The presence of fine-grained rocks around the salt stock suggested by the rms attribute maps indicates that these rocks accommodated the strain through the stretching of rocks (Fig. 18).

Strata around stocks are good reservoir rocks for hydrocarbon, especially when truncated by faults (Fails, 1965; Freeman, 1965; Patti, 1988; Woodbury et al., 1974). A fault trap is one of the best traps, especially when a reservoir rock is juxtaposed against an impermeable rock. When such a trap combines with a salt trap, an oil/gas accumulation may occur. However, faults that have a decreasing throw towards a stock can lead to a leaking trap and continuous migration of hydrocarbon.

The assumption that faults throw will continue to increase towards stock can lead to misinterpretation of subsurface data. The gradient of a fault, i.e., decreasing throw towards stock, can lead to the misinterpretation of the location of throw maximum. For example, when mapping a subsurface reservoir with sparsely spaced well data, if fault throw is assumed to increase to the salt-fault contact, the fault architecture and structure of the horizon would be poorly constrained.

The mechanism of fault connecting salt stock is important because it can help interpret the timing of fault formation and linkage (e.g., Tvedt et al., 2016). This timing

149

of linkage is essential because it helps to understand the timing of salt evacuation. Also, in petroleum geology, a knowledge of the timing would help us interpret if the fault-salt traps were in place before oil migration and the charge of the reservoirs.

Most normal faults have a throw pattern similar to a normal distribution (Barnett et al., 1987; Muraoka and Kamata, 1983; Walsh and Watterson, 1987). Those formed by linkage have a throw minimal at the linkage location (Peacock and Sanderson, 1991; Willemse et al., 1996). This study shows that faults that connect a salt stock have a distinct displacement profile that can range from concave up to concave down profiles. These concavity in throw patterns are remnants of the parent faults and serve as clues for the mechanism of fault growth and propagation.

4.8. Conclusions

Faults that connects two salt stocks have a distinct kinematic characteristic and displacement profile. Based on the throw analysis of faults in Terrebonne Bay, this study reached the following conclusions;

a) Faults that connect two salt stocks can be formed through the propagation of two radial faults from separate stocks towards each other and linked to form a single fault. These faults have a unique concave up displacement profile on the throw map.

b) Faults that connect two stocks can form by the propagation of a single fault from one stock to another. In this case, the throw is usually higher at the origin of the fault and decreases towards the intersected stock.

c) Throw is not always maximum at the salt-fault contact. When it is maximum at the contact, the sand/shale ratio is usually high. Deformation occurs inside the salt stock. However, the throw can decrease rapidly within the vicinity of the salt stock. When this happens, the sand/shale ratio is low, and deformation takes place outside the salt stock within ductile strata.

LIST OF REFERENCES

Abriel, W. L., and Haworth, W., 2011, (Case Histories of Three-Dimensional Seismic
    Surveys)—Case History 10: Value of Geophysics in the Production of Bay
    Marchand Field.

Alexander, L. L., and Flemings, P. B., 1995, Geologic evolution of a Pliocene-
    Pleistocene salt-withdrawal minibasin: Eugene Island Block 330, offshore
    Louisiana: AAPG bulletin, v. 79, no. 12, p. 1737-1756.

Atwater, G. I., and Forman, M. J., 1959, Nature of growth of southern Louisiana salt
    domes and its effect on petroleum accumulation: AAPG Bulletin, v. 43, no. 11, p.
    2592-2622.

Bailey, E. B., 1931, Salt-Plugs: Geological Magazine, v. 68, no. 7, p. 335-336.

Barnett, J. A., Mortimer, J., Rippon, J. H., Walsh, J. J., and Watterson, J., 1987,
    Displacement geometry in the volume containing a single normal fault: AAPG
    Bulletin, v. 71, no. 8, p. 925-937.

Barton, D. C., 1933, Mechanics of Formation of Salt Domes with Special Reference to
    Gulf Coast Salt Domes of Texas and Louisiana1: AAPG Bulletin, v. 17, no. 9, p.
    1025-1083.

Baudon, C., and Cartwright, J., 2008a, Early stage evolution of growth faults: 3D seismic
    insights from the Levant Basin, Eastern Mediterranean: Journal of Structural
    Geology, v. 30, no. 7, p. 888-898.

Baudon, C., and Cartwright, J. A., 2008b, 3D seismic characterisation of an array of blind
    normal faults in the Levant Basin, Eastern Mediterranean: Journal of Structural
    Geology, v. 30, no. 6, p. 746-760.

Bowers, G. L., 2007, Effect of inelastic sediment behavior on near-salt stresses and pore
    pressures: The Leading Edge, v. 26, no. 11, p. 1462-1465.

Buffler, R. T., and Sawyer, D. S., 1985, Distribution of crust and early history, Gulf of Mexico basin: Gulf Coast Association of Geological Societies Transactions, v. 35, p. 333-344.

Byrnes, M. R., Britsch, L. D., Berlinghoff, J. L., Johnson, R., and Khalil, S., 2019, Recent subsidence rates for Barataria Basin, Louisiana: Geo-Marine Letters, v. 39, no. 4, p. 265-278.

Carruthers, D., Cartwright, J., Jackson, M. P. A., and Schutjens, P., 2013, Origin and timing of layer-bound radial faulting around North Sea salt stocks: New insights into the evolving stress state around rising diapirs: Marine and Petroleum Geology, v. 48, p. 130-148.

Cartwright, J., Bouroullec, R., James, D., and Johnson, H., 1998, Polycyclic motion history of some Gulf Coast growth faults from high-resolution displacement analysis: Geology, v. 26, no. 9, p. 819-822.

Cartwright, J. A., Trudgill, B. D., and Mansfield, C. S., 1995, Fault growth by segment linkage: an explanation for scatter in maximum displacement and trace length data from the Canyonlands Grabens of SE Utah: Journal of Structural Geology, v. 17, no. 9, p. 1319-1326.

Chan, A. W., and Zoback, M. D., 2007, The role of hydrocarbon production on land subsidence and fault reactivation in the Louisiana coastal zone: Journal of Coastal Research, p. 771-786.

Chapman, T., and Meneilly, A., 1991, The displacement patterns associated with a reverse-reactivated, normal growth fault: Geological Society, London, Special Publications, v. 56, no. 1, p. 183-191.

Childs, C., Easton, S. J., Vendeville, B. C., Jackson, M. P. A., Lin, S. T., Walsh, J. J., and Watterson, J., 1993, Kinematic analysis of faults in a physical model of growth faulting above a viscous salt analogue: Tectonophysics, v. 228, no. 3, p. 313-329.

Childs, C., Nicol, A., Walsh, J. J., and Watterson, J., 2003, The growth and propagation of synsedimentary faults: Journal of Structural Geology, v. 25, no. 4, p. 633-648.

Childs, C., Watterson, J., and Walsh, J. J., 1995, Fault overlap zones within developing normal fault systems: Journal of the Geological Society, v. 152, no. 3, p. 535-549.

-, 1996, A model for the structure and development of fault zones: Journal of the Geological Society, v. 153, no. 3, p. 337-340.

Coleman, A. J., Jackson, C. A.-L., Duffy, O. B., and Nikolinakou, M. A., 2018, How, where, and when do radial faults grow near salt diapirs?: Geology, v. 46, p. 655-658.

Coleman, J. M., and Roberts, H. H., 1988a, Late Quaternary depositional framework of the Louisiana continental shelf and upper continental slope: Gulf Coast Association of Geological Societies Transactions, v. 38, p. 407-419.

Coleman, J. M., and Roberts, H. H., 1988b, Sedimentary development of the Louisiana continental shelf related to sea level cycles: Part I—sedimentary sequences: Geo-Marine Letters, v. 8, no. 2, p. 63-108.

Coleman, J. M., Roberts, H. H., and Stone, G. W., 1998, Mississippi River delta: an overview: Journal of Coastal Research, p. 699-716.

Cowie, P. A., and Roberts, G. P., 2001, Constraining slip rates and spacings for active normal faults: Journal of Structural Geology, v. 23, no. 12, p. 1901-1915.

Culpepper, D., McDade, E. C., Dawers, N., Kulp, M., and Zhang, R., 2019, Synthesis of fault traces in SE Louisiana relative to infrastructure.

Dawers, N. H., and Anders, M. H., 1995, Displacement-length scaling and fault linkage: Journal of Structural Geology, v. 17, no. 5, p. 607-614.

Dickinson, G., 1954, Subsurface interpretation of intersecting faults and their effects upon stratigraphic horizons: AAPG Bulletin, v. 38, no. 5, p. 854-877.

Dutton, D. M., and Trudgill, B. D., 2009, Four-dimensional analysis of the Sembo relay system, offshore Angola: Implications for fault growth in salt-detached settings: AAPG bulletin, v. 93, no. 6, p. 763-794.

Fails, T. G., 1965, Lake Pelto Field: Terrebonne Parish, Louisiana.

Frederick, B. C., Blum, M., Fillon, R., and Roberts, H., 2019, Resolving the contributing factors to Mississippi Delta subsidence: Past and Present: Basin Research, v. 31, no. 1, p. 171-190.

Fredrich, J. T., Coblentz, D., Fossum, A. F., and Thorne, B. J., Stress Perturbations Adjacent to Salt Bodies in the Deepwater Gulf of Mexico, *in* Proceedings SPE Annual Technical Conference and Exhibition2003, Volume All Days: SPE-84554-MS.

Freeman, P. S., 1965, Caillou Island (East) Field: Terrebonne Parish, Louisiana: Oil and Gas fields of Southeast Louisiana, v. 1.

Frey, M., and Grimes, W., 1970, Bay Marchand--Timbalier Bay--Caillou Island Salt Complex, Louisiana: M 14: Geology of Giant Petroleum fields, p. 277-291.

Gagliano, S. M., Kemp, E. B., and Wicker, K. M., 2003a, Active Geological Faults and Land Change in Southeastern Louisiana: A Study of Contribution of Faulting to Relative Subsidence Rates, Land Loss, and Resulting Effects on Flood Control, Navigation, Hurrican Protection and Coastal Restoration Projects. Prepared for United States Army Corps of Engineers, New Orleans District, Louisiana: Coastal Environments, Incorporated.

Gagliano, S. M., Kemp III, E. B., Wicker, K. M., Wiltenmuth, K. S., and Sabate, R. W., 2003b, Neo-tectonic framework of southeast Louisiana and applications to coastal restoration: Gulf Coast Association of Geological Societies/Gulf Coast Section SEPM Transactions, v. 53.

Galloway, W. E., 2001, Cenozoic evolution of sediment accumulation in deltaic and shore-zone depositional systems, Northern Gulf of Mexico Basin: Marine and Petroleum Geology, v. 18, no. 10, p. 1031-1040.

Galloway, W. E., Whiteaker, T. L., and Ganey-Curry, P., 2011, History of Cenozoic North American drainage basin evolution, sediment yield, and accumulation in the Gulf of Mexico basin: Geosphere, v. 7, no. 4, p. 938-973.

Gupta, A., and Scholz, C. H., 2000, A model of normal fault interaction based on observations and theory: Journal of Structural Geology, v. 22, no. 7, p. 865-879.

Harding, R., and Huuse, M., 2015, Salt on the move: Multi stage evolution of salt diapirs in the Netherlands North Sea: Marine and Petroleum Geology, v. 61, p. 39-55.

Harrison, T. S., 1927, Colorado-Utah Salt Domes: AAPG Bulletin, v. 11, no. 2, p. 111-133.

Heidari, M., Nikolinakou, M. A., Flemings, P. B., and Hudec, M. R., 2017, A simplified stress analysis of rising salt domes: Basin Research, v. 29, no. 3, p. 363-376.

Heinrich, P., Paulsen, R., Snead, J., and Peele, H., 2015, Investigation and GIS development of the buried Holocene-Pleistocene surface in the Louisiana coastal plain: Louisiana Geological Survey-Louisiana State University, for Coastal Protection and Restoration Authority of Louisiana, p. 140. 143 plates.

Hopkins, M., Lopez, J., and Songy, A., 2018, Subsidence rates from faulting determined by Real-Time Kinematic (RTK) elevation surveys of bridges in Lake Pontchartrain: State of the Coast Book of Abstracts 2018, p. 138.

Hudec, M. R., Norton, I. O., Jackson, M. P. A., and Peel, F. J., 2013, Jurassic evolution of the Gulf of Mexico salt basin: AAPG Bulletin, v. 97, no. 10, p. 1683-1710.

Ingram, R. J., 1991, An Introduction to Central Gulf Coast Geology, New Orleans Geological Society, Salt Tectonics.

Jackson, C. A.-L., Bell, R. E., Rotevatn, A., and Tvedt, A. B. M., 2017, Techniques to determine the kinematics of synsedimentary normal faults and implications for fault growth models: Geological Society, London, Special Publications, v. 439.

Jackson, C. A. L., 2017, Throw Rate Variability on Gravity-Driven Normal Faults; Constraints from the Gudrun Fault, South Viking Graben, Offshore Norway.

Jackson, M. P., and Hudec, M. R., 2017, Salt tectonics: Principles and practice, Cambridge University Press.

Jankowski, K. L., Törnqvist, T. E., and Fernandes, A. M., 2017, Vulnerability of Louisiana's coastal wetlands to present-day rates of relative sea-level rise: Nature Communications, v. 8, no. 1, p. 14792.

156

Kairanov, B., Marín, D., Escalona, A., and Cardozo, N., 2019, Growth and linkage of a basin-bounding fault system: Insights from the Early Cretaceous evolution of the northern Polhem Subplatform, SW Barents Sea: Journal of Structural Geology, v. 124, p. 182-196.

Kolker, A. S., Allison, M. A., and Hameed, S., 2011, An evaluation of subsidence rates and sea-level variability in the northern Gulf of Mexico: Geophysical Research Letters, v. 38, no. 21.

Kolvoord, K. S., Peterson, A. R., LaForge, R. C., and Block, R. W., 2008, Rejuvenation of a shallow reservoir in the seventy-year-old Golden Meadow field, Lafourche Parish, Louisiana: Gulf Coast Association of Geological Societies Transactions, v. 58, p. 543-560.

Koyi, H., 1998, The shaping of salt diapirs: Journal of Structural Geology, v. 20, no. 4, p. 321-338.

Kuecher, G., Roberts, H., Thompson, M., and Matthews, I., 2001, Evidence for active growth faulting in the Terrebonne delta plain, south Louisiana: implications for wetland loss and the vertical migration of petroleum: Environmental Geosciences, v. 8, no. 2, p. 77-94.

Maerten, L., Willemse, E. J. M., Pollard, D. D., and Rawnsley, K., 1999, Slip distributions on intersecting normal faults: Journal of Structural Geology, v. 21, no. 3, p. 259-272.

Maltman, A., Prelithification deformation, *in* Proceedings Continental deformation1994, Pergamon Press, Oxford, p. 143-158.

Mansfield, C. S., and Cartwright, J. A., 1996, High resolution fault displacement mapping from three-dimensional seismic data: evidence for dip linkage during fault growth: Journal of Structural Geology, v. 18, no. 2, p. 249-263.

Mattos, N. H., and Alves, T. M., 2018, Corridors of crestal and radial faults linking salt diapirs in the Espírito Santo Basin, SE Brazil: Tectonophysics, v. 728-729, p. 55-74.

McBride, B. C., 1998, The evolution of allochthonous salt along a megaregional profile across the northern Gulf of Mexico Basin: AAPG Bulletin, v. 82, no. 5, p. 1037-1054.

Meckel, T. A., 2008, An attempt to reconcile subsidence rates determined from various techniques in southern Louisiana: Quaternary Science Reviews, v. 27, no. 15, p. 1517-1522.

Morton, R. A., and Bernier, J. C., 2010, Recent Subsidence-Rate Reductions in the Mississippi Delta and Their Geological Implications: Journal of Coastal Research, p. 555-561.

Morton, R. A., Bernier, J. C., and Barras, J. A., 2006, Evidence of regional subsidence and associated interior wetland loss induced by hydrocarbon production, Gulf Coast region, USA: Environmental Geology, v. 50, no. 2, p. 261-274.

Morton, R. A., Bernier, J. C., Barras, J. A., and Ferina, N. F., 2005, Historical subsidence and wetland loss in the Mississippi delta plain: Transactions - Gulf Coast Association of Geological Societies, v. 55, p. 555-571.

Morton, R. A., Buster, N. A., and Krohn, M. D., 2002, Subsurface controls on historical subsidence rates and associated wetland loss in southcentral Louisiana: Gulf Coast Association of Geological Societies Transactions, v. 52.

Morton, R. A., Tiling, G., and Ferina, N. F., 2003, Causes of hot-spot wetland loss in the Mississippi delta plain: Environmental Geosciences, v. 10, no. 2, p. 71-80.

Mouslopoulou, V., Walsh, J. J., and Nicol, A., 2009, Fault displacement rates on a range of timescales: Earth and Planetary Science Letters, v. 278, no. 3, p. 186-197.

Muraoka, H., and Kamata, H., 1983, Displacement distribution along minor fault traces: Journal of Structural Geology, v. 5, no. 5, p. 483-495.

Nicol, A., Walsh, J. J., Watterson, J., and Underhill, J. R., 1997, Displacement rates of normal faults: Nature, v. 390, no. 6656, p. 157-159.

Nienhuis, J. H., Törnqvist, T. E., Jankowski, K. L., Fernandes, A. M., and Keogh, M. E., 2017, A new subsidence map for coastal Louisiana: GSA Today, v. 27, no. 9, p. 58-59.

Nikolinakou, M. A., Flemings, P. B., and Hudec, M. R., 2014, Modeling stress evolution around a rising salt diapir: Marine and Petroleum Geology, v. 51, p. 230-238.

O'Leary, M., and Gottardi, R., 2020, Relationship between Growth Faults, Subsidence, and Land Loss: An Example from Cameron Parish, Southwestern Louisiana, USA: Journal of Coastal Research, v. 36, no. 4, p. 812-827.

Omale, A. P., and Lorenzo, J. M., 2015, Using Fault Kinematics to Evaluate the Relationship between Cenozoic Fault Activity, Sedimentation Rates, and Salt Movement in the Gulf of Mexico: A Comparison between Southwestern and Southeastern Louisiana.

Patti, S. M., 1988, South Timbalier Block 135 Field: Offshore Louisiana.

Peacock, D. C. P., and Sanderson, D. J., 1991, Displacements, segment linkage and relay ramps in normal fault zones: Journal of Structural Geology, v. 13, no. 6, p. 721-733.

Peel, F., Travis, C., and Hossack, J., 1995, Genetic structural provinces and salt tectonics of the Cenozoic offshore US Gulf of Mexico: a preliminary analysis, *in* M. P. A. Jackson, D.G. Roberts, and S. Snelson, eds., Salt tectonics: a global perspective: AAPG Memoir 65, p. 153-175.

Perez-Garcia, C., Safronova, P. A., Mienert, J., Berndt, C., and Andreassen, K., 2013, Extensional rise and fall of a salt diapir in the Sørvestsnaget Basin, SW Barents Sea: Marine and Petroleum Geology, v. 46, p. 129-143.

Pochat, S., Castelltort, S., Choblet, G., and Van Den Driessche, J., 2009, High-resolution record of tectonic and sedimentary processes in growth strata: Marine and Petroleum Geology, v. 26, no. 8, p. 1350-1364.

Rettger, R. E., 1935, Experiments on Soft-Rock Deformation: AAPG Bulletin, v. 19, no. 2, p. 271-292.

Roberts, H. H., 1997, Dynamic Changes of the Holocene Mississippi River Delta Plain: The Delta Cycle: Journal of Coastal Research, v. 13, no. 3, p. 605-627.

Rowan, M. G., Hart, B. S., Nelson, S., Flemings, P. B., and Trudgill, B. D., 1998, Three-dimensional geometry and evolution of a salt-related growth-fault array: Eugene Island 330 field, offshore Louisiana, Gulf of Mexico: Marine and Petroleum Geology, v. 15, no. 4, p. 309-328.

Rowan, M. G., Jackson, M. P., and Trudgill, B. D., 1999, Salt-related fault families and fault welds in the northern Gulf of Mexico: AAPG bulletin, v. 83, no. 9, p. 1454-1484.

Sanz, P. F., and Dasari, G. R., Controls On In-situ Stresses Around Salt Bodies, *in* Proceedings 44th U.S. Rock Mechanics Symposium and 5th U.S.-Canada Rock Mechanics Symposium2010, Volume All Days: ARMA-10-169.

Schneider, S. J., 1959, Bay Sainte Elaine oil field, southern Louisiana: AAPG Bulletin, v. 43, no. 10, p. 2470-2480.

Schuster, D., 1995, Deformation of allochthonous salt and evolution of related salt-structural systems, eastern Louisiana Gulf Coast, *in* M. P. A. Jackson, D.G. Roberts, and S. Snelson, eds., Salt tectonics: a global perspective: AAPG Memoir 65, p. 177-198.

Seni, S. J., 1992, Evolution of salt structures during burial of salt sheets on the slope, northern Gulf of Mexico: Marine and Petroleum Geology, v. 9, no. 4, p. 452-468.

Shen, Z., Dawers, N. H., Törnqvist, T. E., Gasparini, N. M., Hijma, M. P., and Mauz, B., 2016, Mechanisms of late Quaternary fault throw-rate variability along the north central Gulf of Mexico coast: implications for coastal subsidence: Basin Research, v. 27, no. 1, p. 43-59.

Steiner, R. J., 1976, Grand Isle Block 16 field, offshore Louisiana, M 24: North American Oil and Gas Fields, American Association of Petroleum Geologists Special Volumes, p. 229-238.

Stewart, S. A., 2006, Implications of passive salt diapir kinematics for reservoir segmentation by radial and concentric faults: Marine and Petroleum Geology, v. 23, no. 8, p. 843-853.

Talbot, C. J., 1978, Halokinesis and thermal convection: Nature, v. 273, no. 5665, p. 739-741.

Thorsen, C. E., 1963, Age of growth faulting in southeast Louisiana: Gulf Coast Association of Geological Societies Transactions, v. 13, p. 103-110.

Törnqvist, T. E., Wallace, D. J., Storms, J. E., Wallinga, J., Van Dam, R. L., Blaauw, M., Derksen, M. S., Klerks, C. J., Meijneken, C., and Snijders, E. M., 2008, Mississippi Delta subsidence primarily caused by compaction of Holocene strata: Nature Geoscience, v. 1, no. 3, p. 173.

Tvedt, A. B. M., Rotevatn, A., and Jackson, C. A. L., 2016, Supra-salt normal fault growth during the rise and fall of a diapir: Perspectives from 3D seismic reflection data, Norwegian North Sea: Journal of Structural Geology, v. 91, p. 1-26.

Tvedt, A. B. M., Rotevatn, A., Jackson, C. A. L., Fossen, H., and Gawthorpe, R. L., 2013, Growth of normal faults in multilayer sequences: A 3D seismic case study from the Egersund Basin, Norwegian North Sea: Journal of Structural Geology, v. 55, p. 1-20.

Vendeville, B., and Jackson, M., 1990, Physical modeling of the growth of extensional and contractional salt tongues on continental slopes (abs.): AAPG Bulletin, v. 74, no. 5, p. 784.

Vendeville, B. C., and Jackson, M. P. A., 1992a, The fall of diapirs during thin-skinned extension: Marine and Petroleum Geology, v. 9, no. 4, p. 354-371.

-, 1992b, The rise of diapirs during thin-skinned extension: Marine and Petroleum Geology, v. 9, no. 4, p. 331-354.

Vidrine, L. O., 1971, Production potential of deep Miocene rocks in southeastern Louisiana: AAPG Bulletin, v. 55, no. 2, p. 227-240.

Vodicka, A. C., 1987, Dog Lake Field Terrebonne Parish, Louisiana.

Walsh, J. J., Bailey, W. R., Childs, C., Nicol, A., and Bonson, C. G., 2003, Formation of segmented normal faults: a 3-D perspective: Journal of Structural Geology, v. 25, no. 8, p. 1251-1262.

Walsh, J. J., and Watterson, J., 1987, Distributions of cumulative displacement and seismic slip on a single normal fault surface: Journal of Structural Geology, v. 9, no. 8, p. 1039-1046.

Walsh, J. J., and Watterson, J., 1991, Geometric and kinematic coherence and scale effects in normal fault systems: Geological Society, London, Special Publications, v. 56, no. 1, p. 193-203.

Walsh, J. J., Watterson, J., Bailey, W. R., and Childs, C., 1999, Fault relays, bends and branch-lines: Journal of Structural Geology, v. 21, no. 8, p. 1019-1026.

Weitz, J. H., 1987, Bay Ste. Elaine Field Terrebonne Parish, Louisiana.

Willemse, E. J. M., Pollard, D. D., and Aydin, A., 1996, Three-dimensional analyses of slip distributions on normal fault arrays with consequences for fault scaling: Journal of Structural Geology, v. 18, no. 2, p. 295-309.

Wilson, C. A., and Allison, M. A., 2008, An equilibrium profile model for retreating marsh shorelines in southeast Louisiana: Estuarine, Coastal and Shelf Science, v. 80, no. 4, p. 483-494.

Woodbury, H., Murray Jr, I., Pickford, P., and Akers, W., 1974, Pliocene and Pleistocene depocenters, outer continental shelf, Louisiana and Texas: AAPG (Am. Assoc. Pet. Geol.) Bull.;(United States).

Yeager, K. M., Brunner, C. A., Kulp, M. A., Fischer, D., Feagin, R. A., Schindler, K. J., Prouhet, J., and Bera, G., 2012, Significance of active growth faulting on marsh accretion processes in the lower Pearl River, Louisiana: Geomorphology, v. 153-154, p. 127-143.

Yeager, K. M., and Whitehead, S., 2020, Evaluating faulting in Holocene Mississippi Dalta strata-merging deep 3-D and 2-D seismic data, near surface imaging, and vertical motion mesurements at three study areas: Louisiana RESTORE ACT report 2020, p. 16.

Young, M. J., Gawthorpe, R. L., and Hardy, S., 2001, Growth and linkage of a segmented normal fault zone; the Late Jurassic Murchison–Statfjord North Fault, northern North Sea: Journal of Structural Geology, v. 23, no. 12, p. 1933-1952.

Biography

Akinbobola Akintomide studied Applied Geology from 2004 to 2009 at the Federal University of Technology Akure, Nigeria. He proceeded to the University of Tulsa in Oklahoma from 2012 to 2014 for his master's degree in geosciences. In 2015, he was admitted into Tulane Unversity to study salt tectonics under Nancye Dawers, and he completed his geoscience Ph.D. in 2021. Bobola, as he is fondly called, has experience in the oil and gas industry. He has worked with various oil companies such as PEECO Limited in Lagos Nigeria, BGI Resources LLC in Tulsa Oklahoma, Canyon Creek Energy in Tulsa Oklahoma, and Columbine Logging Inc in Midland Texas. He has developed expertise in well log correlation, seismic interpretation, oil exploration, formation evaluation, structural geology, salt tectonics, sediment transport and morphodynamics.